# In and Ex-Situ Process Development in Laser-Based Additive Manufacturing

by

Michael J. Juhasz

Submitted in Partial Fulfillment of the Requirements

for the Degree of

Doctor of Philosophy

in the

Materials Science and Engineering

Program

YOUNGSTOWN STATE UNIVERSITY

May 2020

In and Ex-Situ Process Development in Laser-Based Additive Manufacturing

Michael J. Juhasz

I hereby release this dissertation to the public. I understand that this dissertation will be made available from the OhioLINK ETD Center and the Maag Library Circulation Desk for public access. I also authorize the University or other individuals to make copies of this dissertation as needed for scholarly research.

Signature: _____

*Michael J. Juhasz*, Student Date

Approvals: _____

*Brett P. Conner, Ph.D.*, Thesis Advisor Date

_____

*Pedro Cortes, Ph.D.*, Committee Member Date

_____

*Eric MacDonald, Ph.D.*, Committee Member Date

_____

*Virgil C. Solomon, Ph.D.,* Committee Member Date

_____

*Jason Walker, Ph.D.*, Committee Member Date

_____

*Dr. Salvatore A. Sanders,* Dean of Graduate Studies Date

## Abstract

Aircraft are currently flying much longer than their original design cycle with maintenance and logistics being paramount for keeping these aircraft flying. These aircraft require critical parts that may be out of production for a variety of reasons. This report is a subset of a larger project which looks to assess the role of additive manufacturing in assisting the aircraft supply chain with the production of spares and maintenance componentry. Addressed within the report is process development in both hybrid directed energy deposition additive manufacturing and laser powder bed fusion post-processing. Hybrid additive manufacturing combines additive manufacturing and traditional subtractive processing with synergistic layer-wise access. One benefit of an integrated, in-envelope suite of manufacturing processes is access to the structure at intermediate layers during fabrication. Implantation of sensors can inform the process of predictive maintenance and structural health management. These sensors can even support the qualification of the smart metal structures based on in-situ validation/qualification of the manufacturing process. Process development in this area will enable the next generation of aerospace components capable of providing sensing data from within the structure. This development resulted in the successful creation of proof-of-concept components which implemented both active and passive sensors. Laser powder bed fusion produced AlSi10Mg parts are being explored as a potential method for replacement of castings in aerospace applications. Maximizing the mechanical properties of this alloy is desirable to meet or exceed the performance of castings made of alloys such as A356. Like their traditionally produced counterparts, additively manufactured parts raise concerns about post-process induced distortion. Transverse isotropy and “as-produced” cellular microstructures also add to these concerns

and are unique to LPBF parts. Here the results will be presented from a design of experiments examining the post processing conditions of hot isostatic pressing, quench rate, and the length and temperature of artificial aging against existing heat treatment schedules. For the first time, the post-processing heat treatment of AlSi10Mg to include hot isostatic pressing followed by precipitation hardening heat treatments has been significantly characterized with hot isostatic pressing being shown to accelerate artificial aging.

## Acknowledgments

This effort was performed through the National Center for Defense Manufacturing and Machining under the America Makes Program entitled “Maturation of Advanced Manufacturing for Low Cost Sustainment (MAMLS)”and is based on research sponsored by Air Force Research Laboratory under agreement number FA8650-16-2-5700.

“The views and conclusions contained herein are those of the authors and should not be interpreted as necessarily representing the official policies or endorsements, either expressed or implied, of Air Force Research Laboratory or the U.S. Government.”

## Table of Contents

## Table of Figures

# List of Tables

## List of Equations

# General Introduction

This research comprises a subset of a larger research project supported through the America Makes consortium. The project is named Maturation of Additive Manufacturing for Low Cost Sustainment (MAMLS) and seeks to develop sustainment solutions for legacy aircraft by leveraging advanced manufacturing technologies as a demonstration to U.S. Air Force (AF) ("3006 MAMLS ph2 - Bell Crank Family of Parts - America Makes" n.d.). Aircraft are currently flying much longer than their original design cycle. With an average life of 27 years (Versprille 2016), maintenance and logistics are paramount for keeping these aircraft flying. These aircraft used by the AF require critical parts that may be out of production for a variety of reasons, including prohibitively high manufacturing costs, component obsolescence, low quantity requirements, and poor or no documentation (Tomczykowski 2003; Sirichakwal and Conner 2016). These issues subsequently stress the supply chain, as replacement parts are no longer being produced by the original equipment manufacturer (OEM). Additive Manufacturing can assist in filling the supply chain with the production of spares and maintenance componentry. Aircraft componentry, however, must meet stringent requirements on properties and therefore the Air Force needs to develop the expertise and knowledge to apply additive manufacturing and other advanced manufacturing technologies in order to have continued, effective maintenance and sustainment of airframes and aircraft.

The goal of this project is to assist U.S. Air Force sustainment operations through the development, demonstration, and transition of additive manufacturing (AM) and other advanced manufacturing technologies. Research efforts will be focused on four main areas:

(1) direct component manufacture, (2) jigs and fixturing, (3) reverse engineering, and (4) workforce development. Additive manufacturing will be tapped to enable on-demand replacement/repair of critically damaged or obsolete components that do not meet economic requirements of the conventional supply chain. Exploration of solutions including fabrication of non-aircraft component shop tools such as assembly aids, jigs, and fixtures for utilization at maintenance facilities. Reverse Engineering in the form of structured light scanning, touch probe, and similar technologies sourced to refresh missing or unrevised documentation. Lastly, identifying gaps in technology and workforce knowledge which need to be solved prior to actual implementation with all efforts ultimately directed at improving the sustainment of legacy aircraft. The technical approach is focused on improving the supply chain through new AM technologies and related advanced manufacturing capabilities at the Air Logistics Complexes (ALCs) and OEMs. Through site visits, candidate demonstration projects were identified. Two of which will be outlined as they form the basis for this research. These candidate projects were identified by analysis of baseline capabilities and the current supply chain.

One such project identified was the launcher rail assembly which is the interface between the aircraft and weapons system located on the pylon on many Air Force aircraft. This project was first identified from a cost standpoint. The launch rail assembly, while physically large, contains within it an actuation piston which wears and after it is out of tolerance, the entire launch rail is considered obsolete and scrapped. The repair of this piston would restore the entire launch rail system to full functionality and would result in significant cost savings by eliminating the need to purchase an entire new assembly. Hybrid

manufacturing, a technology which combines additive and subtractive methods, was selected as a means to repair the launcher piston. This technology allows for the addition of material, native or otherwise, through Directed Energy Deposition (DED) and subsequently the removal of material to ensure that geometries are within specification. Another benefit of hybrid manufacturing, and one leveraged by this research, is the internal access to a component granted by AM, something simply not possible by traditional means. This access is seen as an opportunity to introduce extra value to the component. While this value can manifest in various forms, the chosen expression of this is through the introduction of internal sensors for structural health monitoring of the component or assembly.

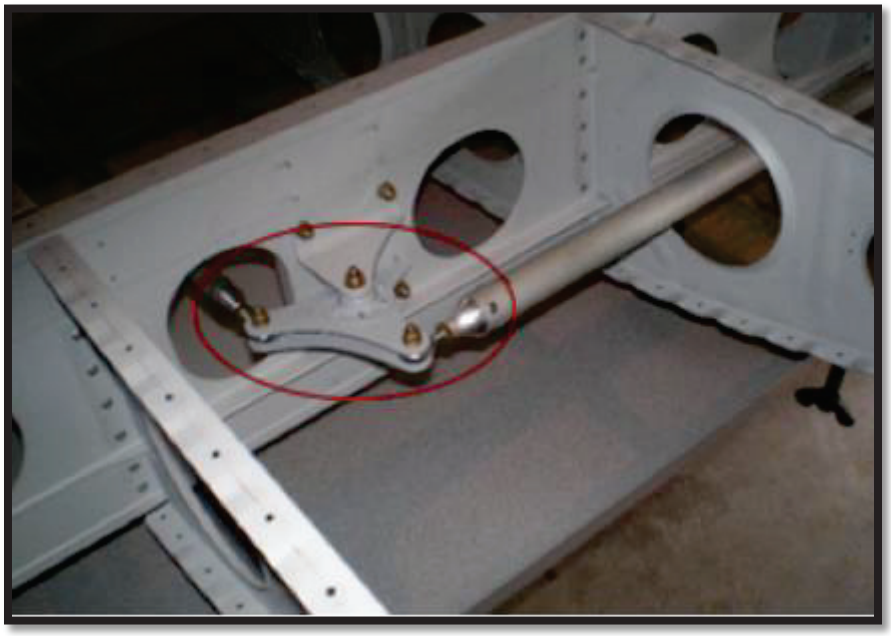

*Figure 1: Example of a bell crank ("3006 MAMLS ph2 - Bell Crank Family of Parts - America Makes" n.d.)*

As a second highlighted project, the bell crank for a given Air Force aircraft has also been identified by the Air Force as a component that is difficult to obtain via conventional

fabrication routes such as casting or machining. The bell crank is geometrically complex with numerous thick to thin transitions and angular features. The original component is cast A356 aluminum, but low part quantities, high tooling costs, and substantial lead time are the chief reasons to seek alternative means of production. Laser Powder Bed Fusion (LPBF) is the AM technology chosen in this project to attempt replacement of the original cast component in the AM alloy AlSi10Mg. With this project the plan is to fabricate a significant number of bell cranks and test coupons on two different manufacturers of laser powder bed fusion systems (EOS and 3D Systems). Repeatability, process robustness, and the ability to specify requirements that are not machine specific are three overarching aspects to this research. In machine process monitoring, metrology, a thorough understanding of post-processing, and material characterization are the main tools that will be utilized.

The challenges and solutions found during the entire MAMLS project will have a significant application to supplying legacy airframe and aircraft parts to the Department of Defense (DoD) supply chain. The MAMLS project seeks to provide an initial rubric for Additive Manufacturing's role in maintenance and sustainment. **Part 1** of this work will elucidate in-situ hybrid directed energy deposition. This applied research involves leveraging two technologies in hopes that the combined final article will be greater than the sum of its parts. **Part 2** of this research recounts the ex-situ, post-processing, potential of Laser Powder Bed Fusion produced AlSi10Mg. This research is also of the applied nature, as the component of interest already has an application. The interesting context of this research is that it is an inverse problem where the geometry, material, and process have all been decided, but the material properties must be "designed" by ex-situ means.

## *References*

"3006 MAMLS ph2 - Bell Crank Family of Parts - America Makes." n.d. America Makes. Accessed November 6, 2019. https://www.americamakes.us/portfolio/3006-mamlsph2-bell-crank-family-of-parts/.

Sirichakwal, Issariya, and Brett Conner. 2016. "Implications of Additive Manufacturing for Spare Parts Inventory." *3D Printing and Additive Manufacturing* 3 (1): 56–63.

Tomczykowski, W. J. 2003. "A Study on Component Obsolescence Mitigation Strategies and Their Impact on R&M." In *Annual Reliability and Maintainability Symposium, 2003.*, 332–38. IEEE.

Versprille, Allyson. 2016. "Air Force Modernization at Risk as Maintenance Costs Continue to Climb." National Defense Industrial Association. April 2016. http://www.nationaldefensemagazine.org/archive/2016/April/Pages/AirForceModernizationatRiskasMaintenanceCostsContinuetoClimb.aspx.

# Part 1: In-Situ Hybrid Directed Energy Deposition for Smart Structures

## *Introduction*

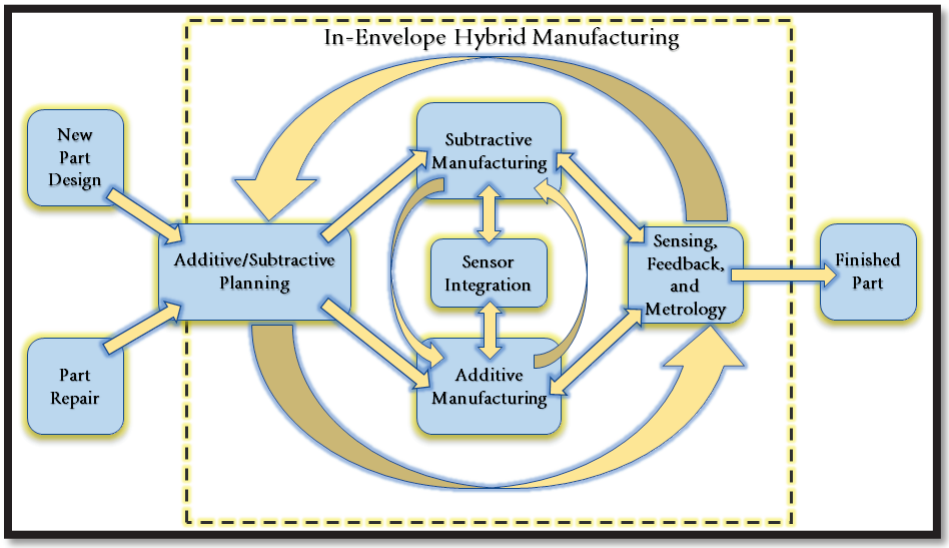


*Figure 2: Schematic of In-Envelope hybrid manufacturing*

Hybrid is an adjective meaning "of mixed character; composed of mixed parts" as given by Merriam-Webster (Merriam-Webster 1977). Therefore, as only a linguistic exercise Hybrid Manufacturing would be the combination of at least two distinct manufacturing technologies. A few authors have proposed definitions for hybrid manufacturing and the commonality between them seems to be that hybrid can, and moreover should impart more value to the process than the two individual technologies by themselves (Schuh, Kreysa, and Orilski 2009; Lauwers et al. 2014; Sealy et al. 2018). The phrase most often attributed to hybrid manufacturing is that "1 + 1= 3", or in other words the sum is greater than the parts. This "1 + 1= 3" goal is of course hard to quantify but a decent goal nonetheless and can almost be seen as an evolutionary inevitability of technology in general. With that said

there's an inherent tendency for scope creep into what exactly constitutes a hybrid process. Taking the logic that hybrid only constitutes a mixing of technologies then at the extremes all assembled components start meeting this criterion. It is at this point where some bounds need to be placed on what exactly the hybrid manufacturing process is and what is not. It is the opinion of this author and the context of this research that hybrid manufacturing must violate locality. Locality implies that two or more manufacturing operations in the past would have required two or more distinct and separate pieces of equipment. Violating locality reduces not only the amount of equipment but also the footprint (or floorspace) and resources that are needed. Hybrid must not only be a mixing of technologies but also an incorporation into a single platform. Specifically, within this framework hybrid will represent additive manufacturing combined with subtractive manufacturing. Conner et al. ("CAM-IT" n.d.) , describes the differences between ex-envelope hybrid manufacturing and in-envelope hybrid manufacturing. The figure below illustrates this manufacturing flow and makes subtle change to build upon those authors' work. The ex-envelope process flow starts with a new part design or part repair which feeds into the planning stage of manufacturing which then feeds to two separate machines which perform either additive or subtractive and depending upon the requirements of the part. this cycle can result in exchanges between the 2 wish methods with a sensing feedback in metrology loop intertwined that then results in a finished product. Granted, this figure describes an additive and subtractive process more generally speaking any two, or even more, processes could be inserted into that process flow. The virtue of creating parts in this manner is that it leverages pre-existing processes in their native format even if those processes for example are not located on the same continent. This flexibility is ex-envelope's best asset, and an

argument can be made that this is only new nomenclature for time tested design practices. The in-envelope process flow extolls the aforementioned described removal of locality and brings the additive a subtractive components of the part creation into one machine or envelope.

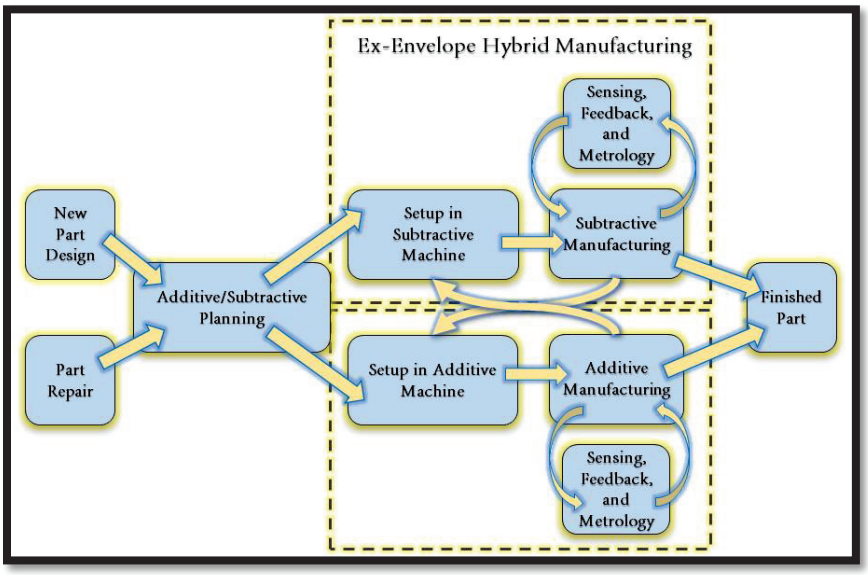


*Figure 3: Schematic of Ex-Envelope hybrid manufacturing*

Additive manufacturing (AM), also known as 3D printing, is a set of 7 archetypal classes of manufacturing as defined by ISO/ASTM 52900:2015 where an object, or widget, is produced "additively" in a layer by layer manner (Iso Astm 2015). Producing objects additively is not a new concept. For example, mud brick construction is an additive process, but additive manufacturing as a term should be considered the rather recent exploration of technologies that started with Stereo Lithography (SLA) in the 1980s. It continues to the present-day with processes such as Laser Powder Bed Fusion (LPBF) and Directed Energy Deposition (DED). DED is "an additive manufacturing process in which focused thermal energy is used to fuse materials by melting as they are being deposited. "Focused thermal

energy" means that an energy source (e.g., laser, electron beam, or plasma arc) is focused to melt the materials being deposited."(Iso Astm 2015)

In the mid-1990s Sandia National Laboratories (New Mexico, USA) developed a new additive manufacturing technology which they called Laser Engineered Net Shaping, or LENS (Griffith et al. 1996). Over the subsequent years, this process has been called by many names, mostly as a means of differentiation once the process was commercialized. A survey of the literature reveals that no less than 20 names appear such as, 3D Laser Cladding (Murphy, Steen, and Lee 1994), Cold Gas Dynamic Spray (Sova et al. 2013; Lupoi and O'Neill 2010), Direct Laser Deposition (DLD), Direct Laser Fabrication Direct Metal Deposition (DMD®) (DM3D Technology, LLC), Directed Light Fabrication (DLF) (Gu et al. 2012), Electron Beam Additive Manufacturing or EBAM ™ (Sciaky, Inc.), Electron Beam Freeform Fabrication (EBF3) (Taminger and Hafley 2006), Focused Ion Beam Direct Writing (FIBDW) (Matsui et al. 2000), Laser Chemical Vapor Deposition (LCVD) (Williams et al. 1999), Laser Consolidation (LC) (Xue and Islam 2006), Laser Deposition Welding (Kaierle et al. 2012), Laser Metal/Melting Deposition (LMD/LMMD), Laser Powder Forming (Liu, Leu, and Schmitt 2006), Laser Rapid Forming, Powder Fusion Welding (Bohrer et al. 2002), Shape Welding (Dickens et al. 1992), Shape Deposition Manufacturing or SDM (Fessler et al. 1997), Solid Freeform Fabrication (SFF) (Gursoz, Weiss, and Prinz 1990; Machlis 1990), Three-Dimensional Welding (Spencer, Dickens, and Wykes 1998), and Wire Arc Additive Manufacturing (WAAM) (F. Wang et al. 2013). The ISO/ASTM introduces the umbrella term, Directed Energy Deposition (DED), which encompasses all the previous described terms. Even since its introduction, some bastions of research still cling to older nomenclature. Despite

the numerous variety of names, the reality is that all the listed terms describe a technology that share a common feature, save a process like LCVD. This commonality is the deposition of thin layers of powder particles or wire feedstock melted by a heat source on a substrate.

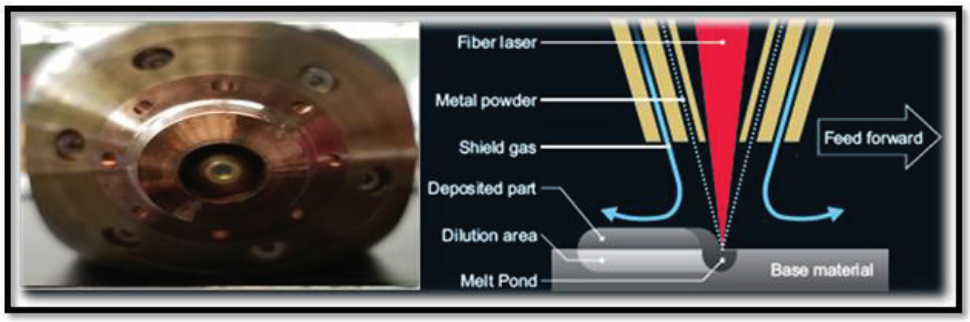


*Figure 4: Schematic of Directed Energy Deposition process*

Directed Energy Deposition is in effect a combination of, and borrows heavily from, the robust technology of laser cladding/welding and computer numeric control (CNC). Toyserkani et al. provides a generous introduction to the subject of laser cladding (Toyserkani, Khajepour, and Corbin 2004). Coupling the deposition knowledge there with the motion control available in CNC machinery forms the basis of DED technology (Ward 1959; Francis Reintjes 1991; Smid 2003). Padding shafts in steel mills, which is the buildup/repair of parts by welding, has been an eleventh-hour practice for many years. The technique is found in most literature teaching shielded metal arc welding (SMAW) for at least the last 70 years (Giachino and Weeks 1985). The buildup of components (non-repair purposes) using welding goes back to 1960s Germany though what is thought of as DED required the advent of CNC and does not appear in an additive manufacturing sense until the 1990s (Dickens et al. 1992) . Starting in the 1990s, DED has been the focus of significant research(Atwood et al. 1998; Lewis and Schlienger 2000; Griffith, Harwell, and

Romero 1997; Shamsaei et al. 2015; Thompson et al. 2015) including the manufacturing of metal and ceramic structures (Nassar, Spurgeon, and Reutzel 2014; Qian and Froes 2015; Flynn et al. 2016; Lorenz et al. 2015; Keist, Taminger, and Palmer 2016; Balla, Bose, and Bandyopadhyay 2008; Balla et al. 2009; DebRoy et al. 2017).

The physical phenomena occurring during directed energy deposition with powder injection can be described sequentially. Laser energy will strike the substrate and impart most of its energy there, the remaining energy will be split amongst reflection and heating of powder particles in flight as they make their way to the substrate. The process is best summarized as the laser creating a melt pool to which metal powder is injected into it in order to create the clad (Lewandowski and Seifi 2016). Adjacent tracks and successive layers of solidified material are deposited to build up a three-dimensional object (Gibson, Rosen, and Stucker 2015). In blown powder DED, metal powder is conveyed through the use of an inert carrier gas and supplied to the melt pool via the deposition tool head (Lorenz et al. 2015). The deposition tool head also directs the laser energy to the substrate and provides an inert shielding gas to protect the melt pool from the oxidizing atmosphere.

In an attempt at deeper understanding of directed energy deposition and cladding, models have been introduced to predict results and dynamics of the process. Pinkerton details the relatively current status of modeling with those models falling into two general categories: Physics-based, and Empirical-statistical based (Pinkerton 2015).

The basic physical phenomenon has been previously described, and any physics-based mathematical model applied to said phenomenon would at a minimum need to address heat transfer, mass transfer, and continuity. An under certain sets of assumptions and boundary

conditions analytic results can be derived. These analytic results have varying levels of sophistication, spanning from overly simple models that lack detail but prove very useful in practical applications, up to complex analytic results that exhibit more accurate predictions but can be unwieldy to apply (Pelletier et al. 1993; Toyserkani, Khajepour, and Corbin 2003). Relaxation of assumptions and introduction of complex phenomenon such as radiation pressure and surface tension effects take physics-based models from analytically solvable into the numerically solvable regime (Amine, Newkirk, and Liou 2014; Heigel, Michaleris, and Reutzel 2015; Ya, Pathiraj, and Liu 2016; Wirth and Wegener 2018). Finite element models serve as the numerical method of choice to solve these complex sets of equations though other discretization techniques have been tried. All these various models have their place and find their best applicability when the physical system most closely matches the model assumptions. All these models lose predictive power in the face of process variability.

Empirical-statistical models address process variability through statistics of direct measurements to construct process maps to predict behavior that otherwise is not directly tested. Empirical-statistical models are the more pragmatic of the two modeling categories, relying only on available user inputs to assess resultant behavior. The tradeoff is the loss of information of the physical phenomenon occurring in order to better understand and control the process itself. These models cannot indicate whether radiation pressure is a significant factor in deposition height, but rather can indicate what combination of process variables will produce a given height within margin. Regression-type models are by and large the simplest and most studied form. These models have been fitted using a variety of material combinations such as cobalt alloys on carbon steel (Colaco, Carvalho, and Vilar

1994; X. Wu et al. 1996), nickel alloys on carbon steel (Qian et al. 1997; de Oliveira, Ocelík, and De Hosson 2005), copper on aluminum (Chryssolouris et al. 2002), a cobalt alloy on cast iron (Ocelík et al. 2007), stainless steels on carbon or stainless steel (El Cheikh et al. 2012; Z. Wang, Palmer, and Beese 2016), a nickel alloy on Inconel (Ansari, Shoja Razavi, and Barekat 2016), WC12Co on stainless steel (Erfanmanesh et al. 2017), and also Ti-6Al-4V on Ti-6Al-4V (Nabhani, Razavi, and Barekat 2018). While all the studies achieved regression parameters that described that individual case well, the parameter values only seem applicable to a given material combination. This illustrates the apparent loss of phenomenological information which would be captured across all conditions. However, this should not be discouraging as regression models are easily applied and have significant value in a practical sense.

In addition to regression-type empirical-statistical models, there are more exotic versions that have been examined in the literature such as neural networks (Mondal, Bandyopadhyay, and Pal 2014), NARMAX (Nonlinear Autoregressive Moving Average Model with eXogenous inputs) (Toyserkani and Khajepour 2006), and those based on block models (Bai 1998). Given the proper setup to generate the required amount of data, the models perform well and lend them themselves readily to feedback control systems. The incorporation of sensors into the work envelope and the handling of large data sets are the current detractors from these methods, though this is an active field of research.

A unique advantage of blown powder DED is the capability to not only change materials but to modulate the composition in real time within a layer or layer-to-layer (Balla et al. 2009, 2007; W. Li et al. 2017; Ensz, Griffith, and Reckaway 2002; Carroll et al. 2016). Combining the benefits of traditional manufacturing with additive manufacturing, hybrid

technologies can provide complex, compositionally varying structures possible only with additive manufacturing coupled with the benefits of machining (surface finish and dimensional accuracies). However, the most profound benefit of hybrid may be the potential to access internal cavities within a structure at intermediate layers during fabrication, in which components can be placed robotically within the structure during manufacture. Interrupting an AM process for the purpose of embedding components within the structure has been reported since the 2000s (Prinz, Weiss, and Siewiorek 1994; MacDonald and Wicker 2016; G. Dumstorff, Paul, and Lang 2014; Hehr et al. 2018; Bournias-Varotsis et al. 2019) and has included aerospace applications (Shemelya et al. 2015; Lyke 2012), antennas (Mirzaee 2015; Z. Wu et al. 2012; Ghazali et al. 2015), biomedical devices, and 3D sensors (Le et al. 2015; Shemelya et al. 2013; Lopes, MacDonald, and Wicker 2012; Macdonald et al. 2014). However, these sensor integrations are generally limited to polymer AM processes due to the lower processing temperatures that do not impact the functionality of the embedded sensor or electronics. The integration of sensors into metal parts, while difficult, has been demonstrated. As an example, Hossain et al. embedded a piezoelectric ceramic compression strain sensor into a titanium part fabricated by electron beam melting (EBM) (Hossain et al. 2016). This involved an assemblage of individual titanium components that were built by EBM. These components were removed from the enclosed build envelope for assembly and sensor insertion, and then returned to the EBM for final cohesion into a single structure. Li et al. also integrated a sensor within a structure using a similar technique (X. Li, Golnas, and Prinz 2000). Recently, controlling thermal exposure through process planning was applied in order to embed electronics in a combined LPBF/DED effort (Petrat et al. 2018). With directed

energy deposition and careful process planning, components can be to some degree shielded from the high temperatures (roughly 1400-1500°C for ferrous materials and 700-800°C for non-ferrous materials) of metals AM as laser cladding is selectively performed in ambient conditions (temperature and pressure). At the present, this is the prototypical approach for induction of an electronic sensor into a metal AM component. Circumspect process planning can be aided by tool path code provided by CAM, but this has been identified as an underdeveloped portion of the DED process ("CAM-IT" n.d.). At present most of the process planning requires ingenuity in exploiting the tool available. An alternative approach for metal AM multi-function parts, albeit Metal Matrix Composites (MMCs), was using ultrasonic sheet lamination for sensor fabrication and incorporation of circuitry and/or optical fibers (Hahnlen and Dapino 2010; J. Li et al. 2017; Bournias-Varotsis et al. 2018, 2019). A significant advantage to this process is the lower temperature needed for ultrasonic sheet lamination which dramatically increases survivability when embedding sensors. However, the form factor of the finished component is limited to sheet-like objects and when combined with subtractive technologies can result high amount s of material waste. While discussing alternative approaches to metal multi-functional AM parts, printed ceramic strain sensors have been shown as an option for temperature and sensing in high pressure die casting applications (Gerrit Dumstorff et al. 2017). These ceramic sensors while high temperature capable have never been successfully embedded using metal additive manufacturing. The efforts in this work include embedding sensors in internal cavities built in metal structures and with reduced impact in terms of temperature to which internal components are exposed.

The novelty of this work is the leveraging of the access to a structure-under-fabrication during the layer-by-layer processing of additive manufacturing. Additive coupled with subtractive manufacturing (hybrid) provides the required dimensional and surface finishing improvements at intermediate process steps in order to insert embedded sensors, which must endure subsequent high-temperature process steps. Sensors can now be included internally in metal structures in a manner not possible previously with traditional manufacturing technologies. Investigations were completed to evaluate the conditions, for both active and passive sensors, required to survive and provide continuous data for validation of the process. Finally, the sensors were measured after fabrication to demonstrate their applicability for structural health monitoring.

## *Methods and Materials*

This section will give an overview of the experimental methods used in this investigation. Before any experiments can commence, thoughtful design of these experiments is required. Once an experimental design is decided upon, implementation of the experiment itself and the various testing methods to acquire results could commence. Examples of these testing methods include optical microscopy, and mechanical testing. The following is a recounting of the protocol developed.

## *Hybrid Additive Manufacturing*

A typical characteristic of purely additively produced parts is the need for post-processing, whether it is heat treatment for stress relief or for precipitation hardening, machining for

dimensional control, hot isostatic pressing (HIP) to heal internal porosity, etc. Hybrid manufacturing allows for some of these post processing techniques to be combined.

At Youngstown State University is a piece of equipment which will be leveraged to explore possibilities in the hybrid manufacturing design space. The machine started life as a *3*-axis vertical machining center (Haas, USA) with a *4th* axis rotary table and machine control (FANUC Controls, USA). This formed the basis for hybridization and was coupled with an AMBIT laser directed energy deposition system (Hybrid Manufacturing Technologies, UK/USA). The vertical machining center is a mid-sized (30 HP/22.4 KW) machine with a BT-40 taper spindle capable of *8000* RPM. It travels roughly a half meter in Y and Z axes and one meter in the X axis at a maximum travel speed of 25.4 m/min. The machine can utilize different tools through a *20* tool, umbrella-style tool carousel and changer. The AMBIT system retrofits the machining center to incorporate directed energy deposition in-envelope. This is accomplished through the addition of a docking collar mechanism aligned parallel to the spindle axis. The docking collar supplies any additional components required (such as laser energy, material, gas supply, etc) to transition from a subtractive to additive mode. This docking collar can also be retracted to restore the original functionality of the machining center. A key feature of the AMBIT system are the various tools which can be connected through the spindle and then attached to the docking collar (fig. 5).

*Figure 5: (left) AMBIT interchangeable tooling heads and docking collar, (right) Oerlikon powder feeders*

This expands the hybrid capability to include more than the addition of DED to material micro extrusion, ultrasonics, etc. This system, however, is set up only for DED currently. The only limitation inherent to this hybrid system is the information bandwidth available between the Fanuc control and the AMBIT control. Being a machine dedicated to research this limitation is in no way insurmountable, but options such as melt pool control and some safety features are not possible in the current configuration. Laser energy is supplied through optic fiber from a variable power, continuous wave 400W laser (IPG, RUS/GER) and the material is delivered from four powder feeders (Oerlikon, GER) (fig. 5). These powder feeders can operate simultaneously allowing for functionally graded materials to be produced. However, only a single material is of concern for this research. This hybrid additive manufacturing can allow for multi-functional parts involving the integration of sensors and electrical or optical components and/or pathways within parts.

## *Material*

Precipitation hardening 13-8 stainless steel (PH 13-8) is the material of interest for this investigation. PH 13-8 is a highly hardenable alloy with a range of heat treat options and their respective strengths are shown in Table 1.

*Table 1: Typical mechanical properties of PH 13-8 with different heat treatments*

| PH 13-8, Typical Mechanical Properties | | |
|---|---|---|
| Condition | Yield Strength (MPa) | Ultimate Tensile Strength (Mpa) |
| Solution Annealed | 827 | 1103 |
| RH-950 | 1482 | 1620 |
| H-950 | 1448 | 1551 |
| H-1000 | 1413 | 1482 |
| H-1050 | 1241 | 1310 |
| H-1100 | 1034 | 1103 |
| H-1150 | 724 | 1000 |
| H-1150M | 586 | 896 |

PH 13-8 has two major mechanisms that dictate the strength of the alloy. The first of these mechanisms is the formation of NiAl precipitate (Seetharaman, Sundararaman, and Krishnan 1981). This NiAl precipitate has been the subject of many studies and the current consensus is that it is a cubic crystal structure (Lo, Shek, and Lai 2009). Formation readily occurs even at relatively low temperatures and short time scales (Guo and Sha 2002; Guo, Sha, and Vaumousse 2003; Robino et al. 1994). The second mechanism controlling the strength of the alloy is the tempering of martensite (martempering) (Padilha, Plaut, and Rios n.d.). The microstructure of RH-950 heat treated PH 13-8 is almost entirely martensite, which is reflected in its ultimate tensile strength of 1620 MPa (Peckner and Bernstein 1977; ASM International 1990). As heat treatment temperature increases

martensite in the alloy tempers and reverts to austenite causing a decrease in yield and ultimate tensile strength. These mechanisms combine and the NiAl precipitate remain invariant to coarsening while a varying level of martensite present in the microstructure is the main driver of mechanical properties (Guo, Sha, and Vaumousse 2003).

### *Process Parameter Development*

With no prior knowledge as to what printing parameters constitute good additive depositions, a period of trial and error ensued to generate the first successful deposits in PH 13-8. A baseline flow rate calibration was needed to quantify any changes to the mass flow rate with regards to our system and also be useful later for comparisons to literature values. A balance (Ohaus, USA) with data acquisition capabilities facilitated this with powder flow rate varied from the powder feeders. Flow rates were incrementally increased and tested for 5 minutes at each increment. The length of time coupled with the sample rate of the balance allowed for experimental statistics to be performed during analysis. This resulted in linear trend with low amount of variance (Figure 6).

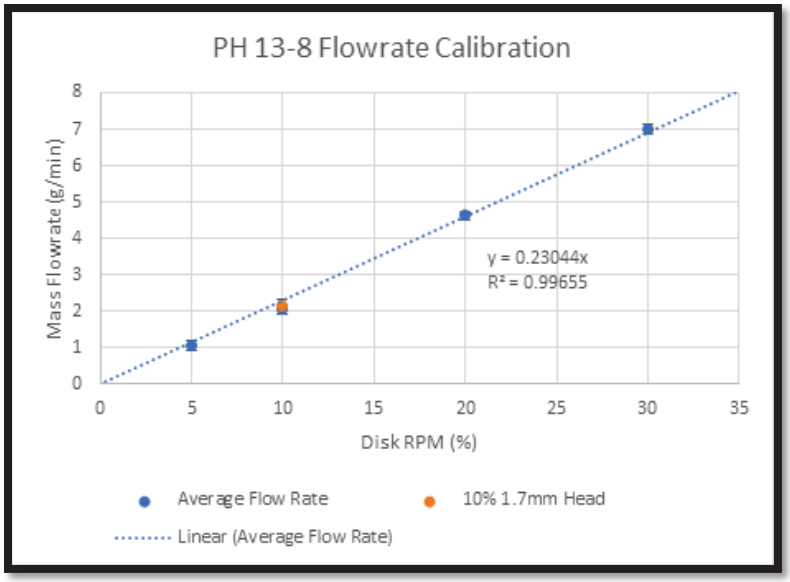


*Figure 6: Oerlikon powder feeder flow rate calibration*

It should be noted that the powder feeders increment by disk rpm percentage versus a more typical mass flow rate unit (like *g/min*). This is due to the manufacturer's design of the feeders, which employ grooved disks of varying depth a width to supply powder, and therefore need a means of equating transfer amounts given a variety of disk configurations. Both units of measurement are used in Figure 6. Trial clads were deposited and evaluated visually and by caliper measurement. The only requirements on these initial depositions were successful adhesion to the substrate (checked by a hammer and chisel), and a width and height approximately equal to the spot diameter and ½ the laser spot diameter respectively. This deposit aspect ratio was suggested by Hybrid Manufacturing Technologies (HMT) as a recommended starting point. After generating successful deposits research efforts shifted to a process parameter investigation of single depositions. Doebelin's text on experimentation was consulted as a general reference for development of experimental design (Doebelin 1995). While there are multiple parameters to adjust on

the AMBIT, the three main factors are laser power (*W*), powder mass flow rate (*g/min*), and traverse Velocity (*mm/min*). The choice of these three parameters is also justified by the literature (de Oliveira, Ocelík, and De Hosson 2005). With only a successful trial deposit, little was known of the parameter space and therefore an extended search of the space seemed warranted. The choice was made to use a symmetrical study upon the three test parameters. Using the successful, initial trial deposition as point of symmetry that makes for a *3* factor, *5* level experiment. The levels were then chosen in +/- *15%* intervals from the point of symmetry. An experiment exhausting all possible parameter configurations results in *125* different tests. The AMBIT at any given time can only store *32* unique parameter sets, so *125* different tests was excessive in light of the storage and any possible reductions to this number were sought. Reduction of the number of levels can achieve a subsequent reduction in tests at the expense of either the size of the parameter window explored or the increase in increment between any two points. The is the quintessential tradeoff of any reduced sized study. While structurally there are a few mathematical ways to reduce the number of experiments, the method chosen for this exploration was the use of an orthogonal array. The easiest way to explain an orthogonal array is that if the parameter window is thought of as a cube containing all the possible test points, the orthogonal subset is the minimum set of points inside the cube so that when viewed from any orientation the space inside the cube appears covered. There is not a unique set of points that meets this requirement, and for the purposes of this process parameter experiment the subset was chosen to adhere to a purely first order combination of parameters. The orthogonal array was thought to best cover a large parameter space while minimizing the incremental distance between test points and resulted in an

experimental matrix of *26* tests. The reduced number of tests allowed for two randomized studies to be performed with all test conditions able to be programmed and stored within the AMBIT control. All test configurations were deposited in single line passes of *127* mm (*5* inches) in length which allowed for multiple readings per test while providing a measure on process stability.

Once deposition occurred, the samples were then processed and readied for optical microscopy and measurement. Sample preparation for optical microscopy included sectioning (by sawing), mounting in polyester resin (Bondo, USA), polishing (Planeopol, DEN), and etching. The preparation recipe is provided in the table. This recipe and polishing products all came from Buehler (USA). All samples were etched for *9.5* minutes with Vilella's Reagent (San Martin et al. 2007). The samples were then imaged (Leco 300 Metallograph, USA) using differential image contrast (DIC) and measured (ToupView, USA). Measurements of interest were height, width, contact (wetting) angle, and depth of penetration. Data acquired for sample measurement was compiled in Excel (Microsoft, USA) with statistical analysis being performed in Minitab (USA).

*Table 2: PH 13-8 specimen preparation recipe*

| Step | Surface/Abrasive | RPM | Load (Setting # on Plane-o-Pol) | Time |
|---|---|---|---|---|
| 1 | 240-grit SiC Paper | 300 | 3 | Until Plane |
| 2 | 320-grit Sic Paper | 150 | 3 | Until Plane |
| 3 | 9um Suspension on Ultra-Pad Cloth | 150 | 5 | 10 min. |
| 4 | 3um Suspension on Trident Cloth | 150 | 3 | 7 min. |
| 5 | .05 um Silica Suspension on Chemomet Cloth | 150 | 2 | 5 min. |

## *Integrated Sensor Design Methodologies*

## *General Design*

In order to additively manufacture a testable proof-of-concept structure with an integrated sensor, in the view of this author, requires addressing three main requirements:

1. the selection of a simple, pragmatic test geometry to be measured and evaluated analytically,
2. the creation of a process plan that avoids damaging the integrated sensor during the high temperature processing of laser cladding, and
3. the access to the sensor both during fabrication and afterwards for field application.

Therefore, the experimental and engineering design are inexorably linked. With this in mind, demonstration pieces were designed to provide proof of concepts for the fabrication of smart structures with embedded internal components. The internal components of concern in this research are embedded sensors. A sensor is a device which responds to physical phenomena and transforms it into a signal in a predictive and indicative manner. In general, there are two broad classes of sensors: passive and active. The main signifying difference between the two classes is that active sensors are self-contained and able to sense, process, and transmit data while passive sensors require outside componentry for full functionality.

### Embedded Wireless Sensor Block

An active sensor proof of concept will investigate a high strength steel part with the sensor encased within it. Multiple objectives were slated for investigation during construction.

Firstly, a strategy for insulating delicate electronics from the intense thermal conditions inherent to the DED process. Secondly, implementation of toolpathing in order to generate an unsupported overhang. And lastly, an investigation into toolpathing strategies computer aided manufacturing (CAM) software. CAM software for subtractive processes is in a rather robust stage of development whilst CAM software for DED is currently underdeveloped. Mayka 8.0.47 (Mayka, FRA) is a software package with an included DED module and is the workhorse package being used in these investigations. The software has limited functionality but enough to produce general structures and came with a post processor that directly writes code which the AMBIT accepts. Slic3r (USA) software is an open source additive CAM software that is mainly used for FDM but is being explored for use with DED at Youngstown State since it comes with many adjustments which make it viable option for detail work. All the concepts investigated can increase the functionality of the hybrid manufacturing process.

The active sensor of interest is a Dialog Semiconductors DA14583 (USA) which can measure temperature, pressure, position, orientation, acceleration, and even local magnetic fluxes. All these data can be transferred via Bluetooth to a device of choice. This ability for parts and structures to report back information could prove invaluable for further refinement of the structures themselves, or the maintenance requirements. As an example of this new capability could be the monitoring of changes in local magnetic fluxes of a metallic structure for crack growth or propagation, so that, in essence, the part itself decides when it needs attention or replacement.

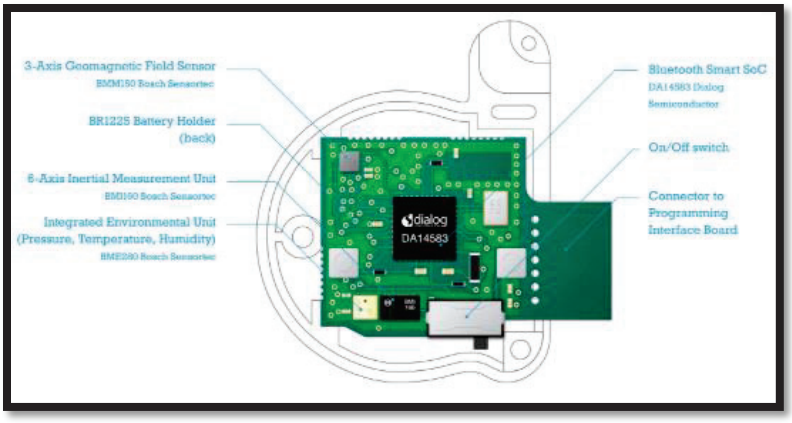


*Figure 7: Diagram of Dialog Semiconductors DA14583 sensor ("DA14583 IoT Sensor Development Kit" n.d.)*

A major detractor to incorporation of an active sensor is the proximity to roughly *1500°C* molten metal during construction. Therefore, the onus is on engineering a solution where the delicate sensor media is protected from the extreme processing conditions. Careful control of the additive deposition head through toolpathing is required to mitigate any interactions. Eventually purpose made sensors would alleviate this problem, but currently many sacrifices are needed for successful integration. Presently, the easiest path to successful sensor integration is creating as much space as possible between the electronics and any molten metal. This of course increases the overall size of the test component.

An interesting aside to this research was the development of best practices for hybrid additive/subtractive part production, some which are still being investigated. Such practices include the use of larger base layers to prevent delamination from the substrate, the number of build layers before accrued build height error requires subtractive machining to a datum surface, hatching patterns and overlaps, overbuilding with respect to machined

and non-machined part geometry, and finally the requirements to build unsupported overhangs and internal holes and/or cavities.

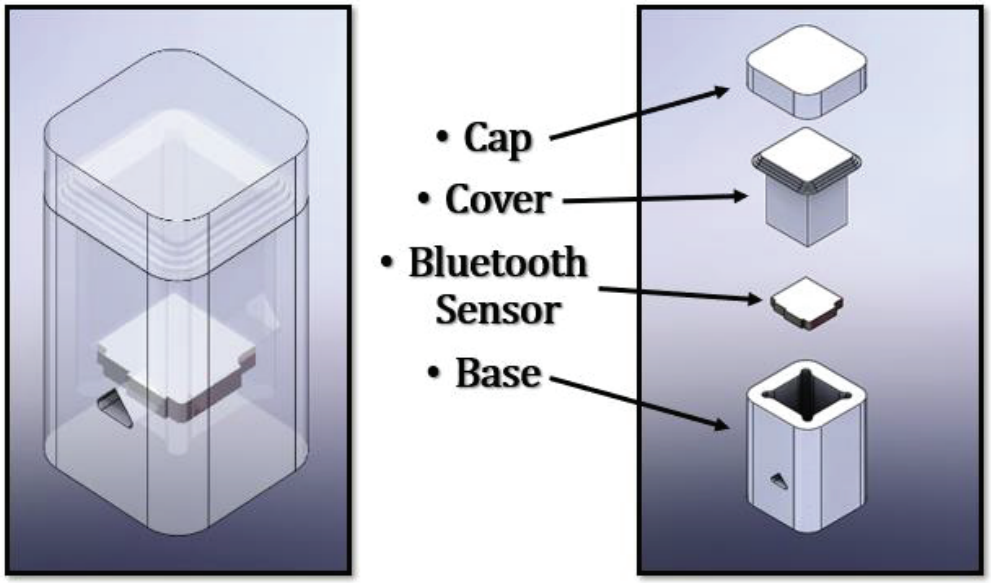


*Figure 8: Schematic of embedded Bluetooth sensor block*

Taking into account the major detractor of sensor integration, Figure 8 is a schematic of a test component. The sensor chosen does not report any data with requires a fixed attachment of the sensor to the component and therefore a simple block container could be used for the design. The overall height of the component was left arbitrary to allow for space between the sensor and the heat source. Before the arbitrary dimensions could be finalized, a series of experiments were performed to ascertain the thermal conditions present during deposition and to determine the feasibility of unsupported overhangs. The unsupported overhangs allow internal cavities and holes to be produced out of plane where either additional axes or setups would be required to accomplish such features. This is a useful capability and worthy of investigation. After this previously described set of

experiments were performed, construction of the integrated sensor test article could begin. The *base*, *cover*, and *cap* are all to be produced via hybrid manufacturing. The *base* and *cover* created separately, and once the sensor is placed inside, the *cap* will consolidate all the pieces into one object.

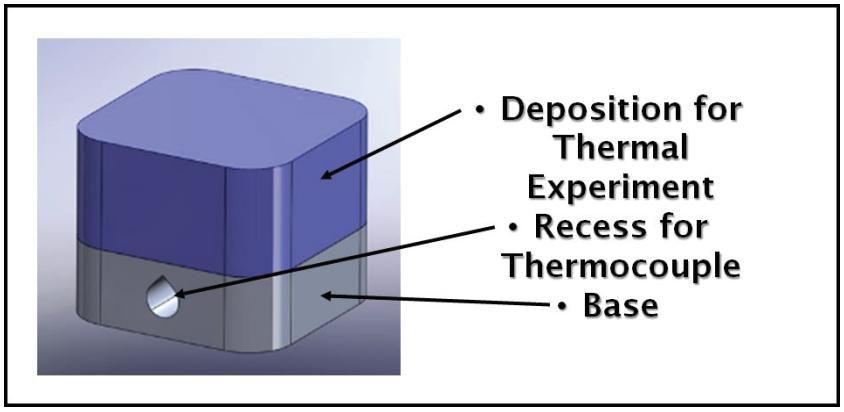


*Figure 9: Schematic of thermal experiment for protective layer determination*

Prior to the construction of the embedded wireless sensor block, a toolpathing and thermal experiment was performed to assess the viability of unsupported structures and determination required cover thickness. Unsupported holes/overhangs specifically provide access to place a thermocouple within the base and generally extends the construction capability through features able to be produced without the need for an additional operation to place it. The unsupported, blind hole for the thermocouple eliminates the need for a change in workpiece holding to accomplish a drilling operation. Also, alterations would need to be made to the base dimensions to create the clearance required for drilling. Data from the thermal experiment is gathered by a K-type thermocouple (Omega Engineering,

USA) coupled to a data logger (Measurement Computing USB-5104, USA) with sample rate of one reading per second.

### Embedded Sensor Tensile Bar: Version 1

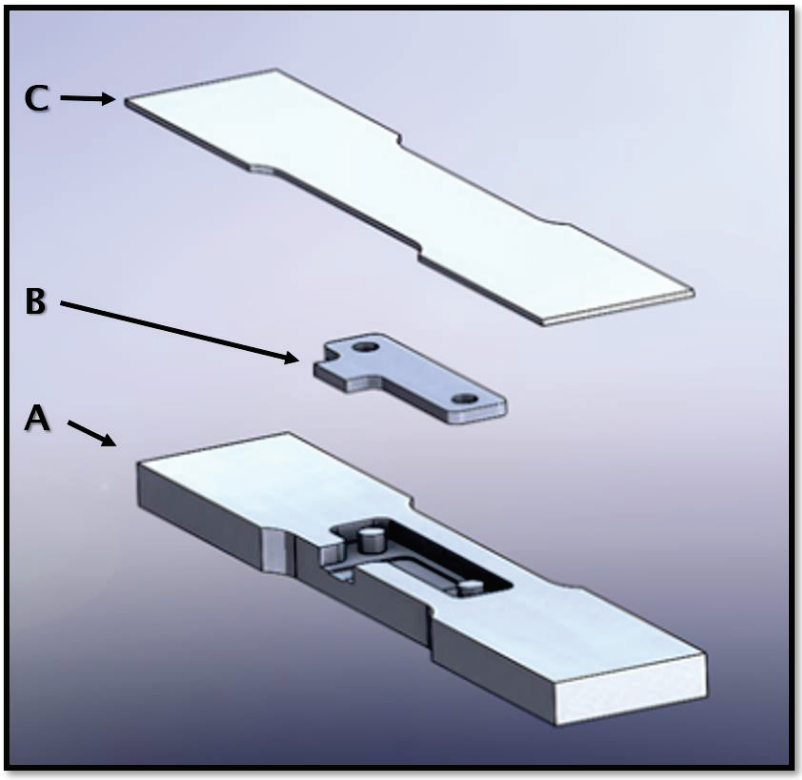


*Figure 10: Schematic of process for integrated strain sensor: (A) main laser clad section of tensile bar; (B) laser clad and machined sensor plate; (C) final laser cladding and machining to consolidate the entire structure and encapsulate the sensor plate*

The ASTM E8 standard for metallic testing was used as a guideline to drive the design (I. Astm 2016). This standard specifies geometry which limits stress to the specified test section allowing for predictable values of stress and strain. While the dimensions were altered to accommodate the sensor, the ratios of those dimensions which play an important role in receiving predictable stress levels were maintained to the standard. This geometry had no allowances for internal sensors, so a pocket was added for the sensor to reside. A

linear strain gauge (Omega Engineering, USA) was chosen to minimize the size of this pocket. The next part was to design protection of the strain gauge from the extreme heat of laser energy and molten metal due its construction of constantan and polyimide. This was accomplished by creating a relatively thick cover. Concerns with this cover is the ability to fix all six sides of the cover so that it is fully incorporated, and not detrimental the tensile bar structure. Five of the sides are easily fixed by the ability to stop the DED process, install the cover, and then continue depositing on top of the cover. To handle fixation of the sixth side, built up pins, with corresponding through holes in the tensile bar, were designed into cover which then could be deposited on to fully lock in the cover. Since the strain gauge is a wired sensor, an opening in the side of the tensile bar was added to allow those wires to exit the structure. All that was described above is captured by fig. 9. After a design was reached, a CAD model was generated and subsequently machine code for all the manufacturing steps was created by Mayka CAM software in conjunction with Fusion 360 (Autodesk, USA). This code controls the Haas VF3/AMBIT during manufacture. The tensile bar with integrated strain sensor was successfully manufactured and then tested on the Instron universal testing machine (5500R, USA). The results detailing the manufacture and testing are elaborated later.

The final design is not without its compromises as the addition of the pocket and slot does modify the stress field within the test sector. A quick, non-in-depth, finite element analysis was performed (Solidworks, Dassault Systems, FRA) to understand this augmented stress field, and the results of which showed a five-fold increase of stress in the test section. The plan is for further iterations to mitigate this increase in stress, but the currently presented design is adequate for this proof of concept.

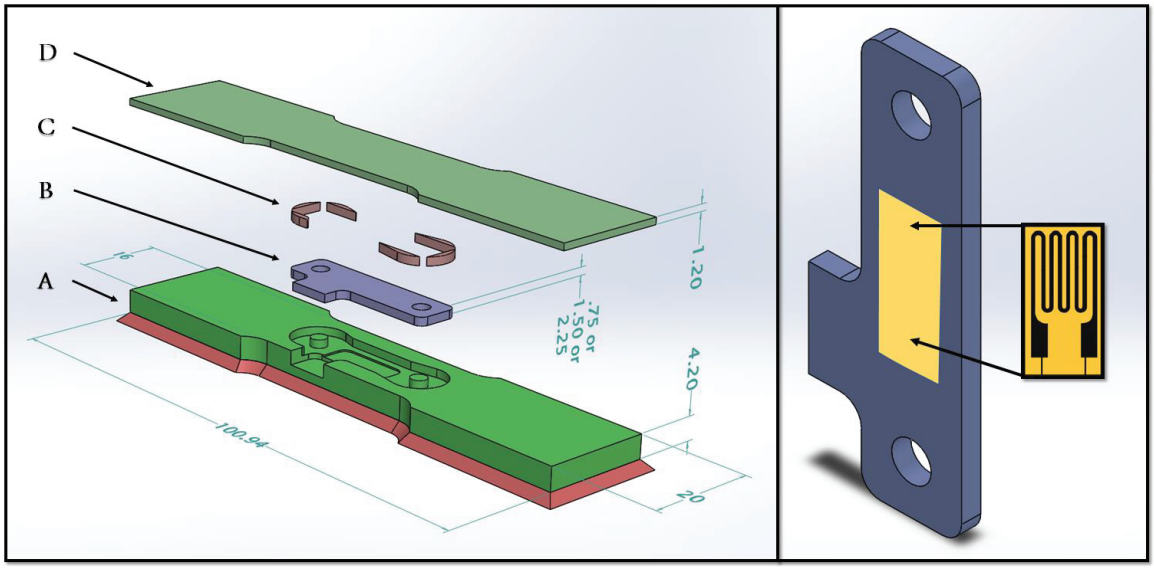


*Figure 11: Schematic of process for integrated strain sensor: (A - dark green) main laser clad section of tensile bar; (B - blue) laser clad and machined sensor plate with screen printed strain and temperature sensor on bottom surface; (C - pink) gap filling laser cladding for removing voids; (D - light green) final laser cladding and machining to consolidate the entire structure and encapsulate the sensor plate*

A second version (or iteration) of the embedded sensor tensile bar was tried, one which would include a screen-printed strain gauge. The technology to screen-print high temperature resistant strain sensors was developed at the University of Bremen, Germany. This endeavor is a collaboration between YSU and the University of Bremen with the point of contact being Rico Tiedemann.

Again the ASTM E8 standard for metallic tensile testing was used as a guideline to drive the design (I. Astm 2016). This standard specifies geometry which limits stress to the specified test section, allowing for predictable measurements of stress and strain. Modifications were made to the first tensile bar design in order to accommodate the

requirements of the screen-printed strain sensor. Figure 11 shows the structure resulting from four main manufacturing phases. Stage A (dark green) includes creating a base tensile bar to provide the majority of mechanical performance and to include to cavity for integration of the sensor plate. Stage B (blue) is the separately fabricated sensor plate with a screen-printed ceramic-ink sensor on the bottom. The plate was laser clad with the same process and materials as the tensile bar and then inserted into the tensile bar. Multiple versions of the plate were fabricated with a range of thickness in order to evaluate the minimum thickness that would allow for the survival of the sensor. Stage C (pink) included laser cladding to fill offset voids and machining to provide a flush surface upon which the final laser cladding (stage D - light green) could be implemented to consolidate the structure.

The integration of the sensor results in a reduction in mechanical performance relative to a standard tensile bar of the same thickness. However, this example serves as a proof of concept for both (a) the insertion of a sensor into an arbitrary location within a 3D structure and leveraging the access to intermediate layers provided by an additive manufacturing and (b) the survival of the sensor in the context of high temperature laser cladding processing. The sensor enabled the in-situ data collection of the internal thermal history for quality control assurances, or later, as a strain gauge in a fielded application for structural health monitoring. Both cases could justify the reduction in performance caused by the intrusion of the internal sensor. Future work will include integrating a micro-dispensing system into the tool exchanger in order to directly print sensors on difficult-to-access surfaces within complex geometries (e.g. metallic lattices) at intermediate build layers where no performance penalty would be incurred.

## Experimental Design of Sensor Plate

Circumspect process planning was required to minimize the exposure of the printed sensor to the high temperatures. The design also included provisions for accessing the electrical leads of the sensor from the outside environment for data acquisition both during and after fabrication. One of the main considerations was the use of the sensor plate as a cover for shielding the printed sensor from the high temperatures of the laser cladding process and the thickness of the plate was the main design variable in the present experiment with sensor survival as the go/no-go output. The design of the cover was required to be planar so that the screen-printed sensor could be subsequently applied, but consideration was also taken to ensure that the associated six degrees of freedom of the cover were fixed. Fixing the degrees of freedom ensured that the consolidated final article behaved as closely as possible to the control tensile bar (without an integrated sensor). The thickness was varied in three distinct steps of *0.75* mm, *1.5* mm, and *2.25* mm. As the *1.5* mm plate was the target thickness, three samples were created. Additionally, a control was fabricated which included a tensile bar without an embedded sensor, but rather was solidly clad with the same material, PH 13-8 stainless steel. The whole experiment was repeated with a second row of tensile bars as back-ups. In total, the build plate included *12* tensile bars.

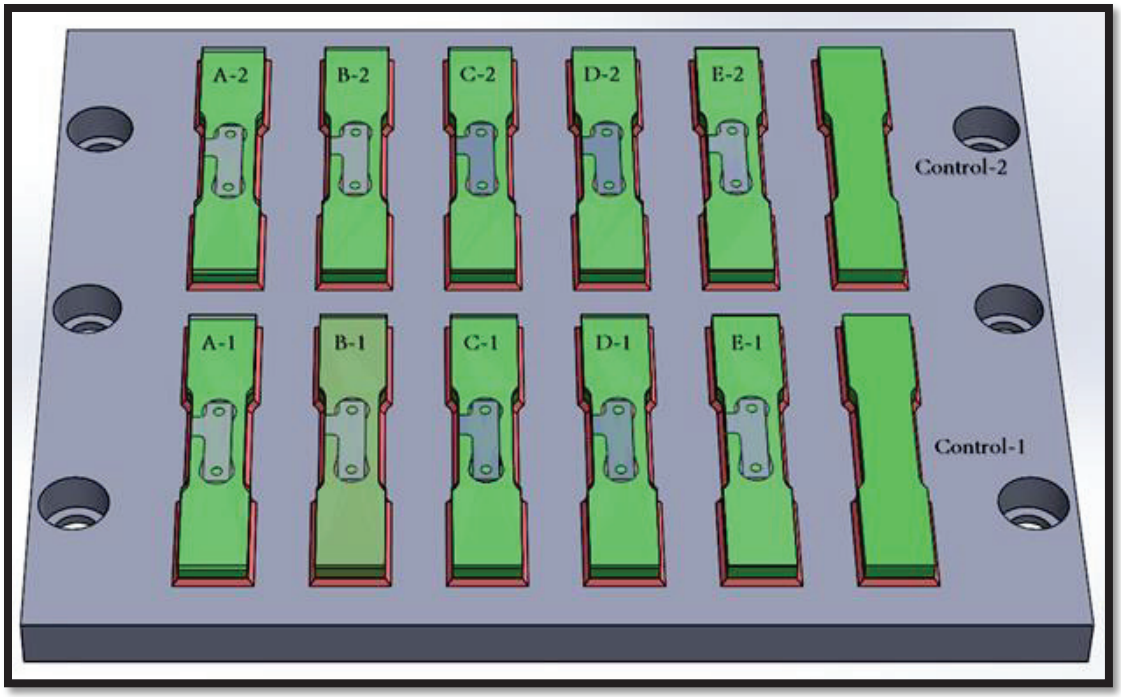


*Figure 12: Build plate. The two tensile bars on the right were without sensors and served as controls. Moving to the left, the next two included the thickest sensor plate (2.25 mm: E-1, E-2). The next six included the nominally targeted thickness of 1.5 mm (*B-1&2, C-1&2, D1&2*). The final two on the far left were the thinnest at* 0.75 *mm (*A-1, A-2*)*

## Design and Manufacturing of the Printed Sensor

In order to fabricate a sensor capable of withstanding the laser cladding temperatures, sensor materials were evaluated with higher melting points than those occurring during fabrication. Consequently, screen printable thick film pastes were identified for the sensor production and were thermally cured at *800°C*. A large difference in expansion coefficient between the ink and the steel plate results in thermally-induced stress that can lead to delamination of the sensor layer during high temperature operations after integration. Consequently, an insulation ink (Heraeus, GER) was selected to match the expansion coefficient of the steel. A sensor inlay introduces a foreign body in the mechanical structure and can lead to a degradation of the macroscopic behavior (G. Dumstorff, Paul, and Lang

2014; Gerrit Dumstorff and Lang 2015). To minimize the foreign material, the sensor plate, which served as the sensor substrate, was created with the same laser cladding process and materials as the tensile bar.

Screen printing is a printing technique that uses a stencil to transfer a pattern of ink onto a plate via a wiping blade and requires both a smooth and planer surface. The sensor plate surface upon which the sensor was to be screen-printed was measured for surface roughness and considered too rough for screen printing due to surface features as large as *250* µm. The plate was required to be further polished beyond the smoothness provided the hybrid AM machining. A single scratch or dent above *50* µm can compromise the electrical insulation layer, thus the substrates were mounted to a polish plate and were polished to a roughness of $R_{max}=15$ µm.

The sensor profiles for the manufacturing flow can be seen in Figure 13. The sensor consists of three functional printed layers: one for electrical isolation, one for low resistance electrical connections, and one for the strain sensitive sensor to implement a strain gauge element. To avoid electrical shorts to the conductive plate, three layers of the insulation were printed to provide sufficient thickness to fully isolate any unintentional surface features (e.g. dents, scratches, etc.) and each printed layer was approximately *18* µm thick for a total thickness of *54* µm (Figure 13, step 2). Subsequently, the conductor and the strain sensitive layer were printed (Figure 13, steps 3 and 4). To achieve full insulation of the sensor, three more layers of insulation were applied to the top of the sensor (Figure 13, step 5). The top insulation layers were printed while maintaining two rectangular openings at the electrical connection points for data acquisition. The inks are produced by the company Heraeus (Germany), the insulation ink is a ceramic ink with

serial number SD1010A, the conductor C8829D consists out of silver particles, and the resistor ink with serial number SR-21 350-100 and consists of platinum particles.

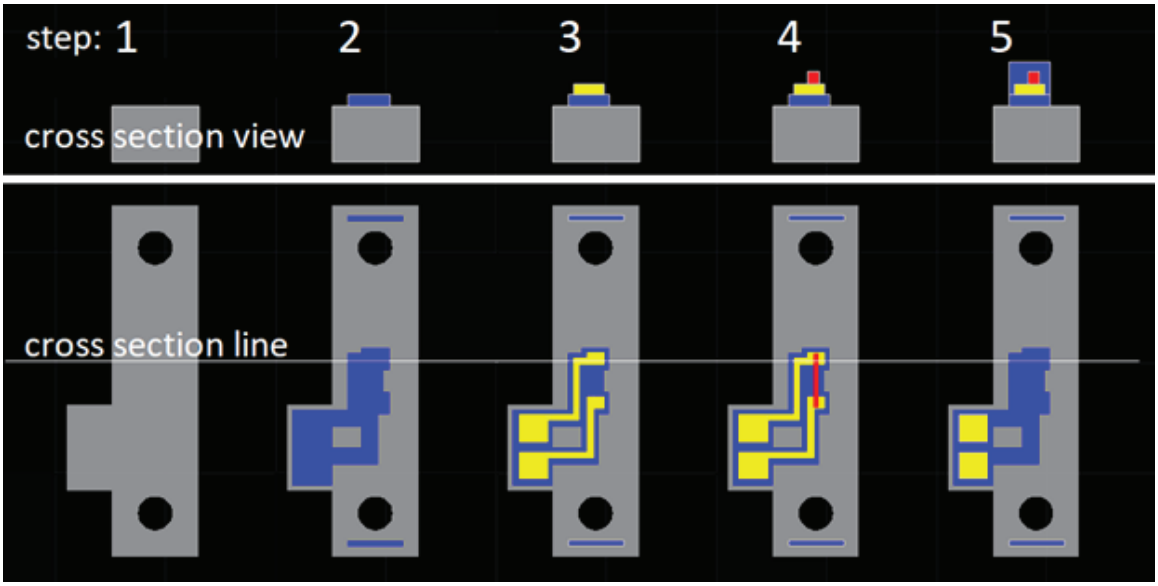


*Figure 13: Process flow of the sensor fabrication with cross section views. (1) polished substrate surface; (2) three layers of ground insulation; (3) one layer for the conductor; (4) one layer for the sensor; and (5) three layers of insulation on top of the structure*

The thickness of each layer can be adjusted by selecting screens with varying mesh-opening, thread diameter, mesh number. A mesh-opening of *45* µm and a thread diameter of *34* µm with a mesh number of *120* led to an open area of *29.6%*. The fired thickness of each layer was approximately *18* µm, which leads to a total thickness at the highest point of *144* µm, where the resistor overlaps the conductor (table 3).

*Table 3: Process flow data including layer count and total thickness in reference to Figure 13*

| Process step (ref. fig. 6) | Layer thickness | Total thickness | Total layer count |
|---|---|---|---|
| *1 Polish surface* | - | - | *0* |
| *2 Ground insulation* | *3 x 18 µm* | *54 µm* | *3* |
| *3 Conductor* | *18 µm* | *72 µm* | *4* |
| *4 Strain gauge* | *18 µm* | *90 µm* | *5* |
| *5 Top insulation* | *3 x 18 µm* | *144 µm* | *8* |

The sensor consists of eight layers in total. Each layer is individually printed, solvents were dried at *150°C* for ten minutes, and, finally, each layer was fired before the next layer was applied. Figure 14 shows the temperature profile of the furnace for any one cycle, which lasted approximately *30* minutes above *800°C* to obtain sufficient adhesion and quality on each layer.

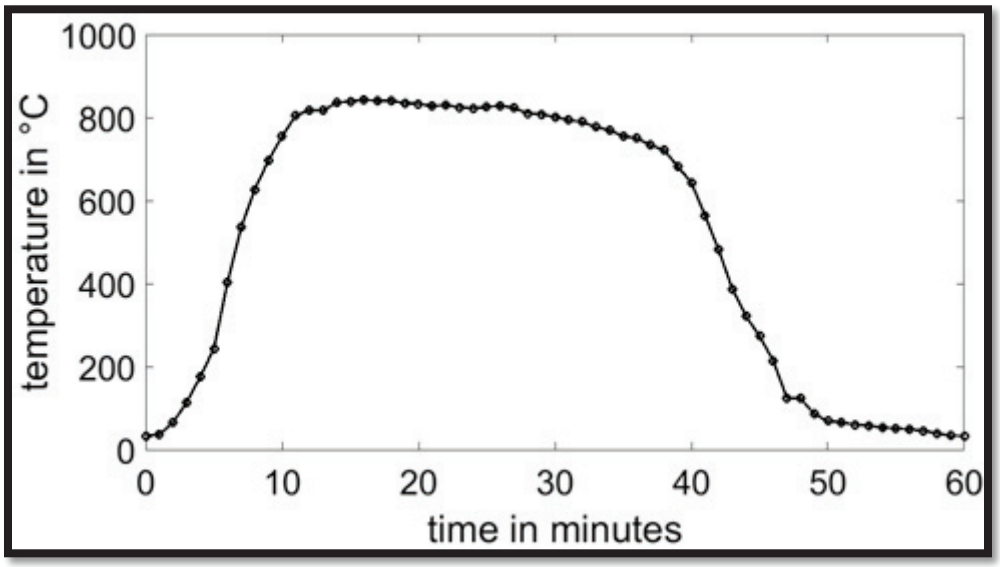


*Figure 14: Temperature profile of the furnace, each sensor layer was fired individually. In total the sensor was fired 8 times prior to embedding while laser cladding*

## *Testing*

Various equipment and software will be used to validate embedded sensor smart structures. The wireless sensor, being of the active variety, requires minimal ancillary equipment to test its survivability and performance once consolidated into the structure. All that is required is a Bluetooth antenna running the manufacturer software (Dialog Semiconductors, USA), and in this case the hardware is a smartphone (Samsung GS9, USA). For the passive strain sensor tensile bars, more equipment is required. To induce strain on the object an Instron universal testing machine will be used to apply tensile loads in a linear and cyclic manner with that company's software (Bluehill v3, Instron, USA) for control and data collection. The sensors themselves require power, a specifically designed circuit/hardware, data acquisition to read and log states, and analysis software. A strain indicator unit (Vishay P3, USA) can be employed to read and log states of the purchased linear strain gage while being tested. No in-situ data was collected during the first iteration of the embedded sensor tensile bar, but this was not the case with the second version. This in-situ data was collected using a DMM (Keysight Technologies, USA) connected via USB to a computer running their software (Keysight BenchVue, USA) for data logging. Powering the screen-printed sensor during tensile testing was a Keysight (USA) power supply with data acquisition being performed by NIDaq (National Instruments, USA) read through Simulink (Mathworks, USA).

## *Results and Discussion*

### *Process Parameter Optimization*

The optical microscopy of the process parameter study is summarized in Figure 15. The figure is arranged by increasing mass flow rate (*g/min*) and then by linear heat input (*J/mm*). Linear heat input is a combined parameter formed by dividing the laser power (*W*) by traverse velocity (*mm/min*). General trends shown are that at low power and low linear mass input no deposition is possible. At the opposite end of the spectrum, where both power and linear mass input are high, this results in depositions of large size and poor contact (wetting) angle.

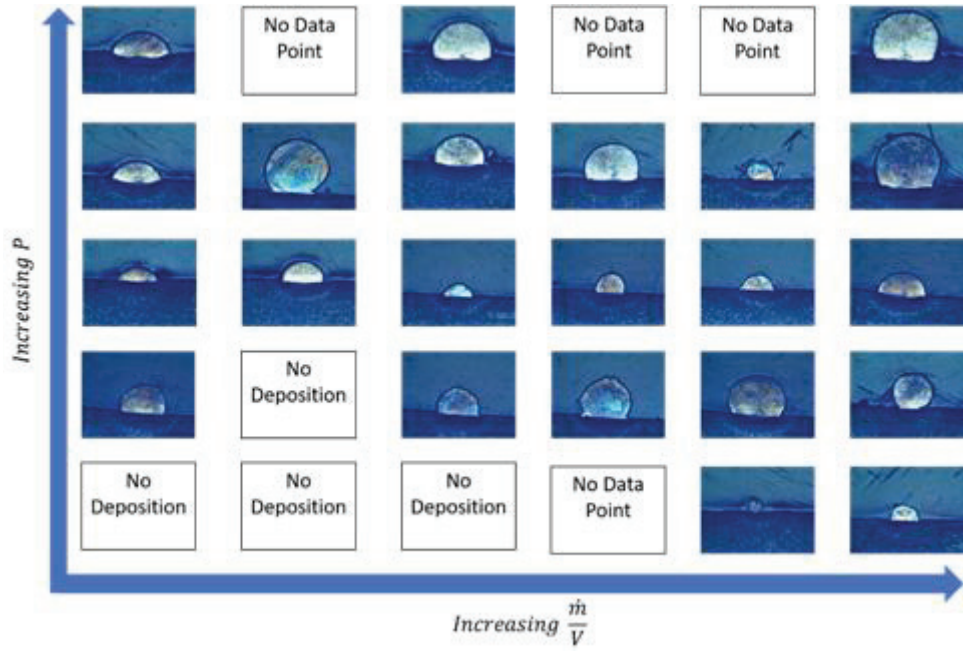


*Figure 15: Process parameter effects on depositions*

Also seen, from a qualitative standpoint, are the apparent differences in microstructure morphology as response to the process parameters. This lends credence to the proposition

that process parameters affect microstructural outcomes. Contact angle (Figure 16) is an important geometric feature of received depositions, as depositions with a contact angle of less than or equal to *90* degrees limits inter-run porosity.

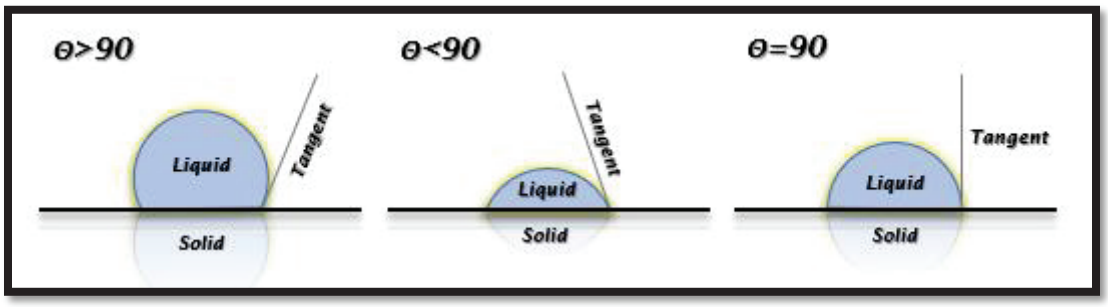


*Figure 16: Contact angle definition*

While optical measurements were taken of the contact angle, the choice of tangency can be problematic and therefore the contact angle was calculated from *(Equation I.*

$$Calculated\ Contact\ Angle = 2 * \tan^{-1}\left(\frac{2 * height}{width}\right) \quad \text{(Equation I )}$$

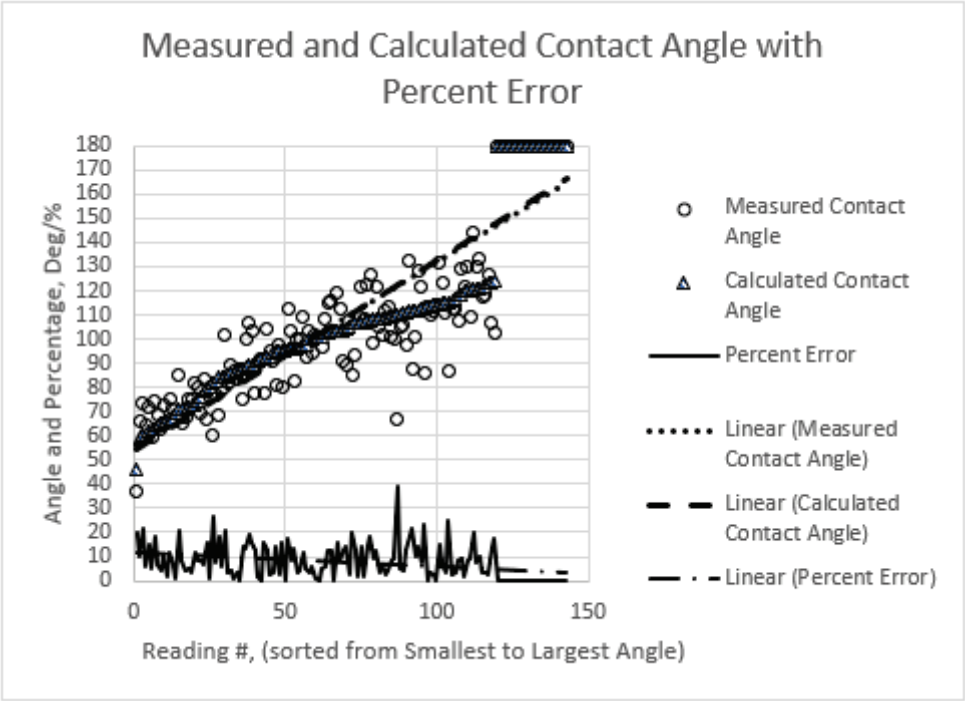


*Figure 17: Measured versus calculated contact angle*

Figure 17 shows a comparison between measured and calculated contact angles of the received depositions. The relatively low error between the two leads this author to use calculated values which are based only on height and width of the depositions. This is considered to be a more reliable measurement. Combining height and width to form the new quantity of aspect ratio simplifies analysis by creating a single response which, when applied to *(Equation I*, also yields the contact angle. Another quantity of interest is the width of deposition as a percentage of the laser spot size. Deposition widths that are a low percentage of spot size are undesirable. This typically results from a lack of injected powder in the melt pool for the given power and traverse rate causing an underdeveloped deposition. Conversely, deposition widths which are larger than the laser spot size are also undesirable. This typically results from too much powder being injected into the melt pool

for the given parameters and creates an overdeveloped deposition with a poor contact angle that promotes inter-run porosity. Therefore, the responses of interest are aspect ratio, which optimally should have a value of ½, and width as a percentage of spot size, where the target value is *100%*. This means that geometrically characterizing good depositions only requires height and width measurements.

Good quality depositions, regarding size and shape, are paramount to additively built structures. Many authors have spoken to this (Qian et al. 1997; Chryssolouris et al. 2002; de Oliveira, Ocelík, and De Hosson 2005; Amine, Newkirk, and Liou 2014). These authors[2] have introduced combined parameters of power, mass flow rate, and traverse velocity to correlate geometric responses of depositions. Most of the semi-empirical models for DED depositions found in literature are of the form: $Response=A(P^{\alpha}V^{\beta}\dot{m}^{\gamma})+B$. Where $P$ is the laser power, $V$ is the traverse velocity, and $\dot{m}$ is the mass flow rate. What is contained within the parentheses is considered to be the combined parameter. Table 4 is a comparison of all the previously introduced combined parameters (X. Wu et al. 1996; Costa et al. 2003; de Oliveira, Ocelík, and De Hosson 2005; Ocelík et al. 2007; El Cheikh et al. 2012; Ansari, Shoja Razavi, and Barekat 2016) and in parenthesis is the $R^2$ value of linear regression when applied to the dataset of this study. Of note should be the poor of fit of all the combined parameters to experimental, the best of which is *.67*.

*Table 4: Literature combined parameters for a given response*

| Response | Wu et al. | Felde et al. | de Oliveira et al. | El Cheikh et al. | Ansari et al. | Ocelik et al. |
|---|---|---|---|---|---|---|
| **Height** | $\frac{\dot{m}}{V}$ (.28) | $\frac{\sqrt{P\dot{m}}}{V}$ (.465) | $\frac{\dot{m}}{V}$ (.28) | $\frac{P^{.25}\dot{m}^{.75}}{V}$ (.39) | $\frac{P^2\dot{m}}{V^{1.5}}$ (.54) | $\frac{\dot{m}}{V}$ (.28) |
| **Width** | ~ | ~ | $\frac{P}{\sqrt{V}}$ (.587) | $P^{.75}\dot{m}^{.25}$ (.343) | $\frac{P^{1.5}}{V^{.33}}$ (.67) | $\frac{P}{\sqrt{V}}$ (.587) |
| **Aspect Ratio** | ~ | ~ | ~ | $\frac{\dot{m}^{.75}}{P^{.5}V^{1.25}}$ (.105) | $\frac{\sqrt{P}\dot{m}}{V^{1.166}}$ (.295) | $\frac{\dot{m}}{P\sqrt{V}}$ (−.25) |
| **Contact Angle** | ~ | $\frac{V}{\dot{m}}$ (.054) | $\frac{V}{\dot{m}}$ (.054) | ~ | $\frac{P\sqrt{\dot{m}}}{V}$ (.06) | $\frac{\dot{m}}{\sqrt{PV}}$ (.195) |

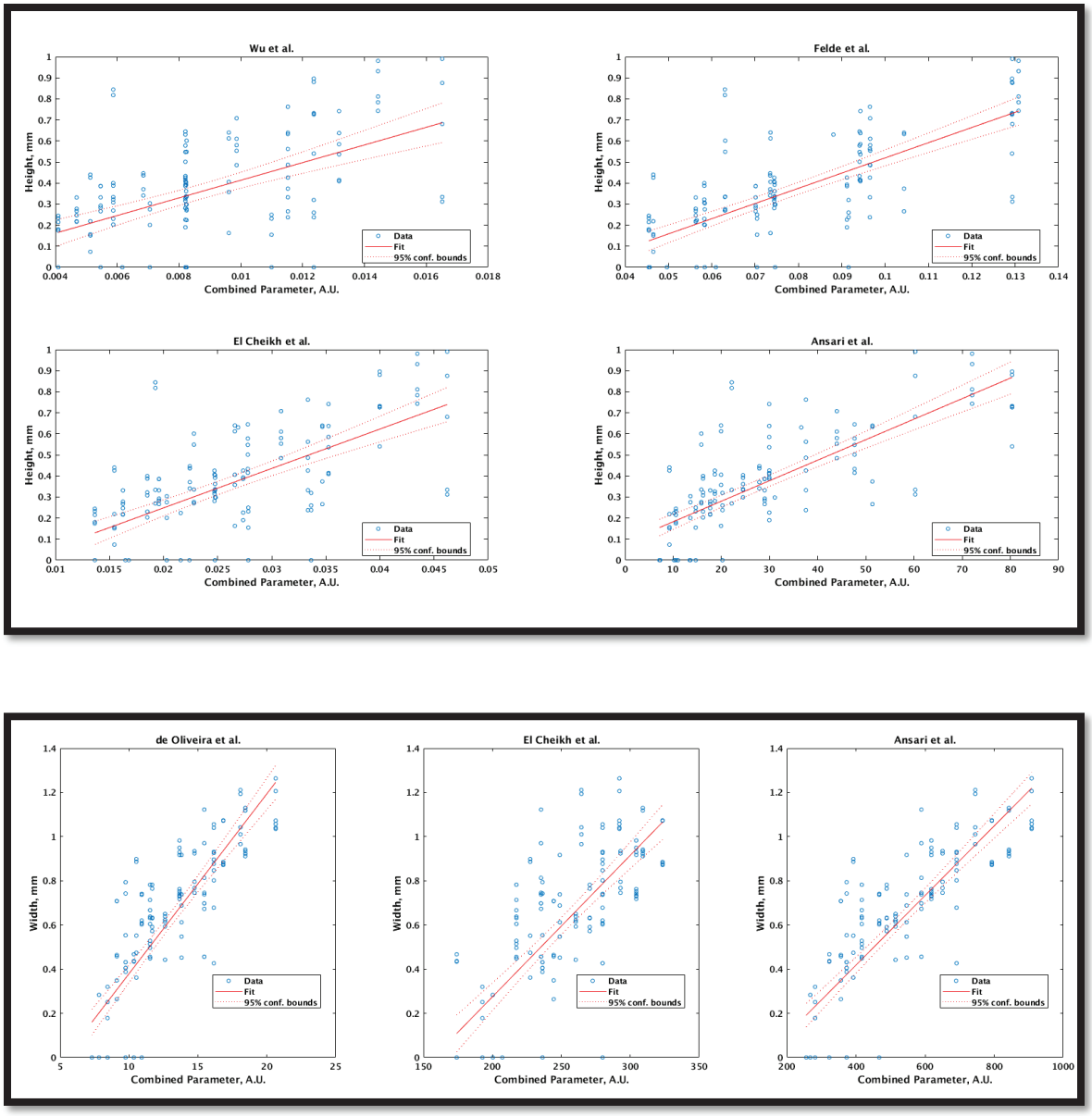


*Figure 18: Height (top) and width (bottom) versus literature combined parameters*

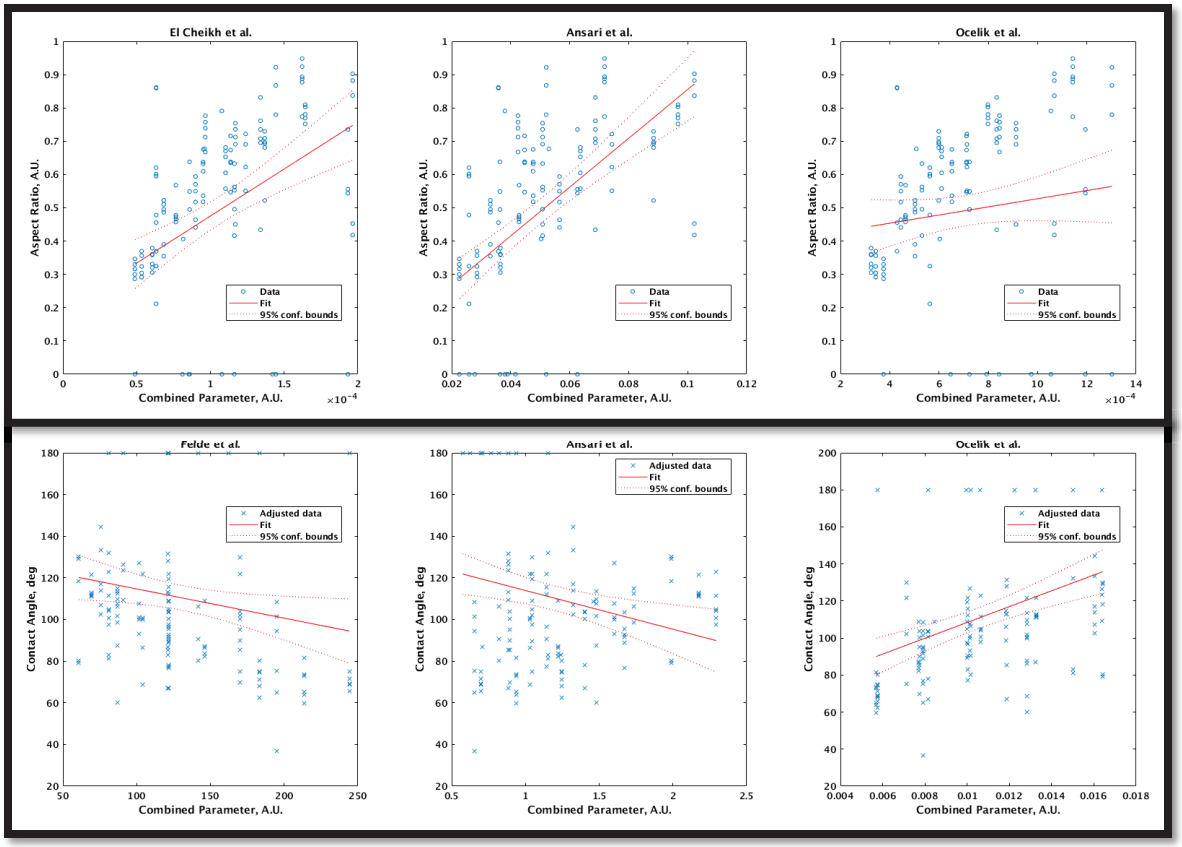


*Figure 19: Aspect ratio (left) and contact angle (right) versus literature combined parameters*

Figure 18 and Figure 19 illustrate graphically to disparity within the dataset when compared to combined parameters in the literature. Since linear correlations could not be made from combined parameters in the literature, a filtered subset of the data formed the basis for a linear regression analysis. After the regression analysis was performed, the process parameters were then mathematically optimized, and these numbers are captured by Table 5.

*Table 5: Results of process parameter optimization*

| | Power (W) | Mass Flowrate (g/min) | Traverse Velocity (mm/min) |
|---|---|---|---|
| Optimized Parameters | 296 | 2.72 | 281 |

The work of the process parameter optimization showed some interesting results and challenges. First, the incorporation of multiple measurements of a given single set of parameters exhibits more variation than has been previously reported. This variation leads to inadequate correlations when mapped against reported results in the literature which only use single measurements. The poor fit of this data to the literature can be attributed to a few factors: (1) limited data with sparse repeated measurements, (2) only having the best results reported in the literature, and (3) each material combination requires its own parameter map (set of combined parameters). Addressing those factors; every scientist battle with limited data and limited repeated measurements due resource limitations. However, only reporting the best data from any experimental leads to systematic errors in deriving a process model. A model cannot possibly predict phenomenon which were removed from the data set the model was predicated upon. It seems to be an obvious conclusion that manufacturing processes are not without variance. Therefore, in this research a hybrid approach was used. Performing a somewhat wide variation on process parameters and then taking the subset which is close to optimal geometric characteristics to perform regression analysis on to obtain satisfactory results. The opinion of this author is that it is naïve to assume that the entirety of the process parameter space could possibly be boiled down to a simple linear relation. It is analogous to stress analysis, where it would

not be assumed that the behavior of a material past the yield point would conform to Hooke's law. The analogy in reference to directed energy deposition then is that a single equation to describe keyholing, slumping, balling, and normal deposition seems unlikely. However, work is yet to be done. Comparisons between semi-empirical relations to analytic formulations of the DED process need to be investigated. Through the process of performing these parameter tests, experience and knowledge was obtained about expediting the process for future tests/experiments. If the only concern is purely the geometric nature of DED depositions, a best practice would be to perform a wide process parameter variation Taguchi-type study. All depositions first checked by a simple hammer and chisel to ensure adherence, then all depositions meeting this first check should then be evaluated by profilometry. The only values required from profilometry would be the height and width of the deposition. These can then form the important quantities of aspect ratio, and width as a percentage of laser spot diameter. The received data can then be filtered by an arbitrary distance from nominal values for the aforementioned important quantities. Linear regression can be applied to this subset and if the fit is satisfactory an optimum set of process parameters can be easily found. If this fit is not satisfactory, another test will be required. However, this test will be of a reduced process parameter space. The previous steps are repeated until the desired geometric characteristics are obtained. This should expedite process parameter optimization versus the previously used time intensive method of sectioning, mounting, polishing, and optical microscopy of fabricated depositions.

## *Integrated Wireless Sensor Block*

The goal with the integrated wireless sensor block was to successfully incorporate~~s~~ a Bluetooth sensor with multi functionality into a metallic hybrid DED structure. Coming up with the design of a block that would accommodate the sensor was fairly straightforward but to understand the protection needed for the sensor involved investigation. Therefore, a preliminary thermal experiment was designed using the outside geometry of the finished integrated wireless sensor block but accommodations for a thermocouple at its base had to be made. This thermocouple would record data while deposition occurred at various heights, or distance from the thermocouple. This data would then inform the overall cover thickness which would be the basis for protecting the wireless sensor.

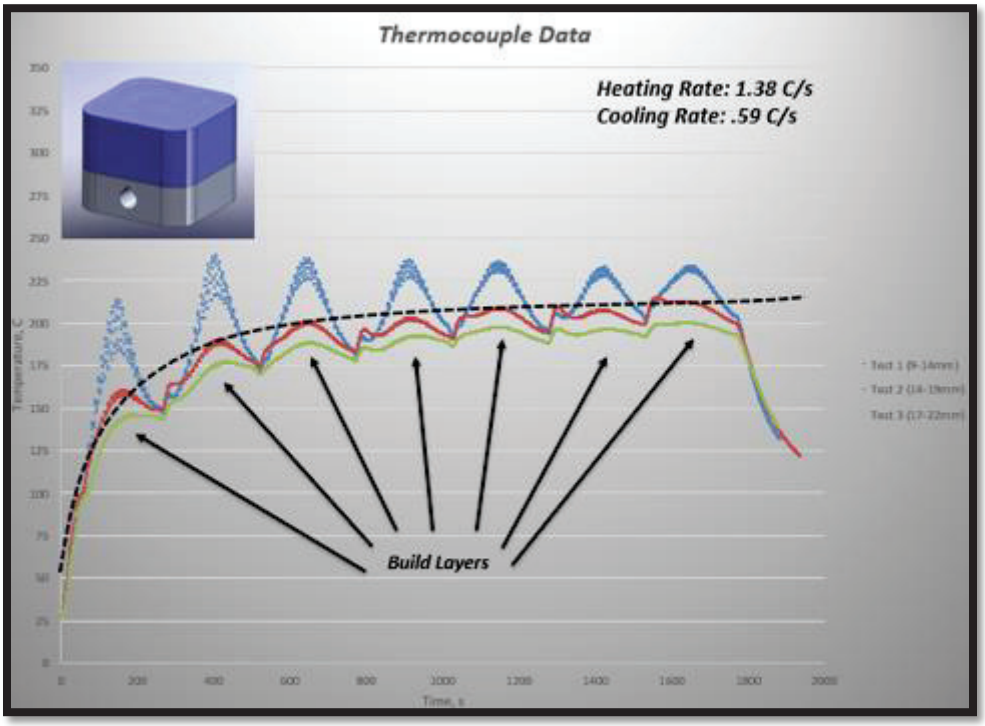


*Figure 20: Results from thermal experiment*

Figure 20 shows the results from the thermal experiment. Indicated on that figure are the individual build layers. The data streams are correlated by height. The blue data represents heights of *9* to *14* millimeters away from the thermocouple. In the upper right-hand corner is a calculated heating and cooling rate. The dashed black line shows that regardless of distance from the thermocouple, there exists a steady state temperature that will be reached during continuous deposition. Understanding this steady state temperature would be difficult as it would require knowledge of the in-envelope conditions as well as the thermal pathways created by the machine table, vice, and substrate. Figure 21 extrapolates the thermal data in order to estimate a cover thickness. The limited elevated temperature capability of the battery (roughly *100℃*) powering the sensor meant that an extremely thick cover was required for this application.

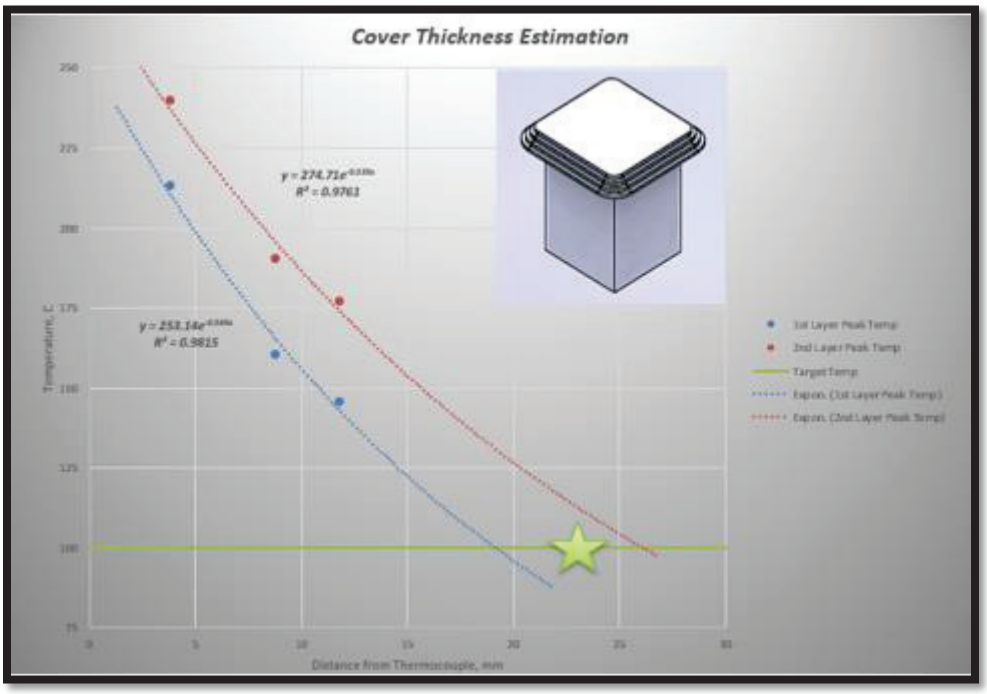


*Figure 21: Extrapolation of data for cover thickness requirement*

The build had both successes and failures. While technically difficult to produce, unsupported access holes were able to be made in two of the walls of the sensor block. In a three-axis setup, unsupported features or holes are a delicate balance of a few factors. The hatch spacing at the unsupported feature edge must be reduced to limit the amount of laser energy which will bypass that edge and strike lower layers. This laser energy that bypasses the desired deposition location can strike unintended areas causing dimensional changes and spatter accumulation. In the area of an unsupported feature the conductive heat transfer is lessened by the reduction of material directly adjacent the deposition track. This results in softening and slumping of the deposition and a tendency to burn through close the unsupported feature. To counteract this behavior, an effective strategy is to increase the traverse rate in the area of the unsupported feature. This does change the deposition geometry and therefore needs to be accounted. At present, there are not many options to accomplish these required changes through CAM or machine control. The unsupported features produced in this study were accomplished by adapting a CAM software (SLIC3R, USA) typically used for fused deposition modeling (FDM) of polymers. Other process changes were assessed during the build of the sensor block such as alterations to the hatching strategy used on a given layer. The primary strategies investigated were those that either did or did not include an outside contour pass, and the amount of overbuild required to have a successful build. The outside walls of the sensor block in fig. 21 (left) make evident those trials. The lower portions of the sensor block were completed using an outside contour. In general, this strategy works satisfactorily. Its primary detractor being the burns (dark rings) from laser energy bypassing the outside contour. Towards the top of the sensor block, the layers were completed without the use of

an outside contour. This strategy reduced the bypass laser energy but requires significant overbuild (levels that were not achieved) to produce a continuous surface after machining. While not essential to the study of embedding sensors in within structures, these sub-studies all add to the exploration of hybrid processes and capabilities.

By far the largest success of the sensor block build was that the wireless sensor did survive the process which was shown by its indicator light flashing. Unfortunately, the battery of the wireless sensor must have been damaged by the heat, as the sensor would only remain powered for a limited amount of time. Also, data was never received from the sensor either due to the decreased battery life and/or the signal being blocked by the structure itself. The sensor block was sectioned by EDM (FANUC RoboCut C600iB-12, USA) to reveal the Bluetooth sensor within. A new sensor was placed inside and subsequently tested for data transmission. The Bluetooth sensor successfully transfers data while the server block is open, but when the sensor is enclosed in the block the data connection is lost. These results are promising for an initial iteration, as everything learned during the creation of the first sensor block is solvable and future iterations are worth pursuing.

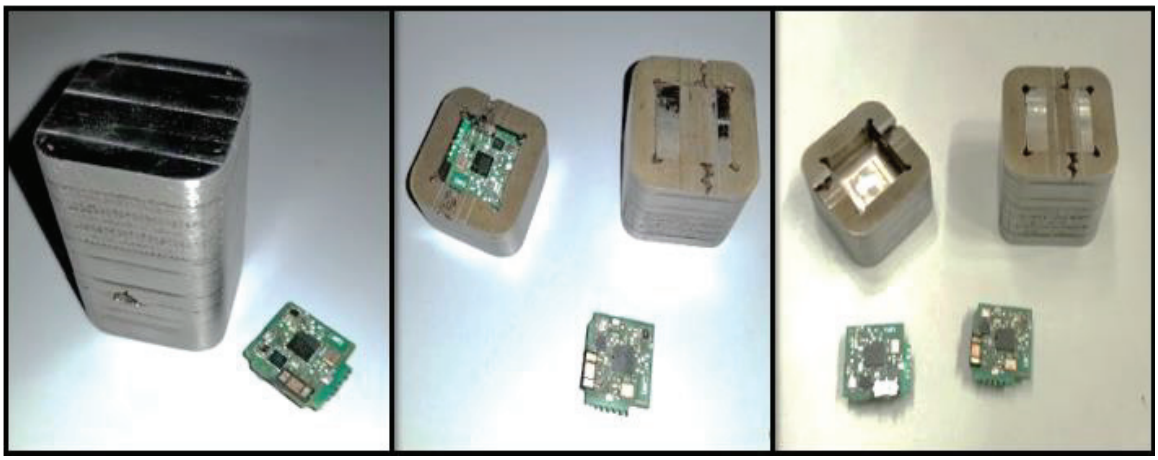

*Figure 22: Completed sensor block which was eventually sectioned to reveal the sensor inside*

## *Integrated Sensor Tensile Bars: Version 1*

Figure 23, Figure 24, and Figure 25 below illustrate the process of the buildup of the integrated sensor tensile bar. Both the main tensile bar and protective cover were built on *400*-series stainless steel substrates using the optimized process parameters. Each was also overbuilt in height and width to facilitate full cleanup when being machined down to specifications.

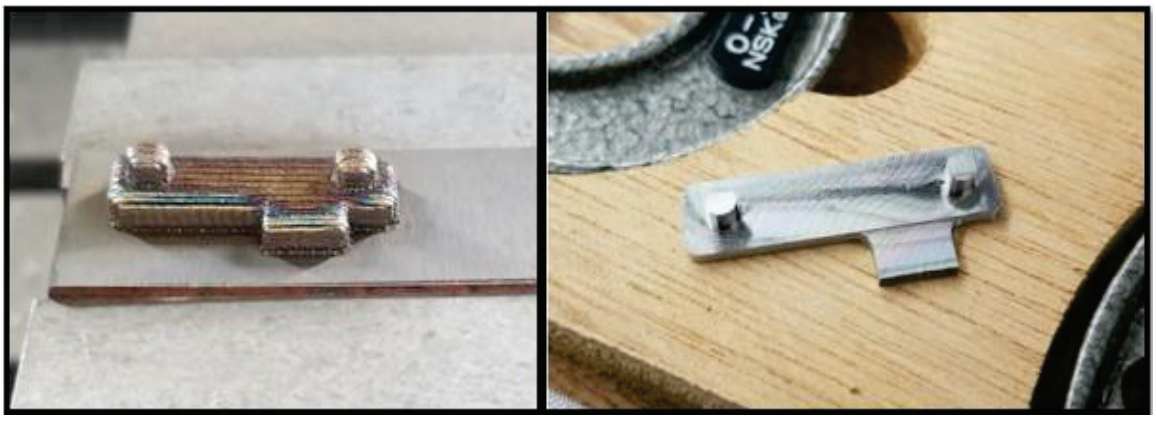

*Figure 23: Protective cover*

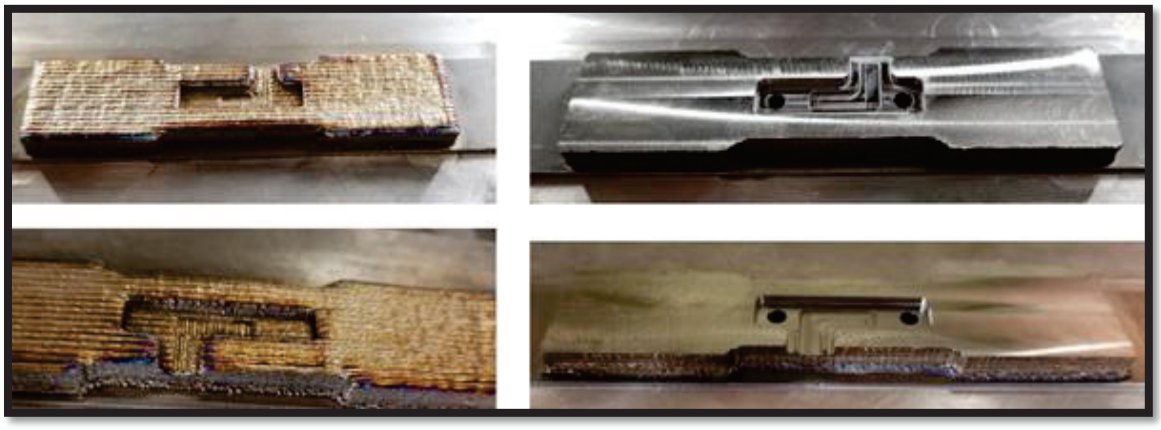

*Figure 24: Buildup of main tensile bar*

Figure 23 and Figure 24 illustrate the before and after states of the two main components. On the left in each figure is the as deposited state, and on the right is the after machining.

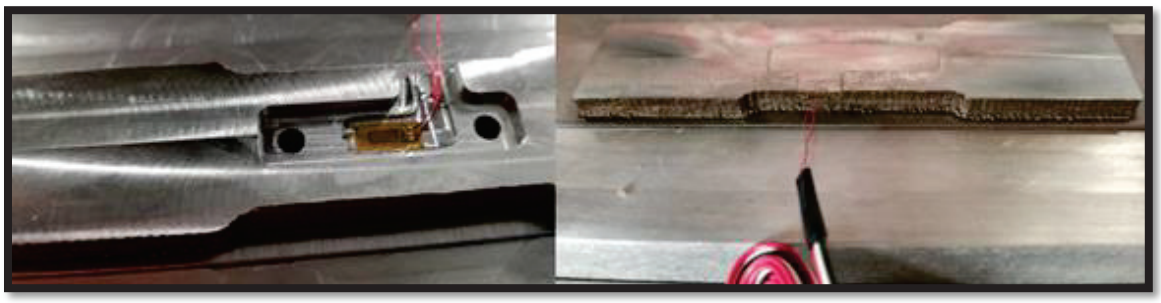

*Figure 25: Sensor and cover installed*

At this point the strain gauge was glued down and the protective cover installed (Figure 25). After each step the strain gauge was checked using a strain indicator box (Vishay P3, USA) to ensure that it was still operational. Next, material was deposited on top of the tensile bar to fully encapsulate fully the strain gauge and cover into the structure. Lastly, the whole tensile bar was finish machined on all surfaces using the hybrid Haas/AMBIT machine.

The finished tensile bar was then tested in an Instron universal testing machine (5500R, USA). The idea was to load only the tensile bar in the elastic regime to get multiple tests on the integrated strain gauge, but as is evident in Figure 26 the tensile bar failed during the first test. A few interesting points of note are that failure initiated from the slot opening on the side and that the structure was not *100%* dense. Pores could be seen by eye on the fracture surfaces. This porosity is believed to be a result of the orthogonal layer-to-layer toolpathing that the CAM software (Mayka, FRA) produces. Further investigation is

ongoing with regards to hatch spacing and layer-to-layer orientation. Figure 27 is the resulting stress-strain curve generated during the test.

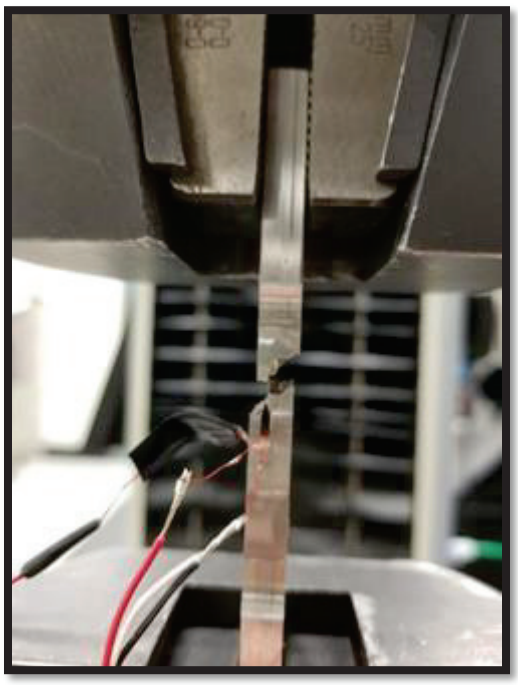

*Figure 26: Fracture of tensile bar in universal testing machine*

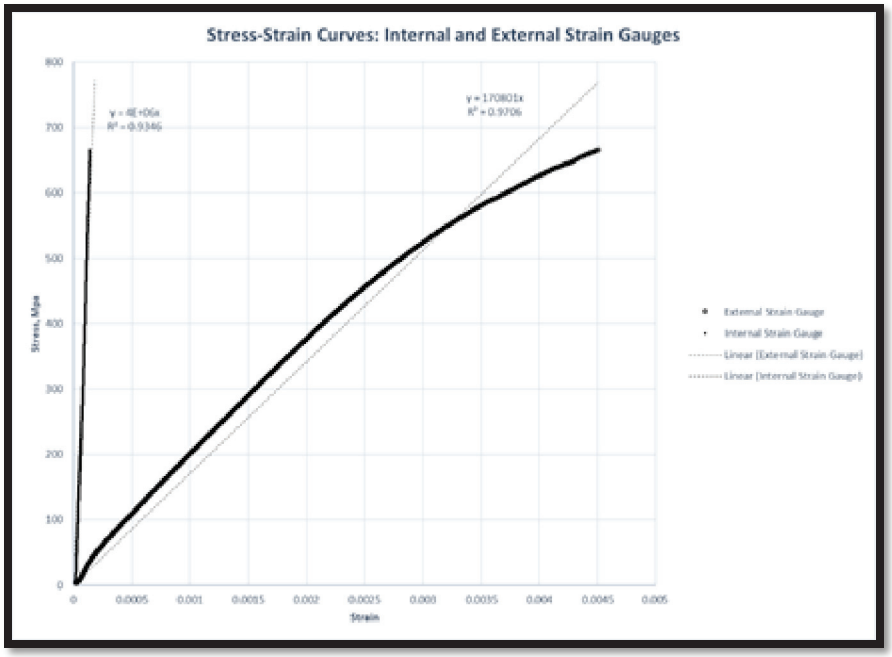


*Figure 27: Stress-strain curve from integrated and control sensors*

The work of a DED produced structure with an integrated sensor, as a proof of concept, and should be considered a success. While the integrated strain gauge did not respond to the same values as the validation gauge, it did respond linearly. The exact cause for why the internal sensor did not behave as the validation sensor is still unknown currently. A couple possible reasons could be thermal damage to the strain grid or loosening of the adhesive connection between the strain gauge and tensile bar. Even with these apparent problems there is an upside. The strain gauge did vary linearly to the applied stress, so even if the values received are not accurate, it is not outside the realm of control. These received values still relay the state of stress within the structure as is, or a correction factor could be added to shift values to more palatable ones. Also, all of this was achieved on the first attempt of integrating a sensor within an additively built structure using inexpensive, off-

the-shelf gauges, and commonly available adhesive. This presents a viable new avenue for creating smart components, that should only get better with further refinement.

## *Integrated Sensor Tensile Bars: Version 2*

The build-up of the smart metal tensile bars began with preparation and mounting of a suitable build substrate. The build substrate was made of *300*-series stainless steel, large enough to accommodate building all *12* of the tensile bars and mounted directly to the machine table. The build starts with a base layer roughly *10%* larger (X-Y/transverse) and *1.5* mm thick (Z/longitudinal) than the intended tensile bars. This is a strategy borrowed from other additive manufacturing processes, namely, laser powder bed fusion (LPBF) and thermoplastic extrusion, to reduce the tendency for an additively produced object to peel from the substrate. The printing parameters were selected to produce consistent results and therefore did not require face milling after several layers to compensate for z-height drift. The main bodies of all the tensile bars were then printed on top of the base layer, and after initial printing these tensile bar main bodies were then machined to correct height and pocketed to accept the previously produced covers that included the printed sensors on the bottom surface.

*Table 6: DED printing parameters*

| Laser Power, W | Massflow Rate, g/min | Traverse Velocity, mm/min | Laser Spot Size, mm | Layer Height, mm | Hatch Spacing, mm |
|---|---|---|---|---|---|
| *375* | *3.23* | *209* | *1.7* | *0.802* | *1.020* |

At this point, a small piece of *40* µm thick zirconia (ENrG Inc., Thin E-Strate, USA) was cut and glued into the pocket (Figure 28). The intent of installing the zirconia was to add

some electrical insulation in the area of the solder pads. As it will be shown later, the ad hoc addition of this zirconia seems to have had no effect on the survivability of the sensor while being consolidated in the final cladding process. The covers of various thicknesses were placed in their receiving pockets where tolerances were such that a minimal clearance was maintained for good fit. It should be noted that even though these steps were performed by hand, for proof of concept, that there is nothing preventing the automation of these steps. Lastly, wire leads were attached to the sensor and secured on the build substrate for in situ monitoring during the final steps.

*Figure 28: Sensor plate integration at different stages. From left to right, tensile bar with empty cavity, bar with inserted sensor, bar after stitch welding, bar after gap deposition, bar after laser cladding consolidation and bar after final machining*

With the sensor plate inserted, laser cladding consolidation began and proceeded in five steps: *Stitch Welding*, *Gap Deposition*, *Cleanup Machining*, *Final Deposition*, and *Finish Machining*. The stitch weld process involves the laser but without any additional material being deposited and resulted in the cover being welded in place. Next, the gap cladding deposits material in the void space between the cover and the main body and provides a flat plane without voids to facilitate further deposition after an additional subtractive step (cleanup machining). The additive portion concluded with the final deposition of material

which consolidated the sensors within the tensile bars. The last step was to finish machine the tensile bars, ensuring dimensional accuracy and proper surface finish.

### In-Situ Results

After the main tensile bodies were completed, resistance data was measured from five of the tensile bars (bottom row in Figure 12) during the consolidation phase of the build (Stage D in Figure 11). The sensors in all tensile bars survived the stitch weld, gap deposition, and cleanup machining. However, only the thickest tensile bar at *2.25* mm thickness survived and continuously output data throughout the entire fabrication process. All other tensile bars provided continuous data up until the point of failure. The failures occurred when the temperature conditions created one of two situations as detailed in the section on solder pad reconditioning: (1) sensor failure due to the exposure to intense temperatures, or (2) lead wire disconnection due to solder liquidity.

All sensor data shown for the remainder of this report is based on scaled change of resistance ($\Delta\Omega$, $\Delta R$). The reasons for this data formatting include: (1) in general the sensor $\Delta R$ response is in the $m\Omega/\mu\Omega$ range and scaling helps identify trends, (2) each sensor inherently has a different baseline resistance and scaling allows for easier comparison, and lastly (3) as this objective is to provide a proof of concept, the actual resistance values are of a secondary nature when compared against sensor functionality and response.

Figure 29 shows the in-situ data collected from the *2.25* mm tensile bar that survived and was measured during the entire laser cladding consolidation stage. The top of the figure shows the entire data stream received from the point of sensor insertion to the end of fabrication. The figure is broken down further into component parts illustrating each of the

previously described manufacturing steps. Stage *A* shows the temperature behavior of the stitch welding, *B* is gap deposition and *C* was the cleanup machining prior to the final deposition which shows relatively lower temperatures as expected. *D* shows the cyclic temperature of the laser cladding deposition as a response to the laser deposition scan strategy.

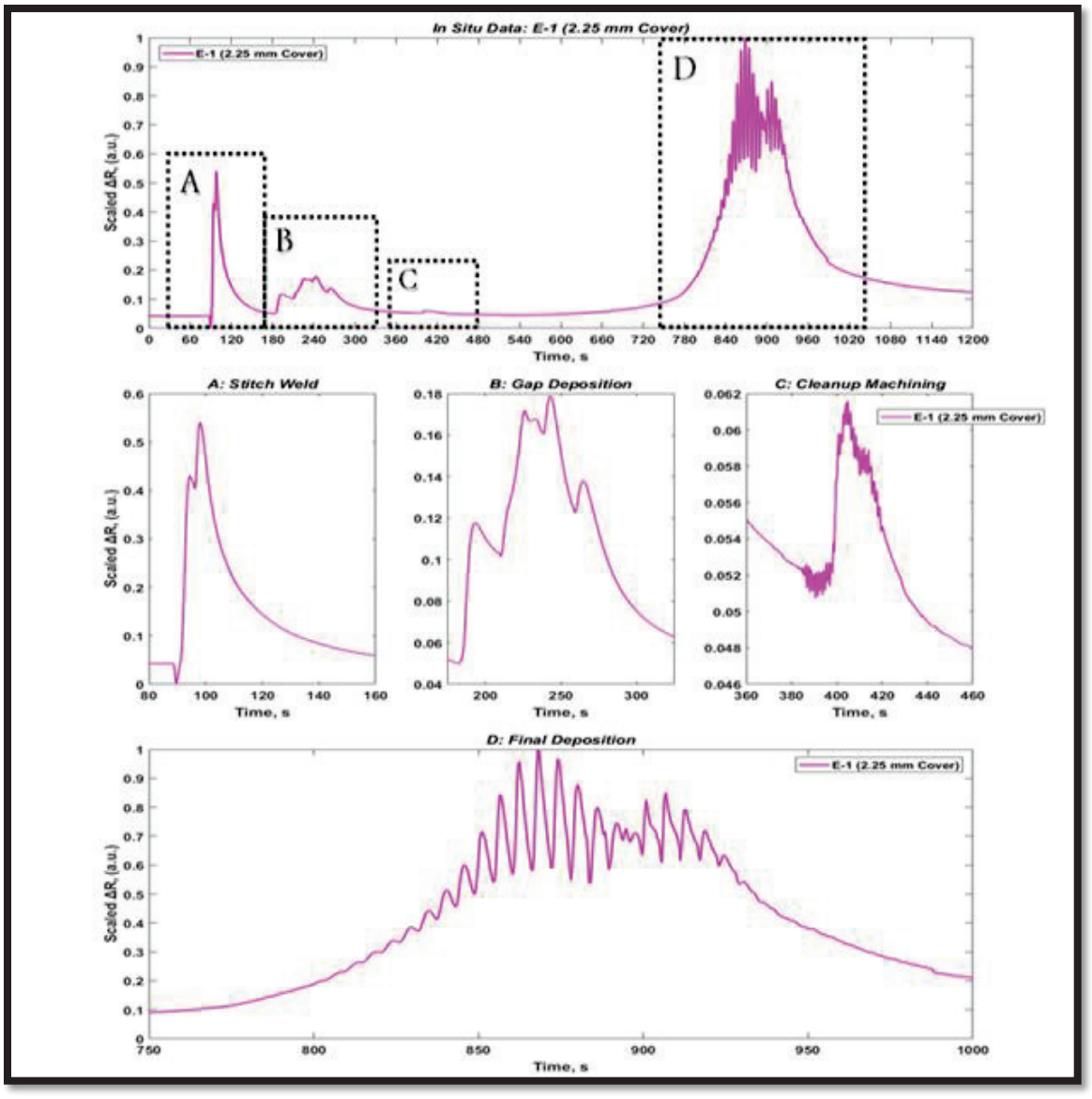


*Figure 29: In-situ sensor response to final manufacturing steps of the 2.25 mm plate*

Of note in the figure is the relative order-of-magnitude differences between all the processes, with the data exhibiting a strong temperature-time dependence. The addition of mass in the gap deposition does in some way insulate the tensile bar from temperature when compared to the previous stitch welding process, where both processes use the same laser power. During the cleanup machining, the vibrational nature of the milling process is detected as small amplitude oscillations. Finally, close inspection of the final deposition reveals a frequency that is consistent with the laser scan strategy. The deposition traverse speed coupled with the average peak-to-peak frequency gives approximately *22* mm of traverse distance between peaks compared to the average tensile bar width of *19* mm. This shows good agreement between the sensor data and the deposition process. The slight discrepancy can be accounted for by traverse time between laser scans when the laser system is off. The sensor design, with proper protection, could be well suited for evaluation of thermal DED models of in envelope processes conditions and process validation for structure qualification.

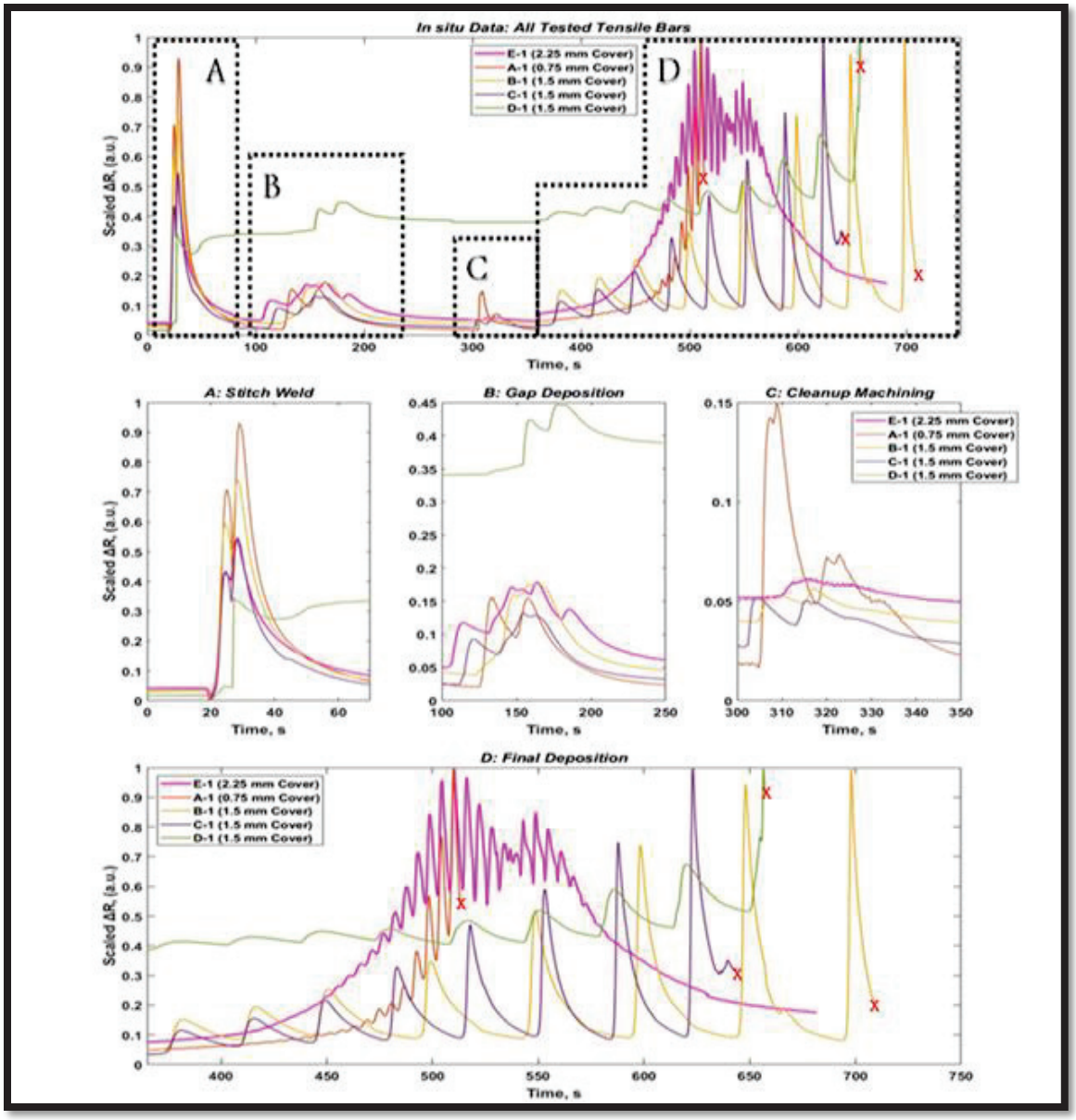


*Figure 30: All other in-situ tensile bar data*

The in-situ data acquired from each of the tensile bars is shown in Figure 30. All of the bars tested survived the first three consolidation steps: stitch weld, gap deposition, and cleanup machining. The data received during the first three steps is consistent to each other and to the *2.25* mm sample. Only sample *D-1* failed during the stitch weld and never returned to a baseline resistance. It is believed that residual stresses were relieved during

the stitch weld. This led to the sensor in effect being "pre-strained" and therefore had a loss of sensitivity in $\Delta R$. This is seen is a lack of intensity in the gap deposition and final deposition data, and the complete lack of response to cleanup machining.

During the final deposition stage, the higher frequency traces (*A-1* and *E-1*) represent laser scans traversing perpendicular to the long axis of the tensile bar while the lower frequency traces (*B-1*, *C-1*, and *D-1*) are laser scans traversing parallel to the long axis. The shorter distance traversed by the laser scanning the perpendicular axis results in a higher frequency of thermal events. It was only during the final deposition that samples *A-1* through *D-1* succumbed to the intense thermal conditions. A red *X* indicates the time at which data stopped transmitting. Sample *E-1* returned to baseline after the final deposition stage and continued to transmit data.

### Solder Pad Reconditioning

After final consolidation, machining, and removal from the substrate, most, if not all, of the lead wires had become decoupled from their respective tensile bar. Little could be seen from the small access slot, so a relief pocket was machined into the tensile bar so that a direct sightline could be established for visual confirmation of the sensor solder pad status. Figure 31 confirmed the assumptions of these authors that not much was left of the sensor solder pads, although most of the original screen-printed conductor remained. Their condition at that time required an ad hoc solution to reestablish an electrical connection to the embedded sensor.

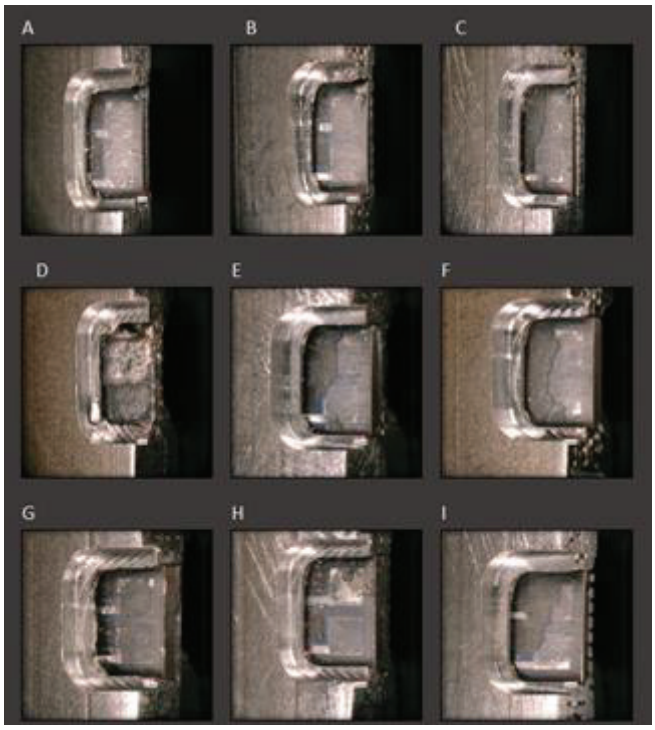


*Figure 31: Solder pads after consolidation and relief pocket machined for viewing and reconditioning*

Upon closer inspection of the tensile bars, Figure 31-*A,B* (both *1.5* mm thick covers) shows broken conductive traces, Figure 31-*C,E,F,I* (all *1.5* mm thick covers) have broken base installation layers, and Figure 31-*D* (*0.75* mm thick cover) shows a partial cover failure. Figure 30-G, H seemed to be in the best condition only showing signs of temperature caused solder liquidity. Thorough testing of each of the tensile bars with fine lead wires and a digital multimeter was conducted to determine if electrical continuity could be restored and it was found that the two samples with *2.25* mm thick covers (Figure 31-*G, H*) were salvageable. Only nine tensile bars are shown in Figure 31 the *10th* was excluded because during consolidation the entire cover failed, and the tensile bar became a single block of metal.

Once the salvageable tensile bars were identified, a plan for reconditioning the solder pads and providing connections to the sensor was implemented. The use of a low temperature curing silver conductor (Dupont, PE828) was settled upon. Shown in Figure 32-*A* is the first application of this silver conductor in the size and shape of the original solder pads. After drying for *24* hours continuity was checked, and there was success. Later, with a larger area on which to apply wire leads, assessing how these connections could be accomplished and was the subject of a few trial and error attempts. The main issue encountered was that the silver conductor itself can really bear no stress therefore connecting the wires directly was not possible. The final iteration of reconditioning was using layers of non-conductive epoxy (Loctite, Quick Set Epoxy) on the side of the tensile bar as a means of providing strain relief to eliminate any stress where the wire leads contact the silver conductor. These lead wires were affixed in that epoxy and bent to make contact with the silver conductor. Additional layers of silver conductor were applied to encapsulate the wire leads as shown in Figure 32-*B*. The solder pad reconditioning process worked and yielded an adequately robust solution.

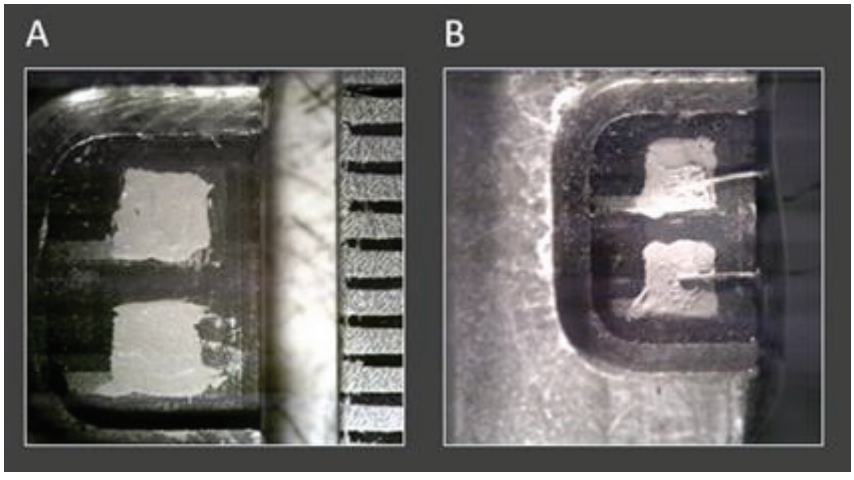


*Figure 32: Solder pad reconditioning*

## After-Fabrication Response to Applied Stress

The final test of this project was to assess the embedded sensors' ability to respond to an applied stress in the tensile bar after manufacturing. A universal testing machine (Instron, 5500R) was used to apply to cyclic load that varied between *25* MPa and *125* MPa over the course of three cycles (Table 7). Data acquisition of the sensor during the test was delicate due to the small changes in resistance of the sensor. Two different forms of data acquisition were used for the embedded sensor: (1) video (Samsung, Galaxy S8, KOR) and, (2) DAQ (National Instruments, NI-DAQ, USA). Resistance measurements taken by video were sampled at a per second basis while the DAQ recorded at *10* samples per second. Output from the load cell of the universal testing machine was also at *10* samples per second. The load cell data and sensor data had to be combined post-test as they recorded on separate instruments. Care was taken during the test to eliminate as much mismatch in time between the two data sources as possible.

*Table 7: Applied stress experiment specifics*

| Cycles, # | Minimum Stress, MPa | Maximum Stress, MPa |
|---|---|---|
| *3* | *25* | *125* |

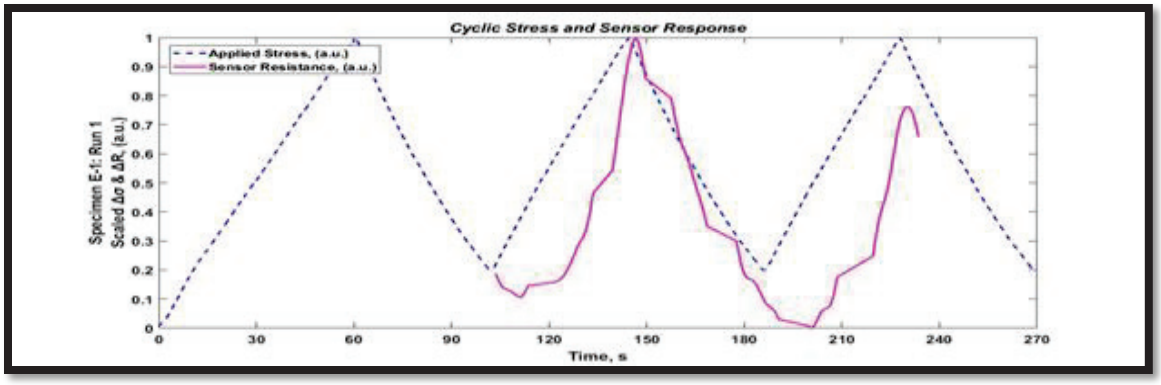


*Figure 33: Sample* A *(*2.25 *mm cover - specimen* E-1*) sensor response*

Figure 33 and Figure 34 show that in both *2.25* mm tensile bars the embedded sensors successfully respond to a cyclic applied stress. Figure 33 is the first data run of specimen *E-1* and was recorded by video. Multiple data runs (six) were attempted on this tensile bar, but again the delicate nature meant that only one run was captured before the embedded sensor lost continuity. The segmented nature of the sensor response is due to the sampling rate, especially when compared to the sampling rate of the DAQ. Figure 34 shows the two data runs for the second *2.25* mm tensile bar, specimen *E-2*, where the sensor data was captured via the DAQ. Only two data runs were attempted with Sample *B* as the ability to be tested persisted. The only particular trends seen in this data is some latency in the embedded sensor as it responds to the cyclic stress.

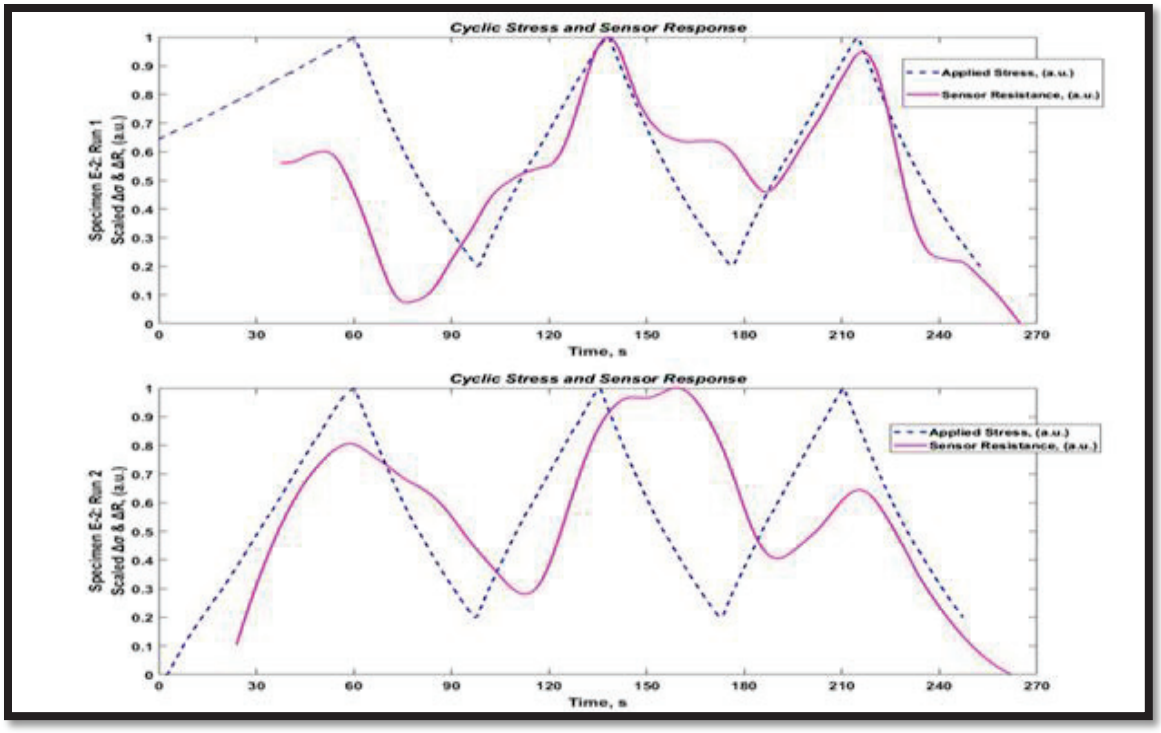


*Figure 34: Sample* B *(*2.25 *mm Cover, specimen* E-2*) sensor response runs* 1 *and* 2

## *Closing Remarks*

Access to intermediate stages of a build by interrupting an additive manufacturing process for embedding components within the structure is not a new idea. However, integrating sensors into high-value metal components is a new, interesting area of research. This represents a new paradigm where parts can have an intelligent, value-added component that can report back status to maintenance personnel.

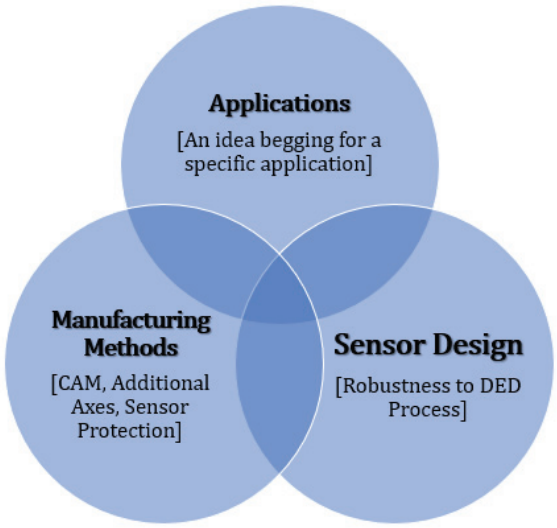


*Figure 35: Venn-style relationship of factors for hybrid DED smart structures*

The above Venn diagram (Figure 35) illustrates both the current state, and/or roadblocks, and future work required to implement successful hybrid DED smart structures. Addressing the sensor design portion of the diagram, the studies performed at Youngstown State in this work have tackled three different sensors, each with their own pros and cons. The passive, screen-printed sensor proved to be the most robust to consolidation within a metal structure. This sensor can be further refined. The layer thickness of the screen-printed sensor can be decreased and will lead to less foreign matter integrated into the steel structure. The simple resistor structure can be extended to a temperature compensated sensor structure with a design consisting of two sensing grids, which are placed at 90-degree angles to one another. In a stressed object, such as a tensile bar, the longitudinal-disposed strain gauge shows higher sensitivity than the transversal-disposed strain gauge. Both would be in close proximity to each other and would be exposed to similar temperatures. With this two-sensor approach, a half- or full bridge could be printed directly on the substrate for temperature compensation. Evident is also the need to tailor the

resistance and sensitivity of the screen-printed sensor away from the mΩ/μΩ range. The passive, off-the-shelf strain gage surprisingly survived the process though heat damage to the sensor and/or adhesive degradation led to a mismatch in the data between the embedded and the control sensor. Changing how the sensor is affixed to the substrate by use of epoxy could alleviate the adhesive degradation through heating. However, care is needed to not induce stress with a brittle epoxy, but rather finding one with appropriate thermal resistance that closely matches the thermal expansion coefficient of the base material. These actions could increase the viability of the low cost, readily available sensor. The Bluetooth sensor with its enhanced, active capabilities is intriguing from the standpoint of novel, structural health monitoring applications, yet that sensor required heavy, thick shielding to survive the consolidation process. A couple of methods which could reduce the shieling required are (1) ceramic shielding of the sensor much in the same way spacecraft are shielded from heat during reentry into the Earth's atmosphere, (2) conformal cooling of the substrate at rates which limit thermal exposure the sensor receives. In general, for future work either the sensor architecture can be changed to specifically handle the thermal exposure during consolidation or novel protection strategies can be developed to incorporate sensors already available and this leads to the portion of the Venn diagram: Manufacturing Methods. As previously described, generating toolpaths through CAM in these studies was tedious at best. The construction and manipulation of toolpaths through CAM represents the single largest area for improvement within directed energy deposition. It cannot be overstated that CAM is the biggest roadblock to realizing hybrid manufacturing capability. Closed loop controls and additional axes to better manage laser processing conditions will also improve the process, but only up to the point where that energy can be directed in a useful manner

through toolpathing strategies and flexibility. The last portion of the Venn diagram is that of applications. Currently what has been presented here is base research exploring the possibility of embedding sensors within metallic structures and even though more base research will be required what will push this technology forward is an application. An application provides a context for understanding that simply cannot be explained through base research and allows the mind a concrete grounding of the technology. This technology seeks an application to illustrate the "1+1=3" capability that is possible with structural health monitoring through hybrid DED.

## *Presentations and Publications Related to this Research*

Michael Juhasz, Michael Maravola, Peter-Jon Solomon, Pedro Cortes, Eric MacDonald, Jason Jones. Jason Walker, and Brett Conner. "Multi-Materials and Multi-Functionality Enabled by Hybrid Additive Manufacturing." Submitted to the International Journal of Additive and Subtractive Materials Manufacturing (IJASMM). In Review.

Michael Juhasz, Rico Tiedemann, Gerrit Dumstorff, Brett Conner, Walter Lang, and Eric MacDonald. "Hybrid Directed Energy Deposition for Fabricating Metal Structures with Embedded Sensors." Submitted to Elsevier Additive Manufacturing. In Review.

Michael Juhasz, Jason Walker, and Brett Conner. "Characterization of Precipitation Hardening 13-8 Stainless Steel Fabricated with Hybrid-DED Manufacturing." Presentation. Materials Science & Technology 2017, Symposium: Additive Manufacturing of Metals: Microstructure and Material Properties. October 2017.

Michael Juhasz, Jason Walker, and Brett Conner. "Effect of Processing Parameters on Microstructure of PH 13-8 Stainless Steel Fabricated by Hybrid DED/CNC Manufacturing." Presentation. 2018 TMS Annual Meeting & Exhibition, Symposium: Additive Manufacturing of Metals: Establishing Location Specific, Processing-Microstructure-Property-Relationships III. March 2018.

Michael Juhasz, Rico Tiedemann, Gerrit Dumstorff, Jason Walker, Brett Conner, Walter Lang, and Eric MacDonald. "Hybrid Directed Energy Deposition for Smart Structural Elements." Presentation. 2018 Annual International Solid Freeform Fabrication Symposium (SFF Symp 2018), Special Session: Hybrid AM Processes 3 - Hybrid Materials, Structures, Functions. August 2018.

Michael Juhasz, Rico Tiedemann, Gerrit Dumstorff, Jason Walker, Brett Conner, Eric MacDonald, and Walter Lang. “Smart Metal Structures with Embedded Strain Sensing Enabled by Hybrid Manufacturing.” Presentation. 2019 Annual International Solid Freeform Fabrication Symposium (SFF Symp 2019), Special Session: Hybrid AM III - Materials, Structures, Function. August 2019.

## *References*


Amine, Tarak, Joseph W. Newkirk, and Frank Liou. 2014. “An Investigation of the Effect of Direct Metal Deposition Parameters on the Characteristics of the Deposited Layers.” *Case Studies in Thermal Engineering* 3 (July): 21–34.

Ansari, M., R. Shoja Razavi, and M. Barekat. 2016. “An Empirical-Statistical Model for Coaxial Laser Cladding of NiCrAlY Powder on Inconel 738 Superalloy.” *Optics & Laser Technology* 86 (December): 136–44.

ASM International, ed. 1990. *ASM Handbook*. 10th ed. Materials Park, OH: ASM International.

Astm, I. 2016. “ASTM E8/E8M-16a: Standard Test Methods for Tension Testing of Metallic Materials.” *West Conshohocken, PA, USA: ASTM International*.

Astm, Iso. 2015. “ASTM52900-15 Standard Terminology for Additive Manufacturing—General Principles—Terminology.” *ASTM International, West Conshohocken, PA*.

Atwood, C., M. Ensz, D. Greene, M. Griffith, and L. Harwell. 1998. “Laser Engineered Net Shaping (LENS (TM)): A Tool for Direct Fabrication of Metal Parts.” https://www.osti.gov/biblio/1549.

Bai, Er-Wei. 1998. “An Optimal Two-Stage Identification Algorithm for Hammerstein--Wiener Nonlinear Systems.” *Automatica: The Journal of IFAC, the International Federation of Automatic Control* 34 (3): 333–38.

Balla, Vamsi Krishna, Partha P. Bandyopadhyay, Susmita Bose, and Amit Bandyopadhyay. 2007. “Compositionally Graded Yttria-Stabilized Zirconia Coating on Stainless Steel Using Laser Engineered Net Shaping (LENS$^{TM}$).” *Scripta Materialia* 57 (9): 861–64.

Balla, Vamsi Krishna, Susmita Bose, and Amit Bandyopadhyay. 2008. “Processing of Bulk Alumina Ceramics Using Laser Engineered Net Shaping.” *International Journal of Applied Ceramic Technology* 5 (3): 234–42.

Balla, Vamsi Krishna, Paul Duteil DeVasConCellos, Weichang Xue, Susmita Bose, and Amit Bandyopadhyay. 2009. “Fabrication of Compositionally and Structurally Graded Ti--TiO 2 Structures Using Laser Engineered Net Shaping (LENS).” *Acta Biomaterialia* 5 (5): 1831–37.

Bohrer, Markus, Heinz Basalka, Wolf Birner, Klaus Emiljanow, Martin Goede, and Stefan Czerner. 2002. “Turbine Blade Repair with Laser Powder Fusion Welding and Shape Recognition.” In *International Conference OF Metal Powder Deposition for Rapid Manufacturing, San Antonio*.

Bournias-Varotsis, Alkaios, Xiaoxiao Han, Russell A. Harris, and Daniel S. Engstrøm. 2019. “Ultrasonic Additive Manufacturing Using Feedstock with Build-in Circuitry for 3D Metal Embedded Electronics.” *Additive Manufacturing* 29 (October): 100799.

Bournias-Varotsis, Alkaios, Shanda Wang, David Hutt, and Daniel S. Engstrøm. 2018.

"The Effect of Ultrasonic Additive Manufacturing on Integrated Printed Electronic Conductors." *Electronic Materials Letters* 14 (4): 413–25.

"CAM-IT." n.d. CAM-IT. Accessed October 21, 2019. http://cam-it.us/.

Carroll, Beth E., Richard A. Otis, John Paul Borgonia, Jong-Ook Suh, R. Peter Dillon, Andrew A. Shapiro, Douglas C. Hofmann, Zi-Kui Liu, and Allison M. Beese. 2016. "Functionally Graded Material of 304L Stainless Steel and Inconel 625 Fabricated by Directed Energy Deposition: Characterization and Thermodynamic Modeling." *Acta Materialia* 108 (April): 46–54.

Chryssolouris, G., S. Zannis, K. Tsirbas, and C. Lalas. 2002. "An Experimental Investigation of Laser Cladding." *CIRP Annals* 51 (1): 145–48.

Colaco, R., T. Carvalho, and R. Vilar. 1994. "Laser Cladding of Stellite 6 on Steel Substrates." *High Temperature Chemical Processes* 3: 21–29.

Costa, Lino, Imre Felde, Tamás Réti, Zoltán Kálazi, Rogerio Colaço, Rui Vilar, and Balázs Verő. 2003. "A Simplified Semi-Empirical Method to Select the Processing Parameters for Laser Clad Coatings." *Materials Science Forum* 414-415 (January): 385–94.

"DA14583 IoT Sensor Development Kit." n.d. Accessed December 3, 2019. https://www.mouser.com/new/dialog-semiconductor/dialog-da14583-kit/.

DebRoy, T., H. L. Wei, J. S. Zuback, T. Mukherjee, J. W. Elmer, J. O. Milewski, A. M. Beese, A. Wilson-Heid, A. De, and W. Zhang. 2017. "Additive Manufacturing of Metallic Components--Process, Structure and Properties." *Progress in Materials Science*. https://www.sciencedirect.com/science/article/pii/S0079642517301172.

Dickens, P. M., M. S. Pridham, R. C. Cobb, I. Gibson, and G. Dixon. 1992. "Rapid Prototyping Using 3-D Welding." In *1992 International Solid Freeform Fabrication Symposium*. repositories.lib.utexas.edu. https://repositories.lib.utexas.edu/handle/2152/64409.

Doebelin, Ernest O. 1995. *Engineering Experimentation: Planning, Execution, Reporting*. ernest otto doebelin.

Dumstorff, Gerrit, Christoph Pille, Rico Tiedemann, Matthias Busse, and Walter Lang. 2017. "Smart Aluminum Components: Printed Sensors for Integration into Aluminum during High-Pressure Casting." *Journal of Manufacturing Processes* 26 (April): 166–72.

Dumstorff, G., S. Paul, and W. Lang. 2014. "Integration Without Disruption: The Basic Challenge of Sensor Integration." *IEEE Sensors Journal* 14 (7): 2102–11.

El Cheikh, Hussam, Bruno Courant, Samuel Branchu, Jean-Yves Hascoët, and Ronald Guillén. 2012. "Analysis and Prediction of Single Laser Tracks Geometrical Characteristics in Coaxial Laser Cladding Process." *Optics and Lasers in Engineering* 50 (3): 413–22.

Ensz, Mark T., Michelle L. Griffith, and Daryl E. Reckaway. 2002. "Critical Issues for Functionally Graded Material Deposition by Laser Engineered Net Shaping (LENS)." In *Proceedings of the 2002 MPIF Laser Metal Deposition Conference*. San Antonio: TX. http://edge.cs.drexel.edu/GICL/people/schroeder/references/mpif02me.pdf.

Erfanmanesh, Mohammad, Hassan Abdollah-Pour, Hamidreza Mohammadian-Semnani, and Reza Shoja-Razavi. 2017. "An Empirical-Statistical Model for Laser Cladding of WC-12Co Powder on AISI 321 Stainless Steel." *Optics & Laser Technology* 97 (December): 180–86.

Fessler, J., A. Nickel, G. Link, F. Prinz, and P. Fussell. 1997. “Functional Gradient Metallic Prototypes through Shape Deposition Manufacturing.” In *1997 International Solid Freeform Fabrication Symposium*. repositories.lib.utexas.edu. https://repositories.lib.utexas.edu/handle/2152/71430.

Flynn, Joseph M., Alborz Shokrani, Stephen T. Newman, and Vimal Dhokia. 2016. “Hybrid Additive and Subtractive Machine Tools--Research and Industrial Developments.” *International Journal of Machine Tools & Manufacture* 101: 79–101.

Francis Reintjes, J. 1991. *Numerical Control: Making a New Technology*. Oxford University Press.

Ghazali, M. I. M., E. Gutierrez, J. C. Myers, A. Kaur, B. Wright, and P. Chahal. 2015. “Affordable 3D Printed Microwave Antennas.” In *2015 IEEE 65th Electronic Components and Technology Conference (ECTC)*, 240–46. ieeexplore.ieee.org.

Giachino, Joseph William, and William R. Weeks. 1985. *Welding Skills*. American Technical Publishers.

Gibson, Ian, David Rosen, and Brent Stucker. 2015. *Additive Manufacturing Technologies: 3D Printing, Rapid Prototyping, and Direct Digital Manufacturing*. Springer.

Griffith, M. L., L. D. Harwell, and J. T. Romero. 1997. “Multi-Material Processing by LENS.” *1997 International*. https://repositories.lib.utexas.edu/handle/2152/71406.

Griffith, M. L., D. M. Keicher, C. L. Atwood, J. A. Romero, J. E. Smugeresky, L. D. Harwell, and D. L. Greene. 1996. “Free Form Fabrication of Metallic Components Using Laser Engineered Net Shaping (LENS).” In *1996 International Solid Freeform Fabrication Symposium*. repositories.lib.utexas.edu. https://repositories.lib.utexas.edu/handle/2152/69929.

Gu, D. D., W. Meiners, K. Wissenbach, and R. Poprawe. 2012. “Laser Additive Manufacturing of Metallic Components: Materials, Processes and Mechanisms.” *International Materials Reviews* 57 (3): 133–64.

Guo, Z., and W. Sha. 2002. “Thermodynamic Calculation for Precipitation Hardening Steels and Titanium Aluminides.” *Intermetallics* 10 (10): 945–50.

Guo, Z., W. Sha, and D. Vaumousse. 2003. “Microstructural Evolution in a PH13-8 Stainless Steel after Ageing.” *Acta Materialia* 51 (1): 101–16.

Gursoz, E. Levent, Lee E. Weiss, and Fritz B. Prinz. 1990. “Geometric Modeling for Rapid Prototyping and Tool Fabrication.” In *1990 International Solid Freeform Fabrication Symposium*. repositories.lib.utexas.edu. https://repositories.lib.utexas.edu/handle/2152/64250.

Hahnlen, Ryan, and Marcelo J. Dapino. 2010. “Active Metal-Matrix Composites with Embedded Smart Materials by Ultrasonic Additive Manufacturing.” In *Industrial and Commercial Applications of Smart Structures Technologies 2010*, 7645:76450O. International Society for Optics and Photonics.

Hehr, Adam, Mark Norfolk, Justin Wenning, John Sheridan, Paul Leser, Patrick Leser, and John A. Newman. 2018. “Integrating Fiber Optic Strain Sensors into Metal Using Ultrasonic Additive Manufacturing.” *JOM*. https://doi.org/10.1007/s11837-017-2709-8.

Heigel, J. C., P. Michaleris, and E. W. Reutzel. 2015. “Thermo-Mechanical Model Development and Validation of Directed Energy Deposition Additive Manufacturing of Ti–6Al–4V.” *Additive Manufacturing* 5 (Supplement C): 9–19.

Hossain, Mohammad Shojib, Jose A. Gonzalez, Ricardo Martinez Hernandez, Mohammad Arif Ishtiaque Shuvo, Jorge Mireles, Ahsan Choudhuri, Yirong Lin, and Ryan B. Wicker. 2016. "Fabrication of Smart Parts Using Powder Bed Fusion Additive Manufacturing Technology." *Additive Manufacturing* 10 (April): 58–66.

Kaierle, Stefan, Alexander Barroi, Christian Noelke, Joerg Hermsdorf, Ludger Overmeyer, and Heinz Haferkamp. 2012. "Review on Laser Deposition Welding: From Micro to Macro." *Physics Procedia* 39 (January): 336–45.

Keist, Jayme, Karen Taminger, and Todd A. Palmer. 2016. "Structure-Property Correlations for Additively Manufactured Ti-6Al-4V Components Produced Using Directed Energy Deposition Processes." In *Proceedings of the 13th World Conference on Titanium*, 1395–1400. John Wiley & Sons, Inc.

Lauwers, Bert, Fritz Klocke, Andreas Klink, A. Erman Tekkaya, Reimund Neugebauer, and Don Mcintosh. 2014. "Hybrid Processes in Manufacturing." *CIRP Annals* 63 (2): 561–83.

Le, T., B. Song, Q. Liu, R. A. Bahr, S. Moscato, C. P. Wong, and M. M. Tentzeris. 2015. "A Novel Strain Sensor Based on 3D Printing Technology and 3D Antenna Design." In *2015 IEEE 65th Electronic Components and Technology Conference (ECTC)*, 981–86. ieeexplore.ieee.org.

Lewandowski, John J., and Mohsen Seifi. 2016. "Metal Additive Manufacturing: A Review of Mechanical Properties." *Annual Review of Materials Research* 46 (1): 151–86.

Lewis, Gary K., and Eric Schlienger. 2000. "Practical Considerations and Capabilities for Laser Assisted Direct Metal Deposition." *Materials & Design* 21 (4): 417–23.

Li, J., T. Monaghan, T. T. Nguyen, R. W. Kay, R. J. Friel, and R. A. Harris. 2017. "Multifunctional Metal Matrix Composites with Embedded Printed Electrical Materials Fabricated by Ultrasonic Additive Manufacturing." *Composites Part B Engineering* 113 (March): 342–54.

Liu, Qingbin, Ming C. Leu, and Stephen M. Schmitt. 2006. "Rapid Prototyping in Dentistry: Technology and Application." *International Journal of Advanced Manufacturing Technology* 29 (3): 317–35.

Li, Wei, Jingwei Zhang, Xinchang Zhang, and Frank Liou. 2017. "Effect of Optimizing Particle Size on Directed Energy Deposition of Functionally Graded Material with Blown Pre-Mixed Multi-Powder." *Manufacturing Letters* 13 (August): 39–43.

Li, Xiaochun, Anastasios Golnas, and Fritz B. Prinz. 2000. "Shape Deposition Manufacturing of Smart Metallic Structures with Embedded Sensors." In *Smart Structures and Materials 2000: Sensory Phenomena and Measurement Instrumentation for Smart Structures and Materials*, 3986:160–71. International Society for Optics and Photonics.

Lo, K. H., C. H. Shek, and J. K. L. Lai. 2009. "Recent Developments in Stainless Steels." *Materials Science & Engineering. R, Reports: A Review Journal* 65 (4): 39–104.

Lopes, Amit Joe, Eric MacDonald, and Ryan B. Wicker. 2012. "Integrating Stereolithography and Direct Print Technologies for 3D Structural Electronics Fabrication." *Rapid Prototyping Journal* 18 (2): 129–43.

Lorenz, K. A., J. B. Jones, D. I. Wimpenny, and M. R. Jackson. 2015. "A Review of Hybrid Manufacturing." In *Solid Freeform Fabrication Conference Proceedings*. Vol. 53. sffsymposium.engr.utexas.edu.

http://sffsymposium.engr.utexas.edu/sites/default/files/2015/2015-8-Lorenz.pdf.
Lupoi, R., and W. O'Neill. 2010. "Deposition of Metallic Coatings on Polymer Surfaces Using Cold Spray." *Surface and Coatings Technology* 205 (7): 2167–73.
Lyke, J. C. 2012. "Plug-and-Play Satellites." *IEEE Spectrum* 49 (8): 36–42.
MacDonald, Eric, and Ryan Wicker. 2016. "Multiprocess 3D Printing for Increasing Component Functionality." *Science* 353 (6307). https://doi.org/10.1126/science.aaf2093.
Macdonald, E., R. Salas, D. Espalin, M. Perez, E. Aguilera, D. Muse, and R. B. Wicker. 2014. "3D Printing for the Rapid Prototyping of Structural Electronics." *IEEE Access* 2 (December): 234–42.
Machlis, S. 1990. "How To Bring CAD To Life." *Design News, March*.
Matsui, Shinji, Takashi Kaito, Jun-Ichi Fujita, Masanori Komuro, Kazuhiro Kanda, and Yuichi Haruyama. 2000. "Three-Dimensional Nanostructure Fabrication by Focused-Ion-Beam Chemical Vapor Deposition." *Journal of Vacuum Science & Technology. B, Microelectronics and Nanometer Structures: Processing, Measurement, and Phenomena: An Official Journal of the American Vacuum Society* 18 (6): 3181–84.
Merriam-Webster, Merriam-Webster's Collegiate. 1977. "Dictionary." *Springfield, Massachusetts, USA: G & C Merriam Company* 830. http://swt3.vatitude.com/qql/slot/u423/SJIJ%20Experience/E3%20Programme/Downloads/Apps%20to%20download%20(ver%20231213).pdf.
Mirzaee, Milad. 2015. "Developing Novel 3D Antennas Using Advanced Additive Manufacturing Technology." The University of North Dakota. http://search.proquest.com/openview/c5a267d01bd137d39f80750098e0086f/1?pq-origsite=gscholar&cbl=18750&diss=y.
Mondal, Subrata, Asish Bandyopadhyay, and Pradip Kumar Pal. 2014. "Application of Artificial Neural Network for the Prediction of Laser Cladding Process Characteristics at Taguchi-Based Optimized Condition." *International Journal of Advanced Manufacturing Technology* 70 (9): 2151–58.
Murphy, M. L., W. M. Steen, and C. Lee. 1994. "The Rapid Manufacture of Metallic Components by Laser Surface Cladding." *Laser Assisted Net Shape Engineering, Proceedings of the LANE'94* 2: 803–14.
Nabhani, Mohammad, Reza Shoja Razavi, and Masoud Barekat. 2018. "An Empirical-Statistical Model for Laser Cladding of Ti-6Al-4V Powder on Ti-6Al-4V Substrate." *Optics & Laser Technology* 100 (March): 265–71.
Nassar, A. R., T. J. Spurgeon, and E. W. Reutzel. 2014. "Sensing Defects during Directed-Energy Additive Manufacturing of Metal Parts Using Optical Emissions Spectroscopy." In *Solid Freeform Fabrication Symposium Proceedings*. University of Texas Austin, TX. http://sffsymposium.engr.utexas.edu/sites/default/files/2014-024-Nassar.pdf.
Ocelík, V., U. de Oliveira, M. de Boer, and J. Th M. de Hosson. 2007. "Thick Co-Based Coating on Cast Iron by Side Laser Cladding: Analysis of Processing Conditions and Coating Properties." *Surface and Coatings Technology* 201 (12): 5875–83.
Oliveira, U. de, V. Ocelík, and J. Th M. De Hosson. 2005. "Analysis of Coaxial Laser Cladding Processing Conditions." *Surface and Coatings Technology* 197 (2): 127–36.
Padilha, A. F., R. L. Plaut, and P. R. Rios. n.d. "[No Title]." Accessed December 3, 2019. https://www.researchgate.net/profile/Angelo_Padilha/publication/293106894_Stainl

ess_steels_heat_treatment_Chapter_12/links/5a83a35c45851504fb3a6755/Stainless-steels-heat-treatment-Chapter-12.pdf.
Peckner, Donald, and I. M. Bernstein, eds. 1977. *Handbook of Stainless Steels*. New York: McGraw-Hill.
Pelletier, J. M., M. C. Sahour, M. Pilloz, and A. B. Vannes. 1993. "Influence of Processing Conditions on Geometrical Features of Laser Claddings Obtained by Powder Injection." *Journal of Materials Science* 28 (19): 5184–88.
Petrat, Torsten, Robert Kersting, Benjamin Graf, and Michael Rethmeier. 2018. "Embedding Electronics into Additive Manufactured Components Using Laser Metal Deposition and Selective Laser Melting." *Procedia CIRP*. https://doi.org/10.1016/j.procir.2018.08.071.
Pinkerton, Andrew J. 2015. "Advances in the Modeling of Laser Direct Metal Deposition." *Journal of Laser Applications* 27 (S1): S15001.
Prinz, Fritz B., Lee E. Weiss, and Daniel P. Siewiorek. 1994. Electronic packages and smart structures formed by thermal spray deposition. USPTO 5278442. *US Patent*, filed July 15, 1991, and issued January 11, 1994. https://www.google.com/patents/US5278442.
Qian, M., and F. H. Froes. 2015. *Titanium Powder Metallurgy: Science, Technology and Applications*. Elsevier Science.
Qian, M., L. C. Lim, Z. D. Chen, and W. I. Chen. 1997. "Parametric Studies of Laser Cladding Processes." *Journal of Materials Processing Technology* 63 (1): 590–93.
Robino, C. V., M. J. Cieslak, P. W. Hochanadel, and G. R. Edwards. 1994. "Heat Treatment of Investment Cast PH 13-8 Mo Stainless Steel: Part II. Isothermal Aging Kinetics." *Metallurgical and Materials Transactions A* 25 (4): 697–704.
San Martin, D., P. E. J. Rivera Diaz del Castillo, E. Peekstok, and S. van der Zwaag. 2007. "A New Etching Route for Revealing the Austenite Grain Boundaries in an 11.4% Cr Precipitation Hardening Semi-Austenitic Stainless Steel." *Materials Characterization* 58 (5): 455–60.
Schuh, Günther, Jennifer Kreysa, and Simon Orilski. 2009. "Roadmap „Hybride Produktion"." *ZWF Zeitschrift Für Wirtschaftlichen Fabrikbetrieb* 104 (5): 385–91.
Sealy, Michael P., Gurucharan Madireddy, Robert E. Williams, Prahalada Rao, and Maziar Toursangsaraki. 2018. "Hybrid Processes in Additive Manufacturing." *Journal of Manufacturing Science and Engineering* 140 (6). https://doi.org/10.1115/1.4038644.
Seetharaman, V., M. Sundararaman, and R. Krishnan. 1981. "Precipitation Hardening in a PH 13-8 Mo Stainless Steel." *International Journal of Green Nanotechnology: Materials Science and Engineering* 47 (1): 1–11.
Shamsaei, Nima, Aref Yadollahi, Linkan Bian, and Scott M. Thompson. 2015. "An Overview of Direct Laser Deposition for Additive Manufacturing; Part II: Mechanical Behavior, Process Parameter Optimization and Control." *Additive Manufacturing* 8 (October): 12–35.
Shemelya, C., L. Banuelos-Chacon, A. Melendez, C. Kief, D. Espalin, R. Wicker, G. Krijnen, and E. MacDonald. 2015. "Multi-Functional 3D Printed and Embedded Sensors for Satellite Qualification Structures." In *SENSORS, 2015 IEEE*, 1–4. ieeexplore.ieee.org.
Shemelya, C., F. Cedillos, E. Aguilera, E. Maestas, J. Ramos, D. Espalin, D. Muse, R. Wicker, and E. MacDonald. 2013. "3D Printed Capacitive Sensors." In *SENSORS,*

*2013 IEEE*, 1–4. ieeexplore.ieee.org.
Smid, Peter. 2003. *CNC Programming Handbook: A Comprehensive Guide to Practical CNC Programming*. Industrial Press Inc.
Sova, A., S. Grigoriev, A. Okunkova, and I. Smurov. 2013. "Potential of Cold Gas Dynamic Spray as Additive Manufacturing Technology." *International Journal of Advanced Manufacturing Technology* 69 (9): 2269–78.
Spencer, J. D., P. M. Dickens, and C. M. Wykes. 1998. "Rapid Prototyping of Metal Parts by Three-Dimensional Welding." *Proceedings of the Institution of Mechanical Engineers, Part B: Journal of Engineering Manufacture* 212 (3): 175–82.
Taminger, Karen M., and Robert A. Hafley. 2006. "Electron Beam Freeform Fabrication for Cost Effective Near-Net Shape Manufacturing." NASA. https://ntrs.nasa.gov/search.jsp?R=20080013538.
Thompson, Scott M., Linkan Bian, Nima Shamsaei, and Aref Yadollahi. 2015. "An Overview of Direct Laser Deposition for Additive Manufacturing; Part I: Transport Phenomena, Modeling and Diagnostics." *Additive Manufacturing* 8 (October): 36–62.
Toyserkani, Ehsan, and Amir Khajepour. 2006. "A Mechatronics Approach to Laser Powder Deposition Process." *Mechatronics: The Science of Intelligent Machines* 16 (10): 631–41.
Toyserkani, Ehsan, Amir Khajepour, and Stephen F. Corbin. 2004. *Laser Cladding*. CRC Press.
Toyserkani, Ehsan, Amir Khajepour, and Steve Corbin. 2003. "Three-Dimensional Finite Element Modeling of Laser Cladding by Powder Injection: Effects of Powder Feedrate and Travel Speed on the Process." *Journal of Laser Applications* 15 (3): 153–60.
Wang, Fude, Stewart Williams, Paul Colegrove, and Alphons A. Antonysamy. 2013. "Microstructure and Mechanical Properties of Wire and Arc Additive Manufactured Ti-6Al-4V." *Metallurgical and Materials Transactions A* 44 (2): 968–77.
Wang, Zhuqing, Todd A. Palmer, and Allison M. Beese. 2016. "Effect of Processing Parameters on Microstructure and Tensile Properties of Austenitic Stainless Steel 304L Made by Directed Energy Deposition Additive Manufacturing." *Acta Materialia* 110 (Supplement C): 226–35.
Ward, John E. 1959. "Automatic Programming of Numerically Controlled Machine Tools." MASSACHUSETTS INST OF TECH CAMBRIDGE ELECTRONIC SYSTEMS LAB. https://apps.dtic.mil/dtic/tr/fulltext/u2/241754.pdf.
Williams, K., J. Maxwell, K. Larsson, and M. Boman. 1999. "Freeform Fabrication of Functional Microsolenoids, Electromagnets and Helical Springs Using High-Pressure Laser Chemical Vapor Deposition." In *Technical Digest. IEEE International MEMS 99 Conference. Twelfth IEEE International Conference on Micro Electro Mechanical Systems (Cat. No.99CH36291)*, 232–37. ieeexplore.ieee.org.
Wirth, Florian, and Konrad Wegener. 2018. "A Physical Modeling and Predictive Simulation of the Laser Cladding Process." *Additive Manufacturing* 22 (August): 307–19.
Wu, Xinwei, Beidi Zhu, Xiaoyan Zeng, Xiang Hu, and Kun Cui. 1996. "Critical State of Laser Cladding with Powder Auto-Feeding." *Surface and Coatings Technology* 79 (1): 200–204.
Wu, Z., M. Liang, W. R. Ng, M. Gehm, and H. Xin. 2012. "Terahertz Horn Antenna Based

on Hollow-Core Electromagnetic Crystal (EMXT) Structure." *IEEE Transactions on Antennas and Propagation* 60 (12): 5557–63.

Xue, Lijue, and Mahmud U. Islam. 2006. "Laser Consolidation-a Novel One-Step Manufacturing Process for Making Net-Shape Functional Components." NATIONAL RESEARCH COUNCIL OF CANADA OTTAWA (ONTARIO). https://apps.dtic.mil/docs/citations/ADA521898.

Ya, Wei, B. Pathiraj, and Shaojie Liu. 2016. "2D Modelling of Clad Geometry and Resulting Thermal Cycles during Laser Cladding." *Journal of Materials Processing Technology* 230 (April): 217–32.

## Part 2: Ex-Situ Post-processing of Laser Powder Bed Fusion AlSi10Mg

### *Introduction*

Aircraft and airframes are currently flying much longer than their original design cycle. Maintenance and logistics are paramount for keeping these aircraft flying. The lengthened life of aircraft stresses the supply chain, as replacement parts are no longer being produced by the OEM. The bell crank for a specific aircraft was identified by the Air Force as a component that is difficult to obtain via conventional fabrication routes such as casting or machining. The bell crank is geometrically complex with numerous thick to thin transitions and angular features. The original component is cast A356 aluminum, but low part quantities, high tooling costs, and substantial lead time form the basis to seek alternative means of production. Laser Powder Bed Fusion (LPBF) is the AM technology chosen in this project to attempt replacement of the original cast component in the AM alloy AlSi10Mg. Aircraft componentry however must meet stringent requirements on properties and therefore the LPBF process, with a specific alloy system, must be qualified in order to allow for this replacement.

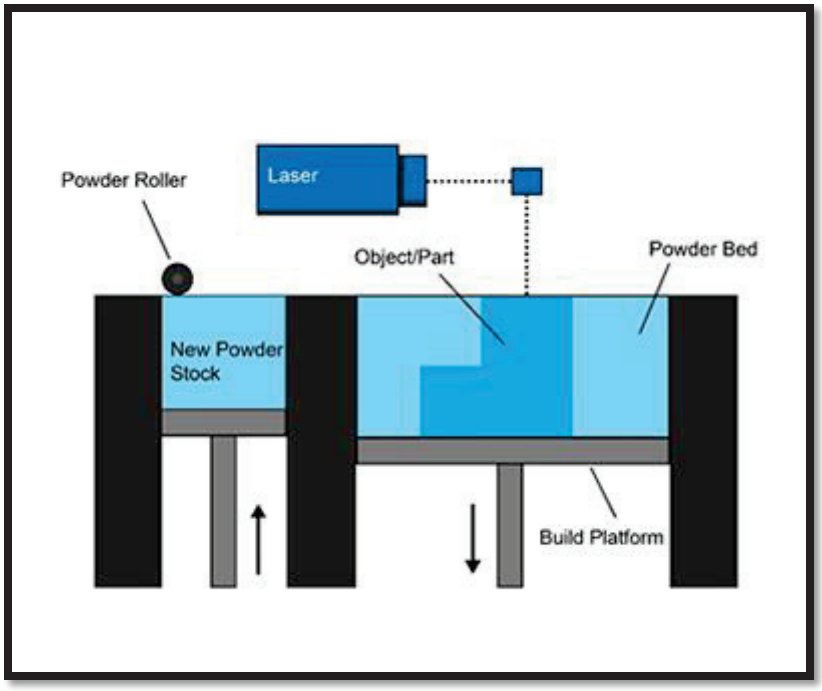


*Figure 36: Powder bed fusion process schematic ("Powder Bed Fusion | Additive Manufacturing Research Group | Loughborough University" n.d.)*

Powder Bed Fusion (PBF) as defined by ISO/ASTM is "an additive manufacturing process in which thermal energy selectively fuses regions of a powder bed." (Iso Astm 2015) PBF is a process in which loose powder is spread in a thin layer forming a bed and subsequently where focused energy is then used selectively to melt or to sinter a layer of powder only where required to produce the desired geometry. Full melting rather than sintering is more typical of metal powder systems.

This technology originated from work in the early 1980s at the University of Texas at Austin. This work was awarded a patent in 1989 (Deckard 1989; Bourell et al. 1990). Then in the mid-1990s, as part of a joint effort between EOS, the Fraunhofer Institute, and others, Selective Laser Melting (SLM) and Direct Metal Laser Sintering (DMLS) were developed in Germany (Shellabear and Nyrhilä 2004). The archetype of LPBF goes by several names

in the literature owing to efforts to commercialize the process. Powder Bed Fusion can also be known as: Selective Laser Sintering (SLS) (3D Systems Corporation) (Gu et al. 2012), Selective Laser Melting (SLM) (Frazier 2014), Direct Metal Laser Sintering (DMLS) (EOS GmbH) (Frazier 2014), Direct Metal Laser Remelting (DMLR) (Gu et al. 2012), Direct Metal Printing (DMP) (3D Systems Corporation), Electron Beam Additive Manufacturing (EBAM) (Gong, Anderson, and Chou 2014), Electron Beam Melting (EBM) (Arcam AB), High Speed Sintering (HSS) (Hopkinson and Erasenthiran 2004), LaserCUSING (Concept Laser GmbH) (Gu et al. 2012), Laser Metal Fusion (TRUMPF Laser Technology) (Candel-Ruiz, Kaufmann, and Müllerschön 2015; Geyer 2016), Micro Laser Sintering (MLS) (EOS GmbH) (Oberhofer, Göbner, and Büse 2014), Selective Electron Beam Melting (SEBM) (Heinl et al. 2007), and Selective Heat Sintering (SHS) (Baumers, Tuck, and Hague 2015).

Additive manufacturing is known for the ability to deliver geometric complexity for free, and while that statement needs to be tempered, PBF has been able to deliver some real benefits (Conner et al. 2014). The most publicized example is the successful creation of the GE LEAP fuel nozzle (Seifi et al. 2016). Its success can be attributed by the reduction of the number of parts (assemblies and sub-assemblies) versus the traditional counterpart, a reduction only achievable through additive manufacturing. While not exploiting geometric complexity, the LEAP nozzle does leverage benefits realizable in PBF. The collection of best practices and methodologies that resulted in the GE LEAP nozzle has come to be known as DfAM, or Design for Additive Manufacturing. DfAM has become its own subject area whose main constituents are light weighting, generative design, and assembly consolidation (Sönegard and Warholm 2017).

The broad strokes of the typical PBF build process starts with the depression of the build platform (on the order of tens of microns) to create a trough to accept and hold the loose powder. The recoater system then moves powder from a hopper and evenly distributes it over the build area, creating the powder bed. This layer of powder is then passed over by either a laser or electron beam which supplies significant heat to the powder. The powder is then either partially melted (sintered) or fully melted, to a point where the powder fuses to itself and to the layers below in accordance with the desired geometry. The build platform then changes height, a new layer of loose powder is deposited by the recoater system, and the process is repeated ad infinitum until the entire part is completed. While all PBF fusion techniques contain the above listed steps, the main differences between all the methods are the heat source employed, the envelope or enclosure environment, and the degree to which the loose powder is fused.

At present, the two favored heat sources for powder bed fusion are a laser or an electron beam. Other sources exist such as using a thermal print head (Baumers, Tuck, and Hague 2015), infrared lamps (Hopkinson and Erasenthiran 2004), and recently high intensity flash bulbs (Nauka, Kasperchik, and Hartman 2019), but these are mentioned in the interest of completeness and are the exception and not the rule. Electron beam heat sources require the entire build envelope to be under vacuum while laser sources have no such requirement for beam transmission. Electron beams are focused using magnetic lenses instead of optical lenses used for lasers and interact with materials differently than lasers (Elmer et al. 2009). The use of deflector coils in electron beam arrangements leads to a dramatic increase in scan speed due to the lack of mechanical parts to direct the beam. The beam in electron beam powder bed fusion (EBPBF) typically scans over the entire layer, preheating the

layer, before the specific geometry is fused. This is advantageous in reducing residual stress and can also be leveraged to control microstructure (Kahnert, Lutzmann, and Zaeh 2007; Gockel, Beuth, and Taminger 2014). However, this pre-sintering leads to additional time requirements for post-processing as finished components need either powder blasting, ultrasonic vibration, or some other form of mechanical removal of powder. This can be especially difficult with certain geometries like small cavities or narrow channels. Laser beam heat sources are best described as a balanced choice, mostly based on economy and robustness. Both laser and electron beams provide high peak power and can be focused to result in very high-power densities. The choice of an appropriate heat source for AM is a balance of multiple factors which must be weighed considering the final component to be produced.

Powders that are useful in additive manufacturing must meet several criteria. Myers investigated many aspects of AM powders and what parameters influence powder bed processes (Myers 2016). These characteristics include the morphology, size distribution, and flowability of the powders. Speaking generally, spherical powder flow and spread well, but can suffer from a low packing density, while faceted particles flow poorly but have excellent packing density. For AM purposes, spherical powder particles with a fixed size distribution is a good compromise between flowability and packing density and is the current industry standard (Sames et al. 2016). Scanning electron microscopy (SEM), X-ray and computed tomography (CT) are used to examine the morphology of the powder particles (Slotwinski et al. 2014). Size distributions can be ascertained by laser diffraction and sieving method, and flowability is measured by a Hall flow meter (Santomaso, Lazzaro, and Canu 2003; Slotwinski et al. 2014). All of these are factors that affect a good

quality powder where the material spreads well and produces a dense powder bed for the process. There are mainly 4 methods for manufacturing powders that are suitable for AM: gas atomization (GA) (Anderson, Figliola, and Morton 1991), water atomization (WA) (Seki et al. 1990; Persson, Eliasson, and Jönsson 2012), rotary atomization (RA) (Bourdeau 1983), and lastly the plasma atomization (PA) (Entezarian et al. 1996). The high surface area can result in surface oxides either from atmospheric interactions or the manufacturing process. Also, entrained gas in the powder may be present from manufacturing. It should come as no surprise to the reader that high quality powders yield better finished components, and that high-quality powders also tend to be expensive (Adriaan B. Spierings and Levy 2009; B. Liu et al. 2011; A. B. Spierings 2011; Sames et al. 2014). Therefore, quality and cost of the powders in question must be considered before down selection can occur.

All powder bed fusion builds suffer to some extent from defects and much effort had been directed at understanding and mitigating these defects. The main defects that affect the powder bed fusion process are residual gas porosity (Cunningham et al. 2017), defects in recoating (Foster et al. 2015), residual stress (Parry, Ashcroft, and Wildman 2016), balling (Khairallah et al. 2016), hatching or path defects (Foster et al. 2015), spatter (Criales et al. 2017; Barrett et al. 2019), keyholing (King et al. 2014), and lack of fusion (Tang, Pistorius, and Beuth 2017). As mentioned previously, entrained gas in the powder feedstock results in residual gas pores within the finalized component. Excessive energy input can also result in residual gas pores forming through material vaporization (Rao et al. 2016). Defects arising from the recoating system stem from two sources: (1) an issue resulting from the powder or (2) an issue resulting from the recoating mechanism. The first issue is related to

flowability and packing density of the powder feedstock. Low packing density, regarding recoating, can result in what is called a “short charge”, meaning that enough powder was not available to make a contiguous, even powder bed. A lack of flowability in the powder feedstock also creates an uneven powder layer in the form of streaks, runs, etc. The second issue is related to the individual machine manufacturer’s choice for the design of the recoater system. Such options as a roller versus fixed blade, roller rpm, blade material, etc., all can affect the powder bed from a consistency and stability viewpoint. Inconsistent powder bed thickness results in variation of the energy density being applied to it, which creates inhomogeneities and therefore defects. Also, the inconsistency, in the case of insufficient powder, means that there is a loss of build direction resolution due to incompleteness of the powder bed layer (Foster et al. 2015). The extreme thermal gradients intrinsic to powder bed fusion indicate that thermal management is of high priority. These thermal gradients induce stress which needs managed through component orientation and/or the addition of support material (Parry, Ashcroft, and Wildman 2016). Failure to do so results in warping and cracking as defects. From the standpoint of the build, residual stress defects represent the largest metric towards having a successful build (Alkhair 2016). Warping, cracking, and/or delamination of a component can result in part rejection from a metrology or material standpoint, but severe warping or delamination mid-build can also interfere with the recoating system and end in a failed build (Yasa et al. 2009; Kleszczynski et al. 2012).

Balling is an instability of the melt pool due to the traverse velocity of the heat source. Studies have shown that balling occurs when melt pool length to width ratio exceeds some value, typically reported as $\pi$ (Kruth et al. 2007). The notional anecdote is that the melt

pool stretches in response to increasing traverse velocity and that beyond a certain velocity the interplay between surface tension and solidification create balls of fused material larger than the parent feedstock. This means that the current layer being lased is not continuous causing defects in the component. This sets physical limits on the speed of the process. It can also result from certain hatching/path strategies where, for example, the required geometry is circular. A velocity differential will exist across the width of the beam source which can lead to a portion of the beam exceeding the conditions for balling and therefore must be under consideration. Hatching or path defects occur when the computer software algorithms that are used to plan the beam path for each layer leaves gaps in the geometry that are not lased (Foster et al. 2015). The algorithms used for path generation all have limitations, akin to how mesh generators have limitations in FEA. What results is "geometric porosity" which is a debit against mechanical properties. It is unfortunate in that most failures of hatching strategies occur between the outside contour of a component and the inside fill hatching which leaves subsurface defects that Romano reported lead to reduction in performance (Beretta and Romano 2017). Spatter has been investigated by a few authors (Y. Liu et al. 2015; Wang et al. 2017; Barrett et al. 2019). The literature suggests that the dominant mechanism for spatter ejecta formation in PBF is from entrainment of particles within an evaporative flow. It was previously thought that ejecta stem from instabilities within the melt pool caused laser induced recoil pressure. (Khairallah et al. 2016; Ly et al. 2017). The ejecta formed during the PBF process results in large particles (with respect to the powder feedstock), and if the ejecta resides on areas to be lased their larger size create inhomogeneities due to the fluctuation in energy density. PBF manufacturers have rudimentary solutions to mitigate this phenomenon, but spatter is

still under active investigation. Keyholing is a defect that happens when excessive energy is applied to the powder bed causing a pore to develop, usually in the previously fused layer (King et al. 2014; Cunningham et al. 2019). Typically, the melt pool is a balance of input energy and conduction of the material. This balance limits the amount of liquid phase developed and therefore controls the geometry of the melt pool. When excess energy is applied, the material begins evaporating and this vapor phase reduces the rate of heat transfer and the melt consequently becomes much deeper than intended. The keyhole defect occurs when the vapor cavity collapses (leaving a pore) due to the instabilities inherent to the system. Lastly, lack of fusion defects is the result of any type of insufficient powder bonding, whether it is inter- or intra-layer. Interlayer lack of fusion owing itself to poor selection of hatch/path overlap and is closely (indistinguishable) related to the previously described hatching defects, geometric porosity. Intralayer lack of fusion defects manifest from erroneous process parameters (mostly layer thickness, energy density) which do not allow for enough "tooth" between the current layer and the previously printed layer. The irregular morphology of lack of fusion defects lend themselves to significant debits against mechanical properties (Cunningham et al. 2017; Tang, Pistorius, and Beuth 2017).

Considering the defects which can occur during PBF, a host of in-situ sensing and monitoring has been proposed as the feedback control required to bring robustness to the process. Everton et al. reviews the fairly current state of those technologies (Everton et al. 2016). The goal of these in-situ monitoring techniques would be to inform the control system of possible flaws, where before the next layer commences could activate protocols to fix the defects before continuing the build. The current state of the research, however, is

that in-situ monitoring can for the most part identify defects, but is still wanting in the implementation of defect correction.

This project leverages powder bed fusion with the heat source being a laser beam. Laser powder bed fusion (LPBF) currently is situated as the preferred method of additive production of metal components (Wohlers et al. 2018). A host of research effort has been directed at the development of this particular technology. Various material systems have seen use in LPBF, but largely aerospace and medical grade alloys (e.g. Ti, Ni-Cr, and Al alloys) are commonplace. Sercombe et al. explored some of the inherent difficulties of working with aluminum alloys (Sercombe and Li 2016). Initial attempts to use aluminum alloys in LPBF were unsuccessful due to thermal cracking of typical wrought alloy chemistries, such as 6061 (Fulcher, Leigh, and Watt 2014). LPBF of aluminum poses several challenges to produce high-density components, because of the characteristics of the powder and chemistry. These include poor powder flowability, oxide layer formation on the powder surface, high reflectivity, high thermal conductivity. Success was found in the printing of aluminum alloys with casting grade, near eutectic composition, alloys.

One such alloy for LPBF is AlSi10Mg, which is compositionally similar to A360, and also precipitation hardening. The chemistry specification for this alloy system is shown in Fig. The Al-Si binary system has a eutectic at about 12% Si (by weight) and 577°C (Hansen, Anderko, and Salzberg 1958; Murray and McAlister 1984). Alloys containing between 11-13% Si are considered eutectic alloys and therefore alloys having more than 13% are hypereutectic and AlSi10Mg which contains 10% Si is a hypoeutectic alloy system. In general Al-Si alloys strengthening can be accomplished through the addition of Cu or Mg (ASM International 1990; Moustafa, Samuel, and Doty 2003). Both of these elements

increase mechanical properties through solid solution strengthening and by the formation of strengthening precipitates. The Al-Si alloys are also hardenable by rapid solidification where significantly high cooling rates are employed to refine the microstructure (Marola et al. 2018).

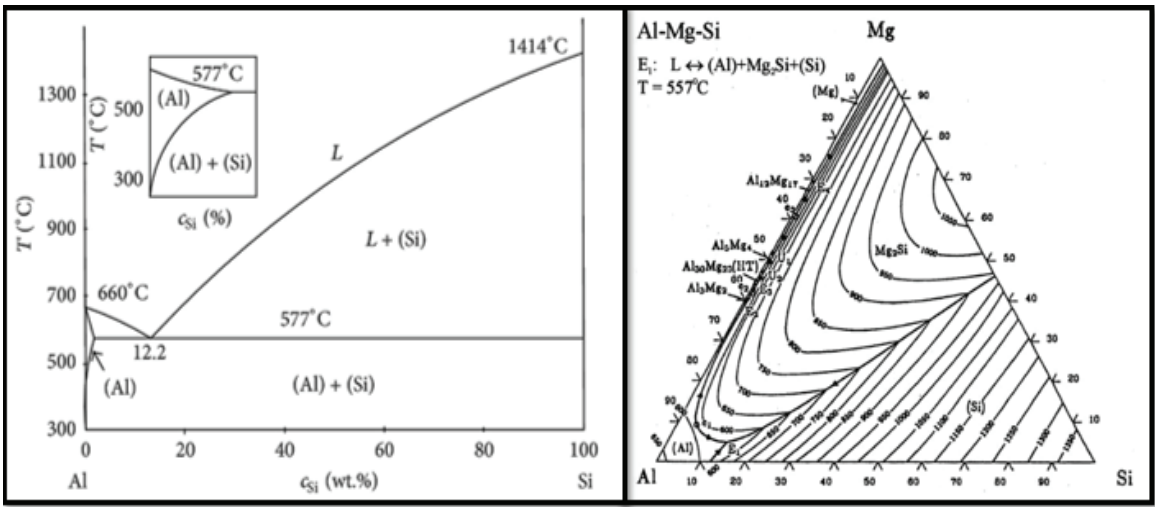


*Figure 37: (left) Binary Al-Si phase diagram (Hansen, Anderko, and Salzberg 1958); (right) Ternary Al-Si-Mg phase diagram (Braszczyński and Zyska 2000)*

The solidification conditions present in the laser powder bed fusion process create a novel microstructure in AlSi10Mg. While other forms of rapid solidification (melt spinning or copper mould casting) can mimic the cooling rates present in LPBF, authors in this field of research find that this system is unique (Marola et al. 2018). The as built microstructure (Figure 38) consists of a cellular network of aluminum cells surrounded by silicon. A few authors have shown that the unique condition processing conditions of laser powder bed fusion increases the solubility of silicon in aluminum to around 7% versus 1.65% in equilibrium conditions (A. I. Mertens and Delahaye 2017).

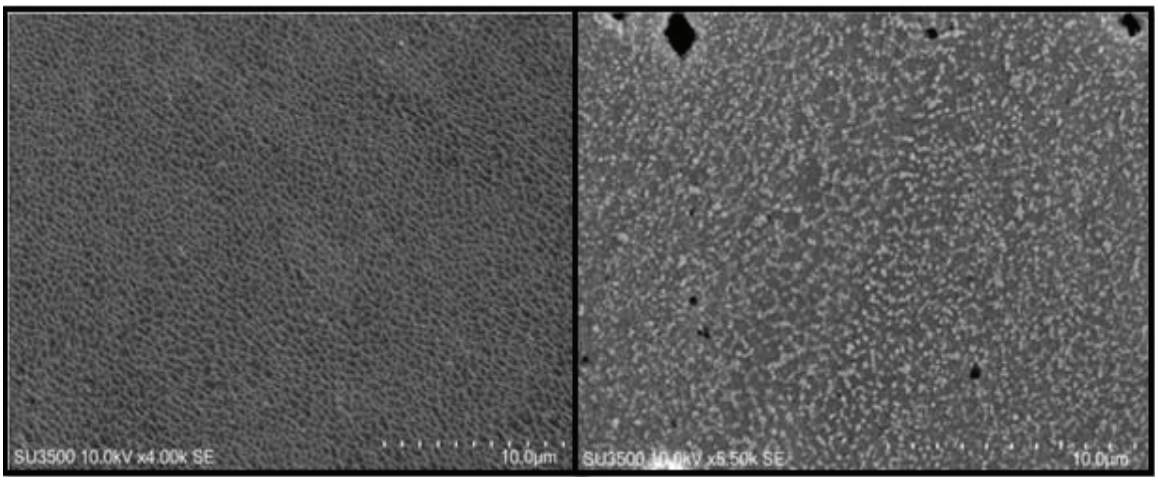


*Figure 38: (left) As built AlSi10Mg microstructure; (right) Stress relieved AlSi10Mg microstructure (Chou et al. 2017)*

Typically, mechanical strength in the alloy system is derived from $Mg_2Si$ formation, but Aboulkhair has reported that in as-built condition there exists little to no $Mg_2Si$ (Aboulkhair et al. 2016). Therefore, the high as built strength must be derived from other means. The general consensus is that while it does not fit the usual case, a Hall-Petch type relation applied to the cellular structure partly explains the increase in properties (Hadadzadeh et al. 2019). The notion is that small "grains" represented by the individual aluminum cells with surrounding silicon impeding grain boundary motion. When a Hall-Petch mechanism is coupled with solid solution strengthening, especially in light of the increased silicon solubility, constitutes the strengthening mechanisms present in as built AlSi10Mg.

A major concern in LPBF is the build-up of high internal stresses during fabrication. Residual stresses have been previously spoken about in the context of defects, but also play an important role post build. Removal of components from the build platform in a high stress state can result in undesirable end condition deformations. Understanding the quantitative stress state within these components post-build is difficult and an open

question within the field, but a common practice to resolve this issue consists of annealing in order to relieve the residual stresses. Annealing/Stress Relieving at *300°C* for *2* hours is the typical recommendation for AlSi10Mg (Diego Manfredi et al. 2013; Idan Rosenthal, Stern, and Frage 2014; Tang and Pistorius 2017). This procedure does produce some microstructural changes (fig. 37) where the cellular structure becomes muted, or mottled, by the initial Si spheroidization (Ma et al. 2014; Prashanth et al. 2014; Kimura and Nakamoto 2016; Fiocchi et al. 2017). Lower stress relieving temperatures have been tried in a few cases (A. Mertens et al. 2015; Shafaqat Siddique et al. 2015; Shafaqat Siddique, Imran, and Walther 2017). Temperatures between *240-250°C* resulted in increased ductility with little to no change in the microstructural morphology. It should be noted that with little change to the microstructure it is yet to be verified to what extent the residual stresses are reduced.

While much of the research into this alloy and process is concerned with as-built properties, the research presented here looks to develop an understanding, and leveraging, of the precipitation hardening ability of this alloy system. Precipitation hardening in the Al-Si-Mg system, traditionally, is accomplished through multi-step post-processing (fig. 38).

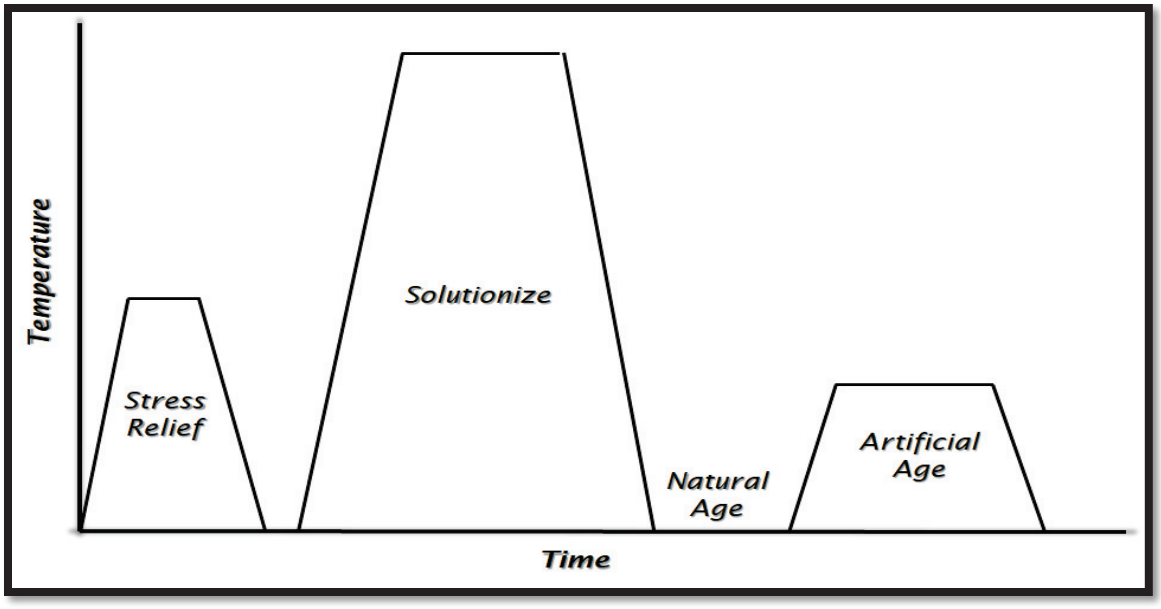


*Figure 39: Time-temperature diagram of the precipitation hardening sequence*

Previously mentioned and shown in (Figure 39) is the stress relief step where residual stresses are reduced to limit deformations upon removal from the build platform. Then the alloy is furnace solutionized which brings all the constituents into solid solution (ASM International 1990). Various research and standards exist on the proper temperature and time to solutionize (Moustafa, Samuel, and Doty 2003; "AMS2771F: Heat Treatment of Aluminum Alloy Castings - SAE International" n.d., "ASTM F3318 - 18 Standard for Additive Manufacturing – Finished Part Properties – Specification for AlSi10Mg with Powder Bed Fusion – Laser Beam" n.d.). Hansen reports *500°C* is the minimum required for diffusion of magnesium and silicon in the aluminum matrix and *577°C* as the maximum before liquidus is achieved (Hansen, Anderko, and Salzberg 1958). At the end of the solutionization a quench is performed to lock into solid solution as much as is possible. Quench rate in the Al-Si systems has been researched (with regards to traditional alloy manufacture) and generally is chosen to maximize strength while minimizing deformation

(T. Croucher 1982). It has been shown that high quench rates result in higher achieved strengths, but this comes as the cost of increased propensity for deformation (Tom Croucher 2009). While some general guidelines are applicable, this quench induced deformation is geometry specific and requires attention on a case by case basis.

After quenching, a period of natural aging occurs. Aging, or precipitation, in many aluminum systems occurs even at room temperature. Some alloys are even known to natural age extremely quickly; however, AlSi10Mg has a relatively flat natural aging curve. Length of the natural age is designated to balance between the realities of manufacturing time constraints, (i.e. components cannot reach the artificial age furnace before time *X*), and end product mechanical properties. Research shows that in this alloy system at least 1-hour of natural aging in order to develop some increase in hardness (Shivkumar, Keller, and Apelian 1990; Möller, Govender, and Stumpf 2007). This minimum is largely driven by magnesium content. After that minimum, many studies have shown which then becomes the standard for the appropriate time to naturally age.

Artificial aging is the last step performed in the precipitation hardening process. The artificial aging process is where the alloy system is held in a furnace at elevated temperature to produce strengthening precipitates. For AlSi10Mg this means two competing and contradictory mechanisms are active during artificial aging: (1) formation and coarsening of the strengthening $Mg_2Si$ phase and (2) the rejection, coalescence, and ripening of excess silicon out of the aluminum matrix. The precipitation sequence has been studied in the Al-Si alloys with Guineir-Preston zones yielding the nucleation sites $Mg_2Si$ formation and coarsening (Edwards et al. 1998; Murayama et al. 1998; Murayama and Hono 1999). The aging kinetics are driven by temperature and time. Three temperature regimes exist which

have subsequent effect on aging (Myhr, Grong, and Andersen 2001; Rometsch and Schaffer 2002). At *120°C* and below, the energy is not sufficient to drive kinetics effectively, and even if reaching peak properties is possible, it usually takes or even weeks to achieve. Conversely, temperatures above *180-190°C* drive kinetics so rapidly that only a few hours, roughly 3, are required to reach peak properties. While this may be desirable for time conscious operations, the quickened kinetics leave little room for error with regards to timing as the aging curves are very peaked. The goldilocks zone, as it were, is between *120-180°C* with *160°C* being commonly specified for peak aging ("AMS2771F: Heat Treatment of Aluminum Alloy Castings - SAE International" n.d.). These temperatures yield peak properties in sub-day timescales and are robust to same errors in timing.

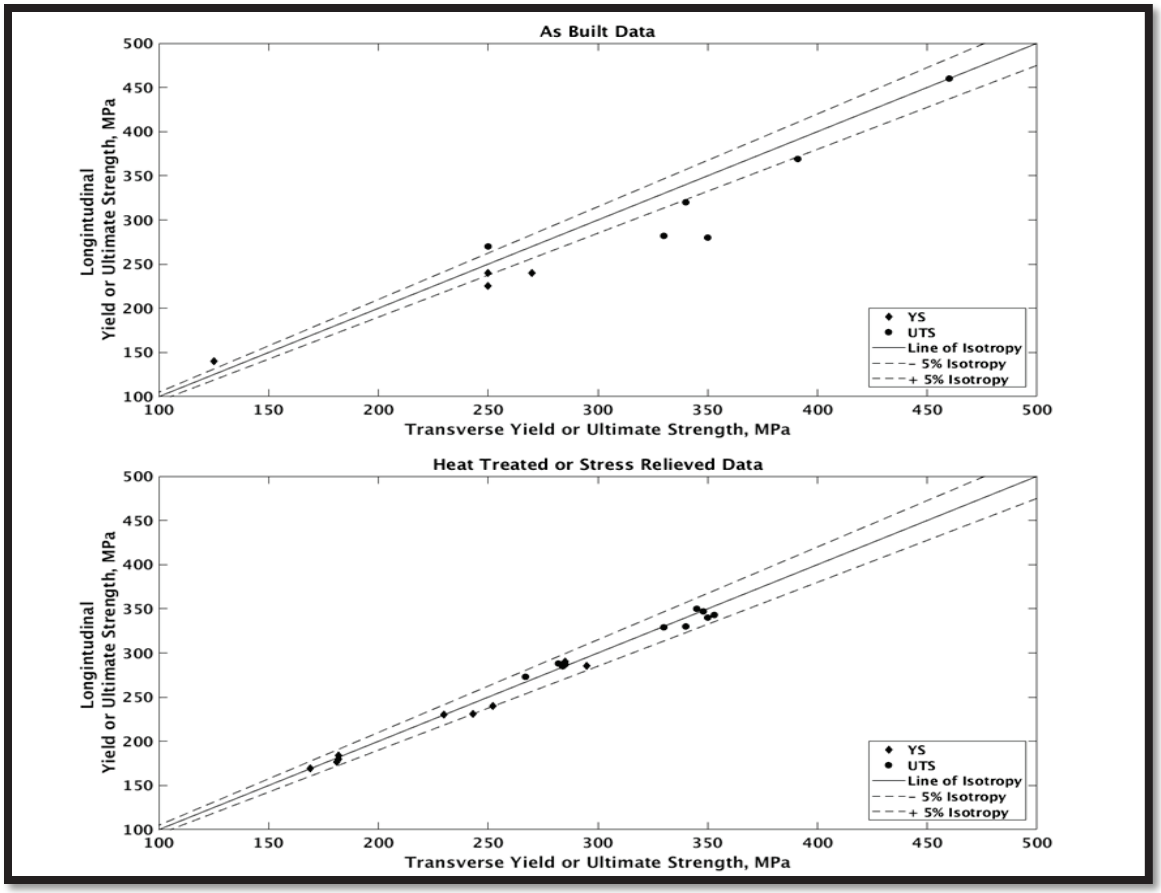


*Figure 40: Transverse versus longitudinal mechanical properties as reported in the literature*

Researchers investigating AlSi10Mg have reported mechanical properties of both as built and heat treated LPBF samples (Buchbinder and Meiners 2010; "EOS Metal Materials for Additive Manufacturing" n.d.; Kempen et al. 2012; Brandl et al. 2012; Diego Manfredi et al. 2013; D. Manfredi, Ambrosio, and Calignano, n.d.; Idan Rosenthal, Stern, and Frage 2014; Kempen et al. 2015; Maskery et al. 2015; Read et al. 2015; S. Siddique, Wycisk, and Frieling 2015; Tang and Pistorius 2017). Figure 40 plots the available literature data. On those plots are lines designating isotropy and deviance from isotropy. In general, as built samples exhibit transverse isotropy while post processed data significantly less. There was also an increase in ductility of the post processed data.

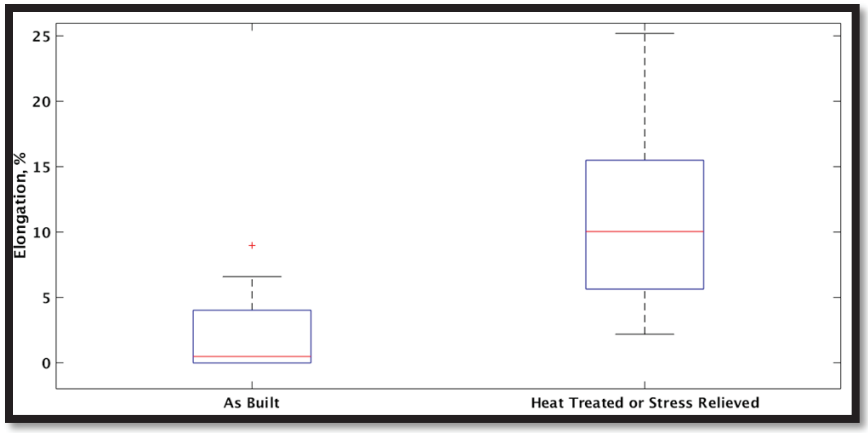


*Figure 41: Whisker plot of elongation % reported in the literature between as built and heat treated AlSi10Mg*

Heat treatments can develop the microstructure to produce tunable mechanical properties but have little effect against the aforementioned defects inherent to the LPBF process. In powder metallurgy, hot isostatic pressing (HIP) has been used for some time to heal internal flaws and consolidate powder metallurgy parts (Lewandowski and Seifi 2016). HIP is a post-processing treatment that combines elevated temperatures with the application of pressure. In LPBF of AlSi10Mg, Brandl, Uzan, Tradowsky et al. and others have reported an improvement in ductility and fatigue after HIP (Brandl et al. 2012; Maskery et al. 2015; Rao et al. 2016; Beretta and Romano 2017; Romano et al. 2018; Tradowsky et al. 2016; Uzan et al. 2017). However, most of the research using HIP is only concerned with fatigue properties and not as a part of a complete post-processing schedule.

Trevisan et al. has explicitly stated that AM AlSi10Mg does not respond to post-processing like traditionally cast version and a needed area of research is in the definition of a new heat treatment strategy for this system (Trevisan et al. 2017). With this project, the plan is to fabricate a significant number of bell cranks and test coupons on two different

manufacturers of laser powder bed fusion systems (EOS and 3D Systems). Repeatability, process robustness, and the ability to specify requirements that are not machine specific are three overarching aspects to this research. In terms of post-processing, the aim of this research is to plug holes in the current body of literature by creating a continuous thread from build platform to finished component. The information provided generating an initial rubric in the post-processing of AlSi10Mg.

## *Methods and Materials*

This section will give an overview of the experimental methods used in this investigation. Before any experiments can commence, thoughtful design of these experiments is required. Once an experimental design is chosen, implementation of the experiment itself and the various testing methods used to acquire results may commence. Examples of these testing methods include hardness testing, optical microscopy, and mechanical testing.

## *Experimental Methodology*

This research sits positioned within a larger project. A portion of this project is to examine and create an additive manufacturing process specification in which a powder and process are combined to create a part without reference to a particular LPBF machine. LPBF as an industry currently has an issue and that issue is that the final product being produced are too machine specific. Manufacturers of machines seeking market competitiveness and or dominance has led to proprietary powders and machine features that in some cases can drastically alter material properties of the finished part. It is the view of these authors that additive manufacturing should take reference to its subtractive counterpart and even though

there are a multitude of subtractive machine tool suppliers all with special features the parts produced still consistently meet the guidelines set forth by the blueprint. With this said, the samples of this research were produced using three machines and EOS M-290 and EOS M-280 (Krailling, GER) and a 3DSystems ProX320 (Rock Hill, South Carolina, USA). The samples were marked in order to trace back any specific build flaws but in terms of the research presented here the samples are commingled between all machines.

*Table 8: Laser powder bed fusion process parameters*

| Mode | Power | Traverse Speed | Hatch Spacing | P/V | Timing | Location |
|---|---|---|---|---|---|---|
| - | W | mm/s | um | J/mm | - | um |
| Infill | 370 | 1400 | 110 | .26 | - | - |
| Contour 1 | 300 | 1450 | - | .21 | Pre | -60 |
| Contour 2 | 300 | 1450 | - | .21 | Post | -120 |
| Up skin | 250 | 1200 | 100 | .21 | - | - |
| Down skin | 75 | 1600 | 100 | .05 | - | - |

A detailed study was performed by Penn State into selecting a powder supplier. Many tests were performed in order to verify powder chemistry morphology and flowability, which are all significance features for additively produce powder parts. The final supplier chosen for this project was LPW, a subsidiary of Carpenter Technology Corporation and now called Carpenter Additive and has a powder size distribution between *15* and *40* microns and the powder chemistry is shown in the table below.

*Table 9: AlSi10Mg chemical composition*

| Al | Si | Mg | Fe | Cu | Mn | Ni, Zn | Sn |
|---|---|---|---|---|---|---|---|
| bal | 9-10 | .4-.6 | 2 | .6 | .35 max | .5 max | .15 max |

The majority of samples for testing were metallographic cylinders. These cylinders are *25* mm (roughly *1"*) in diameter and are of varying height. These metallographic cylinders are dual purpose. First and foremost, they are for this post processing investigation, but secondly within a given build these cylinders are used to balance layer-to-layer time which is a variable under investigation by other collaborators on this project. Layer-to-layer time is proxy for the amount of heat input per layer and balancing this layer-to-layer time minimizes the change in temperature between any two layers. These cylinders are further sectioned into disks of *19* mm in length before experimentation. These samples were randomized according to an ordering generated in MATLAB (Mathworks, USA). Randomization allows for results homogenization between the location where the sample was built on the platform, height of the sample within a given cylinder, and across machines. This is designed to meet the overall goal of the project of having cross-platform production ability.

The second type of sample used within this investigation plate type samples that can be later turned into tensile bars for uniaxial tensile testing. These plate samples are used multiple places throughout the project at large and therefore are a scarce commodity for this investigation and are used sparingly.

## Heat Treatment

The heat treatments on the metallography disks were performed at Youngstown State in a research style set up and by Oerlikon in an industrial type setting. This included an electric muffle furnace (Thermolyne, USA) capable of achieving the required temperatures for solutionizing and artificial aging and met the standard for temperature stability and deviation ("AMS2771F: Heat Treatment of Aluminum Alloy Castings - SAE International" n.d.). The quenchant mediums were contained in clean, quart canisters (Granger, USA). A quick energy balance calculation was performed to know the relative volume of quenchant per sample that would produce less than a 20 degree increase in the quenchant temperature as per the AMS 2771 standard which was being followed.

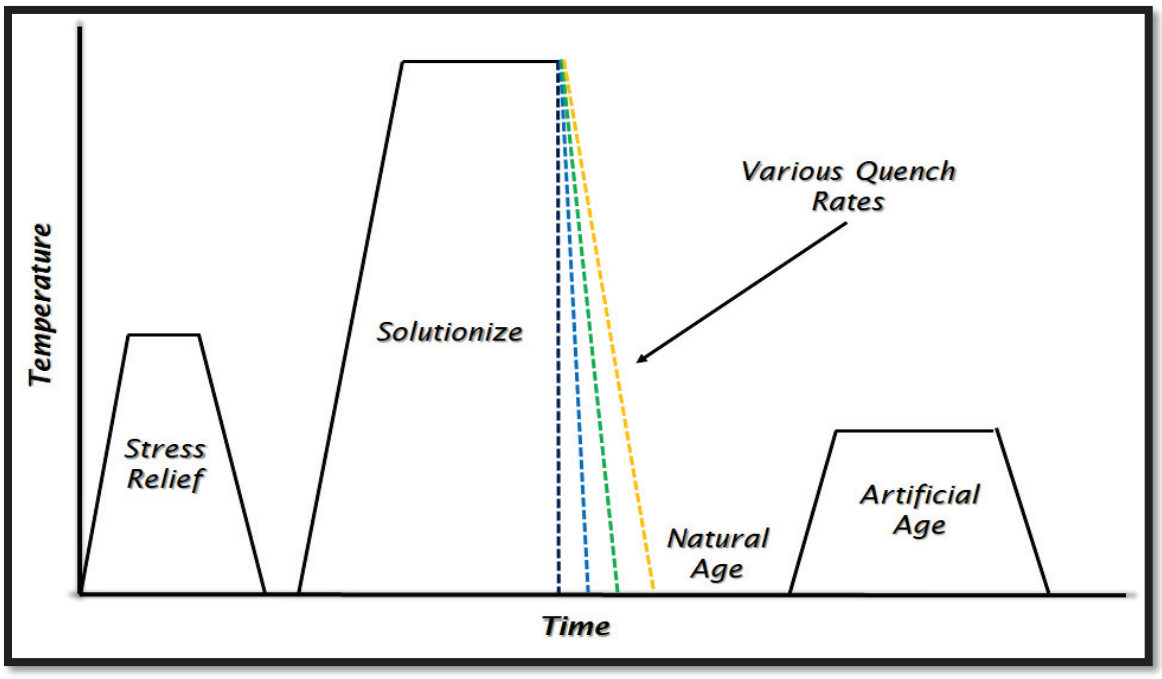


*Figure 42: Time-temperature diagram of the precipitation hardening sequence including various quench rates*

ASTM F3318 has provisions for two different stress relief recipes: (1) *285°C* for *2* hours or (2) *190°C* for *2* hours both followed by an air cool. All printed samples within the scope

of this project received a stress relief of *285°C* for *2* hours (sometimes referred to as *SR1*) before being removed the build substrate. Again, borrowed from the standard, the solution heat treatment of *530°C* for *6* hours was applied to all samples that would be precipitation hardened.


*Figure 43: Youngstown State's heat treatment setup and laboratory equipment used in this investigation*

## Quench Rate

Quench rate in the Al-Si systems has been researched (with regards to traditional alloy manufacture) and generally is chosen to maximize strength while minimizing deformation (T. Croucher 1982). Quenchants were chosen to demonstrate a range of cooling rates. The quenchants for this investigation are (from low to high rate): forced air cool (by fan), near boiling water (*95-100°C*), *100%* ethylene glycol, and room temperature (*20-25°C*) water.

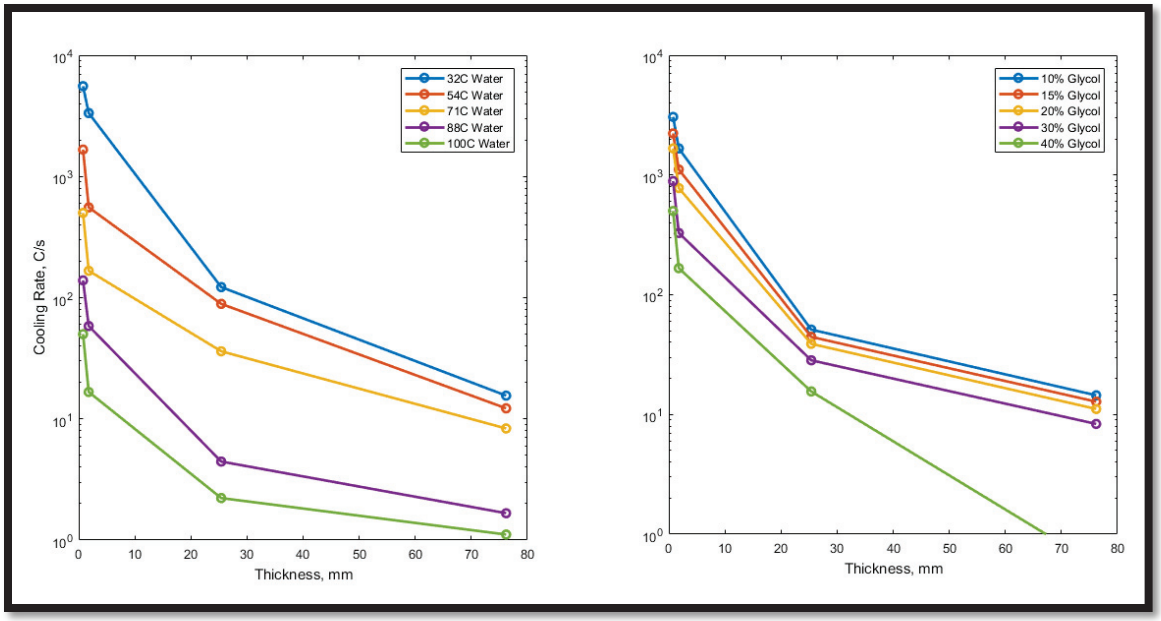


*Figure 44: Quench rates of water (at various temperatures) and ethylene glycol (at various concentrations). Data from Croucher (T. Croucher 1982)*

## Natural Aging

ASTM F3318 defers to AMS 2771 for specifying the duration of natural aging post quench at 16 hours ("AMS2771F: Heat Treatment of Aluminum Alloy Castings - SAE International" n.d.). A project collaborator, Oerlikon, who was also responsible for some of the heat treatment specifies a natural age between one and four hours. All the natural aging for these investigations occurred at one hour or *16* hours.

## Artificial Aging

The ASM handbook provides a list of processing configurations available for precipitation hardening aluminum alloys (ASM International 1990). The most common treatment is that of a *T6* treatment. *T6* is considered to be peak hardened and has been designated as artificial aging at *160°C* for 6 hours. The only other common artificial aging treatment is *T7*. *T7*

condition is considered overaged and is specified as artificial aging at *205°C* for *3-6* hours ("AMS2771F: Heat Treatment of Aluminum Alloy Castings - SAE International" n.d.). Since there is a range given for the *T7* treatment, *4.5* hours was chosen for the length of artificial aging.

The standard, for which the tested conditions in this investigation are based, is predicated on developing the prerequisite mechanical properties and microstructure for cast alloys and the novel microstructure of AlSi10Mg therefore requires an understanding of the aging kinetics present with this alloy and process system. An aging study was performed at the two artificial aging temperatures of *160°C* and *205°C*. The aging study examined the kinetics of AlSi10Mg at *160°C* for 10 hours in two hour increments except around the six hour mark was subdivided into one hour increments. For the *205°C* study, samples were taken every *1.5* hours up to *7.5* hours. The structure of this study in captured in Table 10. Samples for the aging study were all solutionized at *530°C* for *6* hours and quenched with room temperature water. The samples were naturally aged for *16* hours before artificial aging at the two prescribed temperatures. The zero hour samples (Table 10) were refrigerated until the time of testing.

*Table 10: Artificial aging sample times based on aging temperature*

| 160C | 205C |
|---|---|
| 0 | 0 |
| 2 | 1.5 |
| 4 | 3 |
| 5 | 4.5 |
| 6 | 6 |
| 7 | 7.5 |
| 8 | |
| 10 | |

## *HIP*

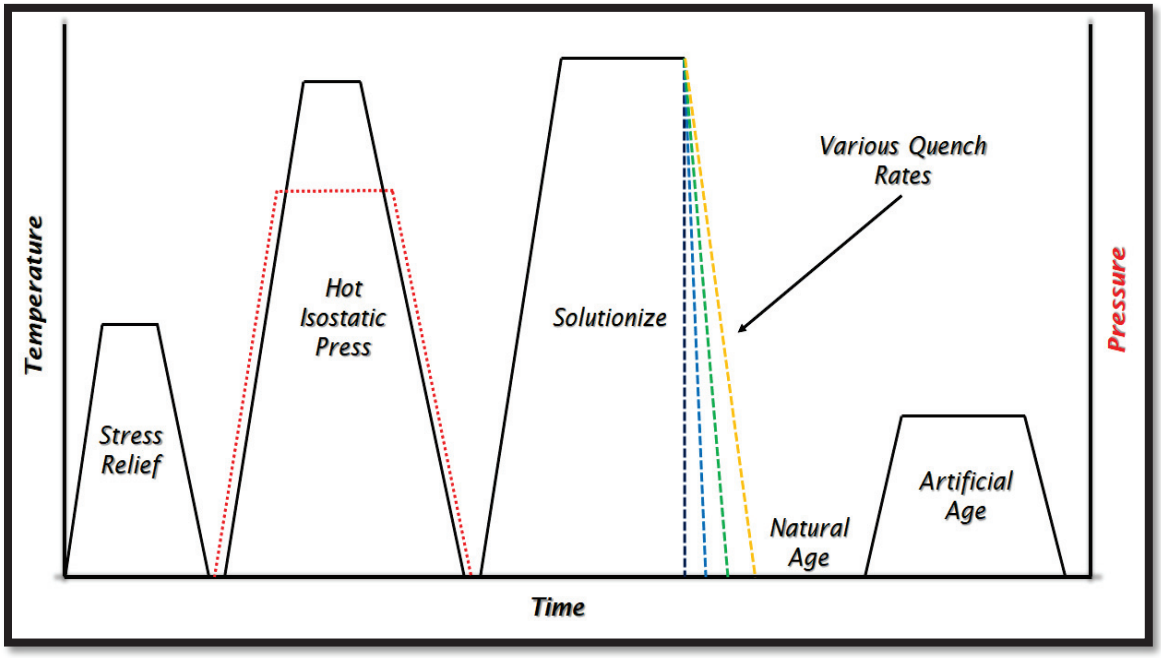


*Figure 45: Time-temperature-pressure diagram of the precipitation hardening sequence including hot isostatic pressing*

Hot isostatic pressing (HIPing) is a common treatment in an additively manufactured parts as it has the ability to heal gas porosity and some other artifacts of the manufacturing process. Hot Isostatic Pressing (HIPing) is the last experimental variable in this investigation. ASTM F3318 specifies *510-520°C* at *100* MPa for 3hrs and a furnace cool until *93°C* at which time the HIP vessel can be opened, and samples exposed to atmosphere. Oerlikon was responsible for the HIPing of test samples. Having HIP as an experimental variable allows for a quantitative comparison of the performance advantage of hot isostatic pressing versus as built but heat-treated condition. The intent is to have a rubric for a situation where the properties of non-HIP samples are adequate for the finished component where it would save the cost and complexity of the extra step of HIP.

## *Nomenclature*

An important aspect to maintaining clarity with the various different conditions of the samples is a consistent nomenclature. Below is Table 11 that encapsulates and demonstrates the nomenclature that will be used to describe post processing hereon.

*Table 11: Post-processing configuration nomenclature*

| | (①/②/③/④/⑤/⑥) | | | | | |
|---|---|---|---|---|---|---|
| | ① | ② | ③ | ④ | ⑤ | ⑥ |
| **Process** | **Stress Relief** | **Hot Isostatic Press** | **Solution Heat Treat** | **Quench** | **Natural Age** | **Artificial Age** |
| **Structure** | <Temp><Time> | <X> | <Temp><Time> | <X> | <Time> | <Temp><Time> |
| **Options/Examples** | SR1 = 285C2H | HIP = H | 530C6H | Forced Air = FAQ | 1H | 160C6H |
| | SR2 = 190C2H | Non-HIP = NH | | Room Temp Water = RTWQ | 16H | 205C4.5H |
| | | | | Hot Water = HWQ | | |
| | | | | Clycol = CQ | | |

As an example, *(285C2H/NH/530C6H/FAQ/16H/160C6H)* is the specification for a sample that was *SR1* stress relieved and not HIPed, received traditional solution heat treat of *530°C* for *6* hours, forced air quenched, and aged naturally for *16* hours before receiving an artificial age at *160°C* for *6* hours. At times various portions may be omitted, such as not specifying the stress relief since all samples in this investigation receive the same stress relief process.

## *Post Processing Characterization*

### Specimen Preparation

Preparation of the metallographic cylinder samples consisted of initial planing of both sides with *220* grit sandpaper to ensure the samples were flat and squared to the cylindrical axis. One of these sides in the planed condition would be used for hardness testing, while the other side would receive polish and etch for microscopy. Consultation of Buehler's technical references for polishing of A356 aluminum was used as a base formulation for the preparation of these samples for microscopy (Asensio-Lozano and Voort, n.d.). The base recipe was followed, but changes were necessary to achieve good results (Table 12). Namely, adjustment of pressures and times used for the polishing steps (Planopol, DEN) and ultrasonication (Branson, USA) in between each step to remove residue polishing compound from pores in the surface. Without ultrasonication, these pores would release larger sized polishing compound from the previous steps that would mar the surface.

*Table 12: AlSi10Mg specimen preparation recipe*

| Step | Surface/Abrasive | RPM | Load (Setting # on Plane-o-Pol) | Time |
|---|---|---|---|---|
| 1 | 240-grit SiC Paper | 300 | 3 | Until Plane |
| 2 | 320-grit Sic Paper | 150 | 3 | Until Plane |
| 3 | 9um Suspension on Ultra-Pad Cloth | 150 | 5 | 10 min. |
| 4 | 3um Suspension on Trident Cloth | 150 | 3 | 7 min. |
| 5 | .05 um Silica Suspension on Chemomet Cloth | 150 | 2 | 5 min. |

After polishing, the samples were etched to reveal the microstructure. There are some common aluminum etches used for aluminum such as: Keller's etch (*2* mL HF, *3* mL HCl, *5* mL $HNO_3$, *190* mL $H_20$), hydrofluoric etch (*1* mL HF, *200* mL $H_20$) or Weck's reagent

(*4* g $KMnO_4$, *1* g of NaOH, *100* mL $H_2O$) (Asensio-Lozano and Voort, n.d.; Mohammadtaheri 2012; Gao, Harada, and Kumai 2015). Two etchants were tried with varying success on the samples. The hydrofluoric etch reveals the constituents of the microstructure after *25*s immersion, but even with extended immersion does not reveal grain structure. Weck's reagent is a colorizing etch which after *12*s immersion reveals both constituents and grain boundaries in samples. However, it is rather easy to over-etch and stain the samples. Microscopy will be shown later of samples etched in either manner.

The tensile bar samples were machined in accordance with ASTM E8 sub size specimens shown in Table 13.

*Table 13: ASTM E8 tensile bar specimen dimensions (I. Astm 2016)*

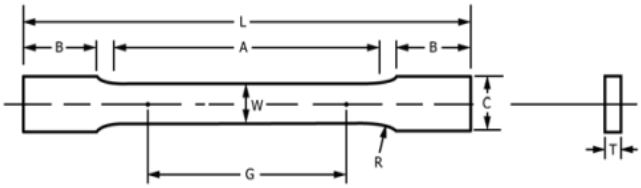


| | Dimensions | | |
|---|---|---|---|
| | Standard Specimens | | Subsize Specimen |
| | Plate-Type, 40 mm [1.500 in.] Wide | Sheet-Type, 12.5 mm [0.500 in.] Wide | 6 mm [0.250 in.] Wide |
| | mm [in.] | mm [in.] | mm [in.] |
| *G*—Gauge length (Note 1 and Note 2) | 200.0 ± 0.2 [8.00 ± 0.01] | 50.0 ± 0.1 [2.000 ± 0.005] | 25.0 ± 0.1 [1.000 ± 0.003] |
| *W*—Width (Note 3 and Note 4) | 40.0 ± 2.0 [1.500 ± 0.125, -0.250] | 12.5 ± 0.2 [0.500 ± 0.010] | 6.0 ± 0.1 [0.250 ± 0.005] |
| *T*—Thickness (Note 5) | | thickness of material | |
| *R*—Radius of fillet, min (Note 6) | 25 [1] | 12.5 [0.500] | 6 [0.250] |
| *L*—Overall length, min (Note 2, Note 7, and Note 8) | 450 [18] | 200 [8] | 100 [4] |
| *A*—Length of reduced parallel section, min | 225 [9] | 57 [2.25] | 32 [1.25] |
| *B*—Length of grip section, min (Note 9) | 75 [3] | 50 [2] | 30 [1.25] |
| *C*—Width of grip section, approximate (Note 4 and Note 9) | 50 [2] | 20 [0.750] | 10 [0.375] |

## Microscopy

### Optical Microscopy

Optical microscopy (OM) was performed on all the metallography disks. Of primary importance to be investigated were the characterization of any defects present and the morphology of the microstructure. The optical microscopy was performed on a Keyence microscope (VHX 6000, Keyence, USA). This microscope has 20x-2000x magnification, as well as polarization, image stabilization, and a variety of lighting options. Micrographs taken during optical microscopy would be further processed with image analysis to quantify apparent features of the different post processing conditions. Optical microscopy was also used as a screening tool for SEM analysis.

### SEM

With macro and meso scale features observed during optical microscopy, Secondary Electron Microscopy (SEM) is a great tool to resolve micro features present in the samples. Optical Microscopy was used as a screening tool for SEM analysis. Any intriguing morphologies or unclear features observed in OM would be marked for investigation with SEM. Youngstown State has a substantial investment and facilities for electron microscopy and a JOEL Multi-beam (need model, Japan) was used for SEM imaging.

### Image Analysis

Image analysis of all micrographs was handled with Fiji (Schindelin et al. 2012). Fiji is an extension of the open source software ImageJ which includes a host of plugins applicable to metallography. In essence, Fiji is a more user-friendly version of ImageJ with popular add-ons preloaded.

The software is also relatively straightforward in the calculation of gas porosity defects and or silicon particle size. Other researchers in the project are also determining the percentage of gas porosity within the additively produced parts. Optical microscopy was used as a check against CAT scan and/or X-ray analysis of gas porosity. Additive manufacturing of metals specifically suffers from gas porosity in the finished parts. Gas porosity leads to a reduction of modulus and affects the fatigue behavior of the material. Both of these mechanical properties are of interest, first with the modulus controlling deflections, which, depending on the final application required, can necessitate a deflection driven design. Secondly, aluminum alloys also have a non-infinite fatigue life, and any gas porosity induced further reduces the already limited service life of a given component.

Observation of the silicon particle size should correlate, although indirectly, to various heat treatments through growth kinetics and mechanical properties through Orowan looping (Orowan 1948). Orowan looping, or strengthening, is the bowing of dislocations as they precess around relatively hard (in comparison to the matrix) precipitates. This lengthening of the dislocations is an energy storage mechanism resulting in increased macroscale strength. The bowing also reduces the dislocation velocity. Orowan looping is dependent upon particle size and spacing, and typically both occur on nanometer length scales. Direct observation requires transmission electron microscopy (TEM) to resolve such length scales. Therefore, the optical and secondary electron microscopy is used as an indirect indicator of the primary strengthening mechanism present in Al-Si-Mg alloy systems. As mechanical properties manifest from the microstructure and a quantitative understanding of the morphologies present due to various heat treatments and or quenching treatments will generally, time permitting, be an advantageous avenue of study. Therefore,

understanding this particle size to strength and or hardness relation was deemed worthy of investigation.

## Chemical Analysis

Analysis of elemental and compound composition was performed on the various post processing conditions already discussed. This analysis was performed using two techniques: energy dispersive spectroscopy (EDS) and x-ray diffraction (XRD). An EDS detector (EDAX, USA) is integrated into the JOEL SEM and allows elemental probing of interesting features while SEM imaging. While single point probing with EDS is simple, quick, and effective also available are line and area scans. Collecting data from a line or area scan can be time intensive but can reveal the spatial organization of elements within the microstructure.

As a compliment to EDS, XRD can reveal elemental and compound composition and with further analysis relative phase ratios within the sample. A Bruker D8 (Germany) machine was used for XRD analyses in conjunction with their software (Diffrac.Suite). Machine settings and assistance with analysis was provided by Materials Research Lab (MRL, Struthers, Ohio). XRD analysis of unknown samples requires access to Crystallography Index File (CIF) database for the reference spectra of elements and compounds. Of interest in this investigation are aluminum, silicon, $Mg_2Si$, $Al_XFeSi$, $SiO_2$, and $AlO/Al_2O_3$ which were identified through compositional information provided from the powder manufacturer and from the literature. Combining these CIF's into a theoretical spectrum is the starting point for the refinement using TOPAS. TOPAS, which is the modern version of Rietveld refinement, is a least-squares regression technique applied to the theoretical

spectrum to match the experimentally received spectrum. The weights calculated during the refinement are very telling of makeup of the tested sample. While the refinement parameters can reveal much, relative phase percentage and aluminum lattice spacing are the primary results sought in this investigation. The samples have been post-processed in various ways and monitoring compositional changes can be illustrative.

## Mechanical Properties Testing

### Hardness Testing

The heat-treated metallography disks, after an initial plane surface was produced, were subjected to hardness testing. Training and some testing took place at MRL in accordance to ASTM E18. The testing at MRL was performed on a Wilson analog hardness tester (Wilson, USA) and testing at Youngstown State was also performed on a Wilson hardness tester only a digital version. The samples exhibited a range of hardness's and therefore a combination of Rockwell hardness B scale and Rockwell hardness F scale were used. The machines were calibrated for accuracy using the correct calibration blocks for the Rockwell scales that were used. Both Rockwell B&F scales use a *1/16"* diameter steel sphere indenter. The difference between the two scales is the load applied to the sample. Rockwell B scale uses *100*-kilogram force while Rockwell F scale uses *60*-kilogram force.

Part of the analysis also included conversion from Rockwell B&F scales into the single Vickers hardness scale. Conversion charts were found, the data was plotted against each other and a curve fit was performed. The graph below (Figure 46) shows a general trend towards an exponential type curve fit, but a second order exponential was required to reduce the residuals to a level to confidently extrapolate data from ($R^2>.95$).

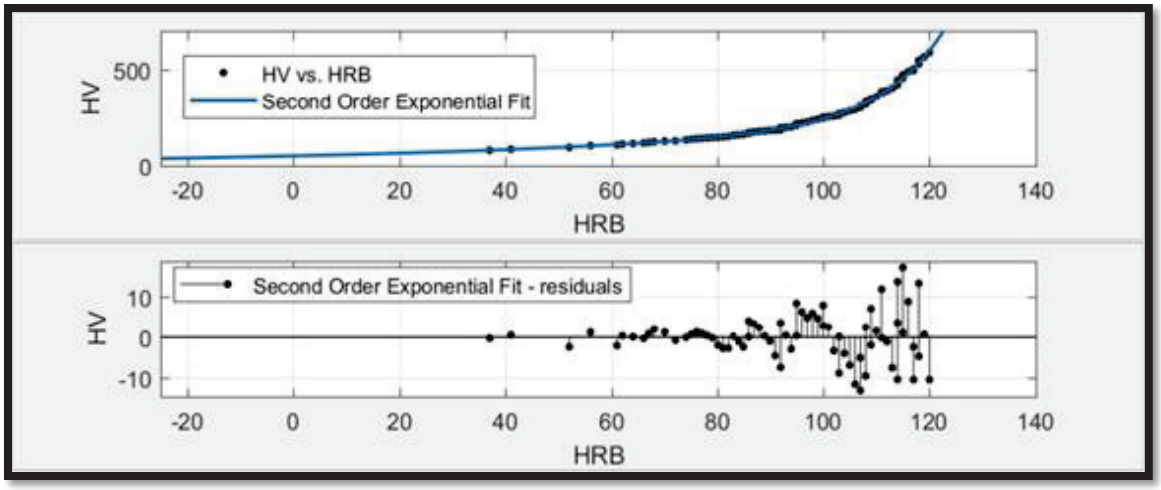


*Figure 46: Rockwell B to Vickers Hardness Conversion*

Five data points were taken from each of the metallography disks so that statistics could be performed on all the data with the mean and standard deviation for each configuration calculated. Five measurements were taken to lower the standard deviation among configurations to allow statistically significant conclusions to be drawn.

### Uniaxial Tensile Testing

Mechanical testing in the form of tensile testing was performed on select heat treatments. Because of the previously mentioned scarcity of plate type samples available for uniaxial tensile testing, only a subset of six post processing conditions were tested. The mechanical testing was performed on an Instron universal testing machine (5500R, Instron, USA) with *150*KN load cell and extensometer. The test parameters were aligned with the ASTM E8 standard. A closed-loop, strain-controlled test is not currently possible with this machine, so a fixed strain rate of one mm/min was used.

The uniaxial tensile testing would provide not only hard data on the actual mechanical properties of interest, but also would form the basis in order to cross-compare with the other heat treatments via their hardness tests. The relations from Cahoon and Tabor provide the basis for these calculations to convert Vickers hardness into ultimate tensile strength and yield strength respectively (TABOR and D 1951; Cahoon, Broughton, and Kutzak 1971; Cahoon 1972; Tabor 2000).

$$\sigma_{ys} = g\left(\frac{H}{3}\right)\left(\frac{1}{10}\right)^{n} \qquad \textit{(Equation II)}$$

$$\sigma_{uts} = g\left(\frac{H}{2.9}\right)\left(\frac{n}{.217}\right)^{n} \qquad \textit{(Equation III)}$$

Both of these conversion equations make use of a hardening exponent. Whether it is *n*, the strain hardening exponent, or *m-2*, the Meyer's hardness coefficient, these exponent values in general require experimental data. Reported in the literature are strain hardening exponents for aluminum alloys between *.05-.3* (Cahoon 1972; Rometsch and Schaffer 2002), with more recent studies specifically in AlSi10Mg placing that value around *.18-.25* (I. Rosenthal, Stern, and Frage 2017; Chen et al. 2017). Therefore, with the data acquired from uniaxial tensile testing a strain hardening exponent and/or Meyer's hardening coefficient could be derived for the conversion equations.

## *Results and Discussion*

The results gathered from the previously described experiments will now be presented and discussed in the following section. There is a structure as to how the results are presented. The results section is divided into individual post processing conditions. Each of those divisions will present the results obtained through microscopy, chemical analysis, and, lastly, mechanical testing. Annotation of the results and their context will be saved for the discussion.

## *Stress Relief Only (SR1 or 285C2H)*

This section contains the results of the stress relief only samples. Figure 47 shows SEM micrographs at two different magnifications with the aluminum being the dark phase and silicon being the light phase. The contrast is enhanced in these images. That is followed by Table 14 which summarizes the quantitative values of the porosity, mean, mode, and standard deviation on the cell size present in those micrographs. Figure 48 are optical micrographs and shows the archetypal structures present in stress relief only samples with the laser artifacts of the melt pools shown in both a transverse and longitudinal plane. Next are the results from the XRD analysis which are shown in Figure 49 with the peaks indicated. Lastly are the quantitative values for the mechanical properties. Hardness, yield strength, ultimate tensile strength, elongation, and the strain hardening exponent shown in Table 15.

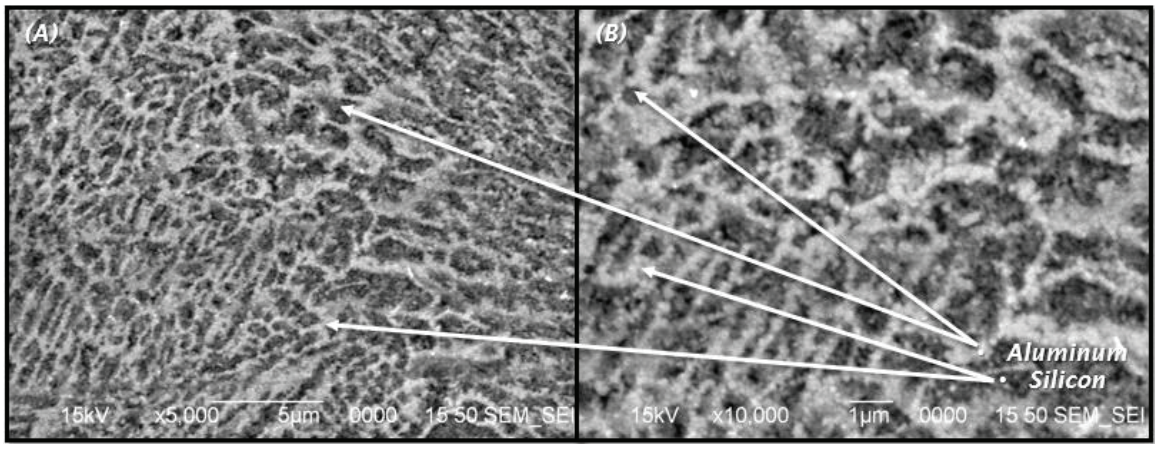


*Figure 47: Microstructure of SR1 samples at two different magnifications with aluminum (dark phase) and silicon (light phase) highlighted (contrast enhanced)*

*Table 14: Cell size and porosity results for (285C2H)*

| Porosity, % | Cell Size Info | | |
|---|---|---|---|
| | Mean, um | Mode, um | SD, um |
| 1.29 | .38 | .3 | .38 |

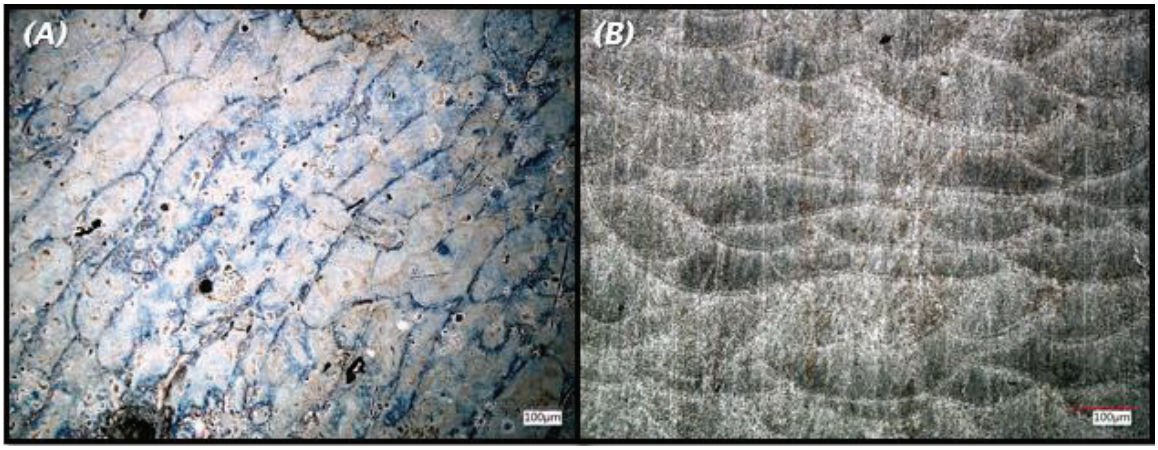


*Figure 48: Low magnification OM of archetypal (A) transverse plane laser hatching and (B) longitudinal plane fish scale structure*

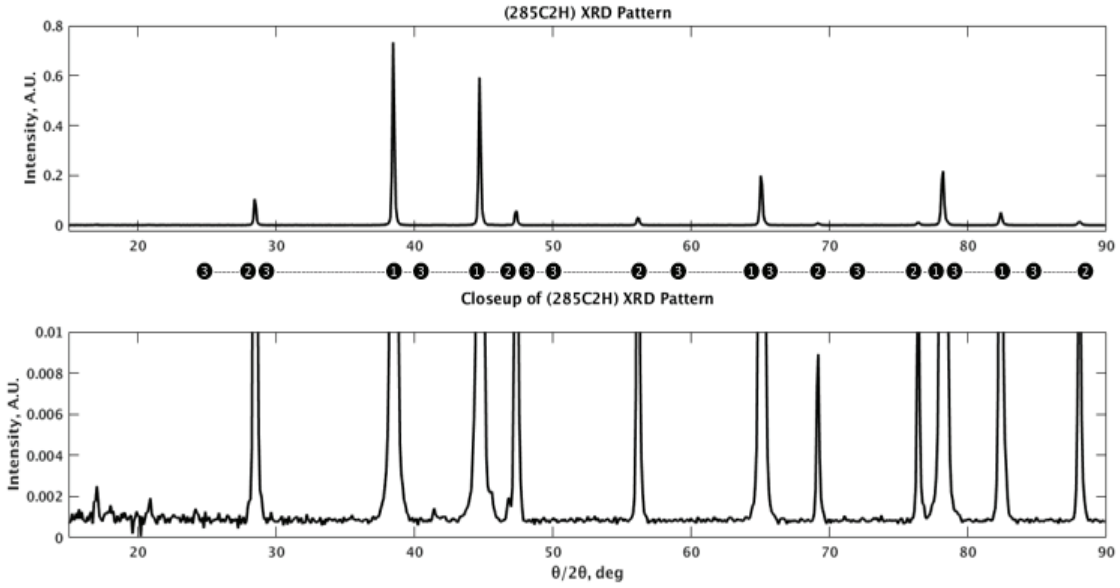


*Figure 49: XRD results for (285C2H). ① indicates Al peak, ② indicates Si peak, ③ indicates Mg2Si peak*

*Table 15: Mechanical properties and calculated n obtained from (285C2H) samples*

| Hardness, HV | YS, MPa | | UTS, MPa | | Elongation, % | | Strain Hardening Exponent, n (YS/UTS) | | |
|---|---|---|---|---|---|---|---|---|---|
| | Transverse | Longitudinal | Transverse | Longitudinal | Transverse | Longitudinal | Mean | Transverse | Longitudinal |
| 79.0±2.24 | 112.8 ±12.35 | 121.2±18.17 | 214.4±6.34 | 216.5±34.56 | 14.2±0.52 | 9.4±5.07 | .3442/.0733 | .3598/.0736 | .3286/.073 |

## *Stress Relief and HIP Only (285C2H/H)*

This section reports the results of the stress relief and HIP only (285C2H/H) samples. Figure 50 is a SEM micrograph of the microstructure with EDS elemental indications of each of the constituents. This figure shows that the typical microstructure consists of an aluminum-silicon matrix, spheroidal silicon particles, and long needle like precipitates being AlFeSi. This microstructure persists in all other post-processing conditions to follow.

Then in Figure 51 is the typical microstructures received in optical microscopy. The right side of Figure 51 is the histograms with fitted distributions for silicon particle size and interparticle spacing. Table 16 summarizes the quantitative results of that image analysis. In that table reported is the mean, mode, and standard deviation of silicon particle size. Also, the average number of silicon particles seen, the relative silicon percentage within the micrograph, and the mean and standard deviation of the silicon interparticle spacing. Lastly, reported in that table is the porosity. Figure 52 are micrographs of the grain structure at either 1000x or 2000x with the samples etched with Weck's reagent. Particularly in this condition the revealed grain structure was very light. Figure 53 is the XRD results for the stress relief and HIP only samples, with peaks indicated on the figure. Table 17 are the mechanical properties and calculated strain hardening exponent for this post-processing condition.

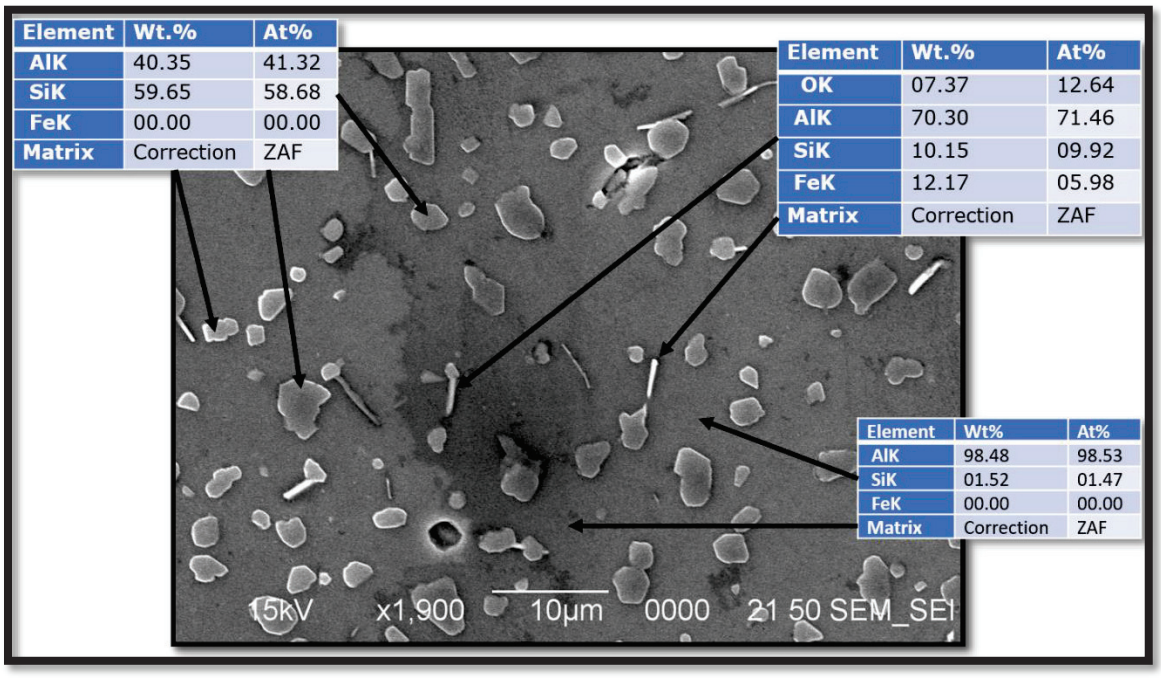


*Figure 50: SEM micrograph with microstructural constituents identified*

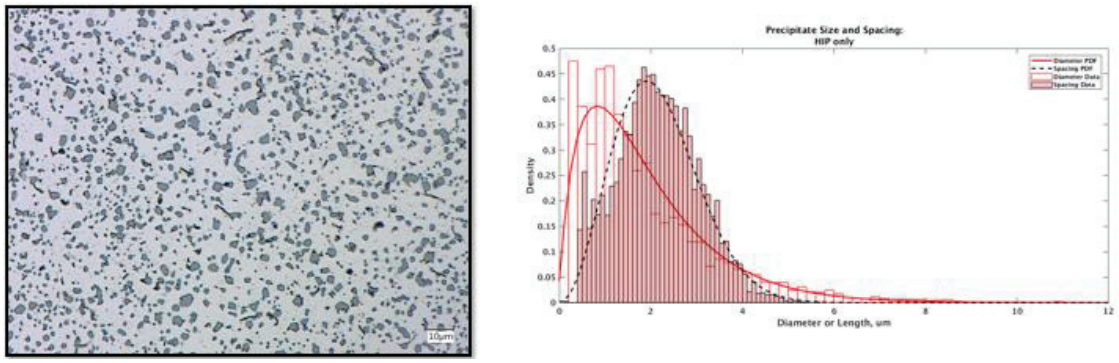


*Figure 51: (left) Microstructure; (right) OM observed silicon and spacing for (285C2H/H)*

*Table 16: Porosity and silicon particle results for (285C2H/H)*

| Porosity, % | Si Particle Info | | | | | Interparticle Spacing Info | |
|---|---|---|---|---|---|---|---|
| | Mean, um | Mode, um | SD, um | Number, # | Silicon % | Mean, um | SD, um |
| .11 | 2.41 | .3 | 1.40 | 6267 | 17.5 | 2.60 | .91 |

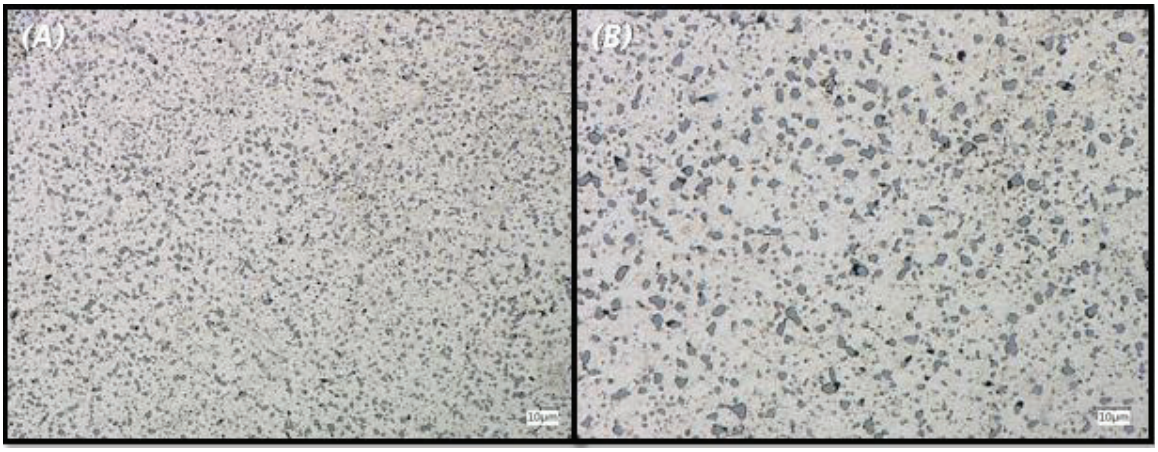


*Figure 52: (A & B) HIP grain structure at (A) 1000x and (B) 2000x condition (285C2H/H)*

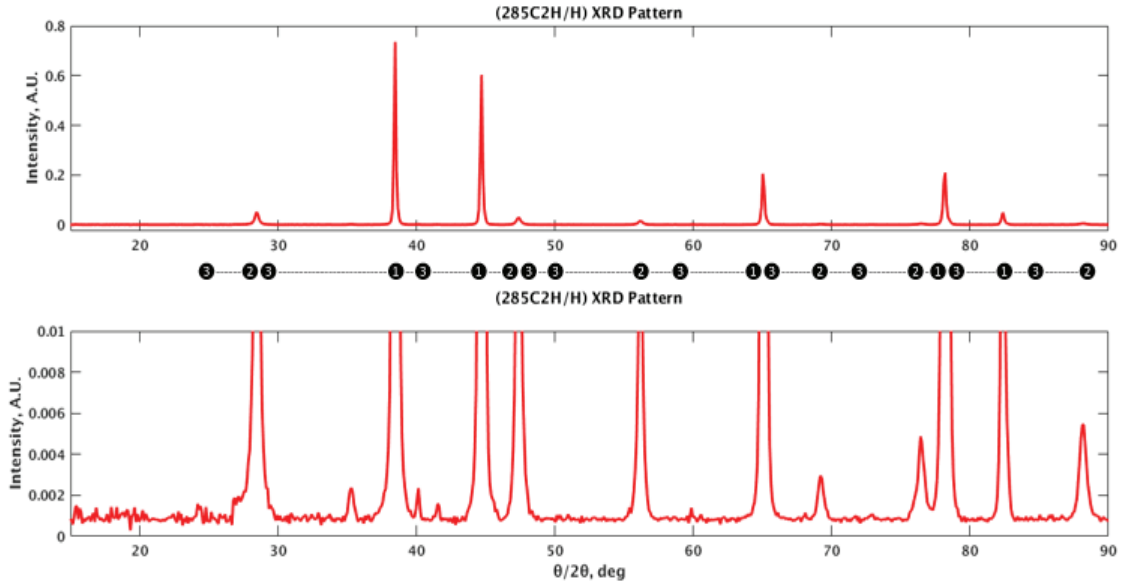


*Figure 53: XRD results for (285C2H/H). ① indicates Al peak, ② indicates Si peak, ③ indicates Mg2Si peak*

*Table 17: Mechanical properties and calculated* n *obtained from (285C2H/H) samples*

| Hardness, HV | YS, MPa | | UTS, MPa | | Elongation, % | | Strain Hardening Exponent, n (YS/UTS) | | |
|---|---|---|---|---|---|---|---|---|---|
| | Transverse | Longitudinal | Transverse | Longitudinal | Transverse | Longitudinal | Mean | Transverse | Longitudinal |
| 25.9±1.5 | 53.3 ±2.68 | 49.6±4.7 | 102.7±2.98 | 98.9±14.71 | 34.4±2.67 | 18.6±17.32 | .2163/.2964 | .2006/.3007 | .2319/.285 |

The results for all the other post-processing conditions will persist in a similar manner.

## *Forced Air Quench (285C2H/X/530C6H/FAQ/16H/160C6H)*

Below are the results gathered from the forced air quench (285C2H/X/530C6H/FAQ/16H/160C6H) condition. Figure 54has multiple components;

the left side being optical micrographs and right side being the silicon particle size and interparticle spacing distributions. The figure is then further separated from top to bottom with the non-HIP condition displayed on top and the HIP condition shown in the bottom of the figure. Table 18 is the quantitative results gathered from Figure 54. *A&B* in Figure 55 are the non-HIP grain structures at 1000x and 2000x optical magnification and subsequently *C&D* are the HIP grain structures. The grain structure in this condition is more apparent than the stress relief and HIP only condition. Between the top and bottom of the figure there is also an apparent reduction in porosity due to the HIP. This is corroborated by the results reported in Table 18. The XRD results for both the non-HIP and HIP force air quench are shown in Figure 56. The HIP spectrum is designated as the solid line on the figure and the non-HIP spectrum is the dashed line on the figure. Table 19 is the comparison between non-HIP and HIP mechanical properties gathered in the investigation.

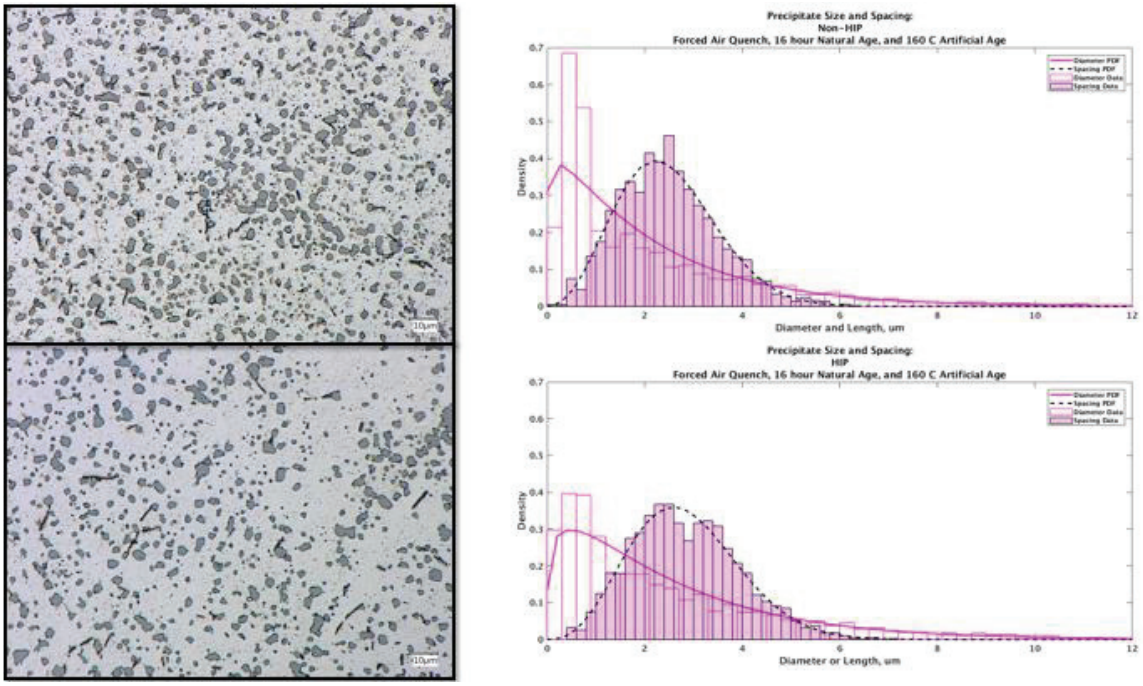


*Figure 54: (left, top (NH) and bottom (HIP)) Microstructure; (right, top (NH) and bottom (HIP)) OM observed silicon and spacing for (285C2H/X/530C6H/FAQ/16H/160C6H)*

*Table 18: Porosity and silicon particle results for (285C2H/X/530C6H/FAQ/16H/160C6H)*

| Condition | Porosity, % | Si Particle Info | | | | | Interparticle Spacing Info | |
|---|---|---|---|---|---|---|---|---|
| | | Mean, um | Mode, um | SD, um | Number, # | Silicon % | Mean, um | SD, um |
| Non-HIP | .54 | 2.13 | .45 | 2.06 | 2884 | 19.3 | 2.37 | 1.0 |
| HIP | .08 | 2.69 | .45 | 2.32 | 7257 | 18.2 | 2.93 | 1.1 |

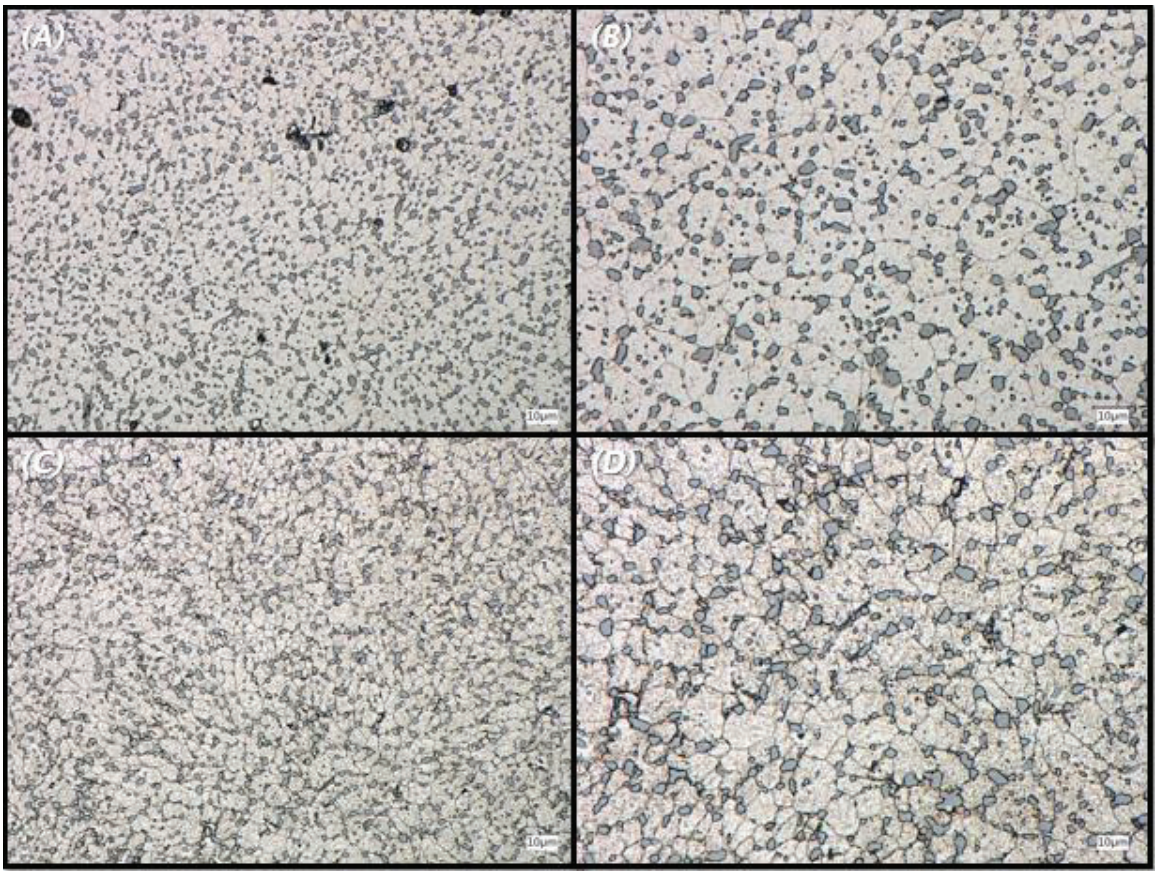


*Figure 55: (A & B) NH grain structure at (A) 1000x and (B) 2000x; (C & D) HIP grain structure at (C) 1000x and (D) 2000x condition (285C2H/X/530C6H/FAQ/16H/160C6H)*

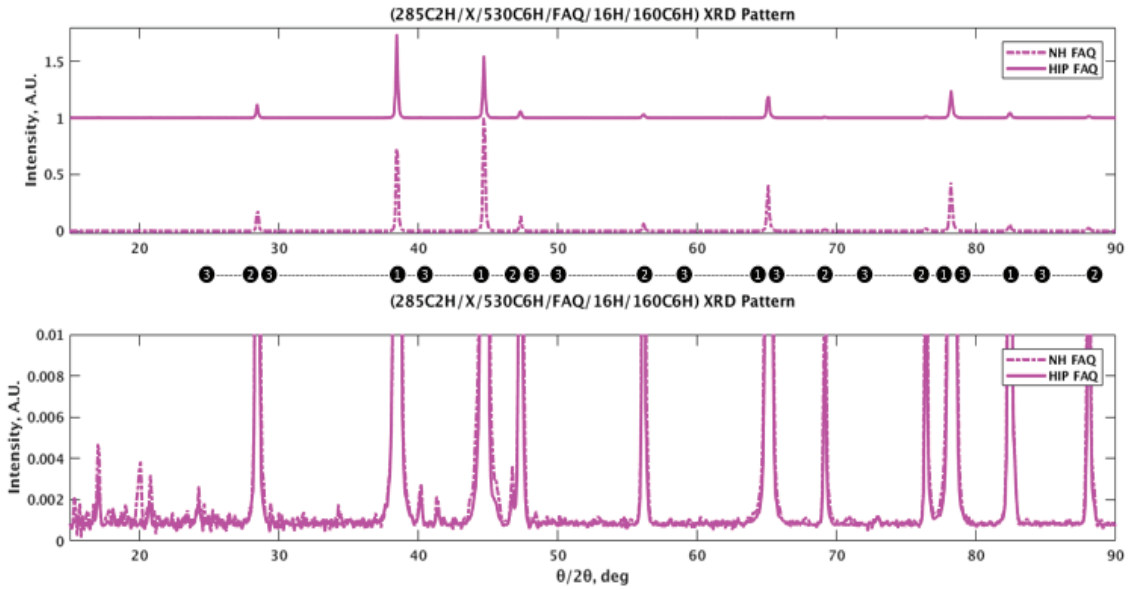


*Figure 56: XRD results for (285C2H/X/530C6H/FAQ/16H/160C6H). ① indicates Al peak, ② indicates Si peak, ③ indicates Mg2Si peak*

*Table 19: Hardness results and estimated properties calculated from* n *for (285C2H/X/530C6H/FAQ/16H/160C6H) samples*

| Condition | Hardness, HV | YS, MPa (Est) | UTS, MPa (Est) | Strain Hardening Exponent, n (YS/UTS) |
|---|---|---|---|---|
| Non-HIP | 37.9±1.8 | 83.5 | 130.9 | .171/.215 |
| HIP | 39.4±1.4 | 90.6 | 127.0 | .1525/.1455 |

## *Hot Water Quench (285C2H/X/530C6H/HWQ/16H/160C6H)*

What follows are the results gathered from the hot water quench (285C2H/X/530C6H/HWQ/16H/160C6H) condition. Figure 57 has multiple components; the left side being optical micrographs and right side being the silicon particle size and interparticle spacing distributions. The figure is then further separated from top to bottom with the non-HIP condition displayed on top and the HIP condition shown in the bottom of the figure. Table 20 is the quantitative results gathered from Figure 57. *A&B* in Figure 58 are the non-HIP grain structures at 1000x and 2000x optical magnification and subsequently *C&D* are the HIP grain structures. The grain structure in this condition is similar to that observed in the forced air quench condition. Between the top and bottom of the figure there is also an apparent reduction in porosity due to the HIP. This is corroborated by the results reported in Table 20. The XRD results for both the non-HIP and HIP force air quench are shown in Figure 59. The HIP spectrum is designated as the solid line on the figure and the non-HIP spectrum is the dashed line on the figure. Table 21 is the comparison between non-HIP and HIP mechanical properties gathered in the investigation.

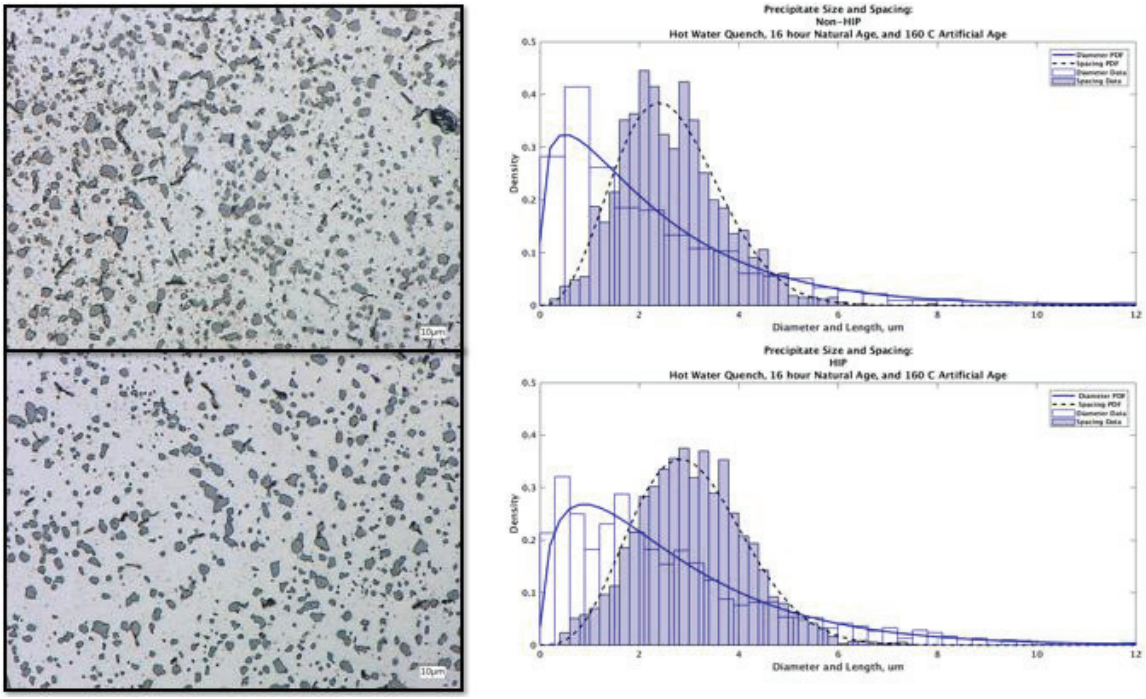


*Figure 57: (left, top (NH) and bottom (HIP)) Microstructure; (right, top (NH) and bottom (HIP)) OM observed silicon and spacing for (285C2H/X/530C6H/HWQ/16H/160C6H)*

*Table 20: Porosity and silicon particle results for (285C2H/X/530C6H/HWQ/16H/160C6H)*

| Condition | Porosity, % | Si Particle Info | | | | | Interparticle Spacing Info | |
|---|---|---|---|---|---|---|---|---|
| | | Mean, um | Mode, um | SD, um | Number, # | Silicon % | Mean, um | SD, um |
| Non-HIP | .28 | 2.28 | .75 | 2.06 | 2695 | 17.2 | 2.57 | 1.03 |
| HIP | .15 | 2.72 | .45 | 2.22 | 4099 | 16.6 | 2.99 | 1.12 |

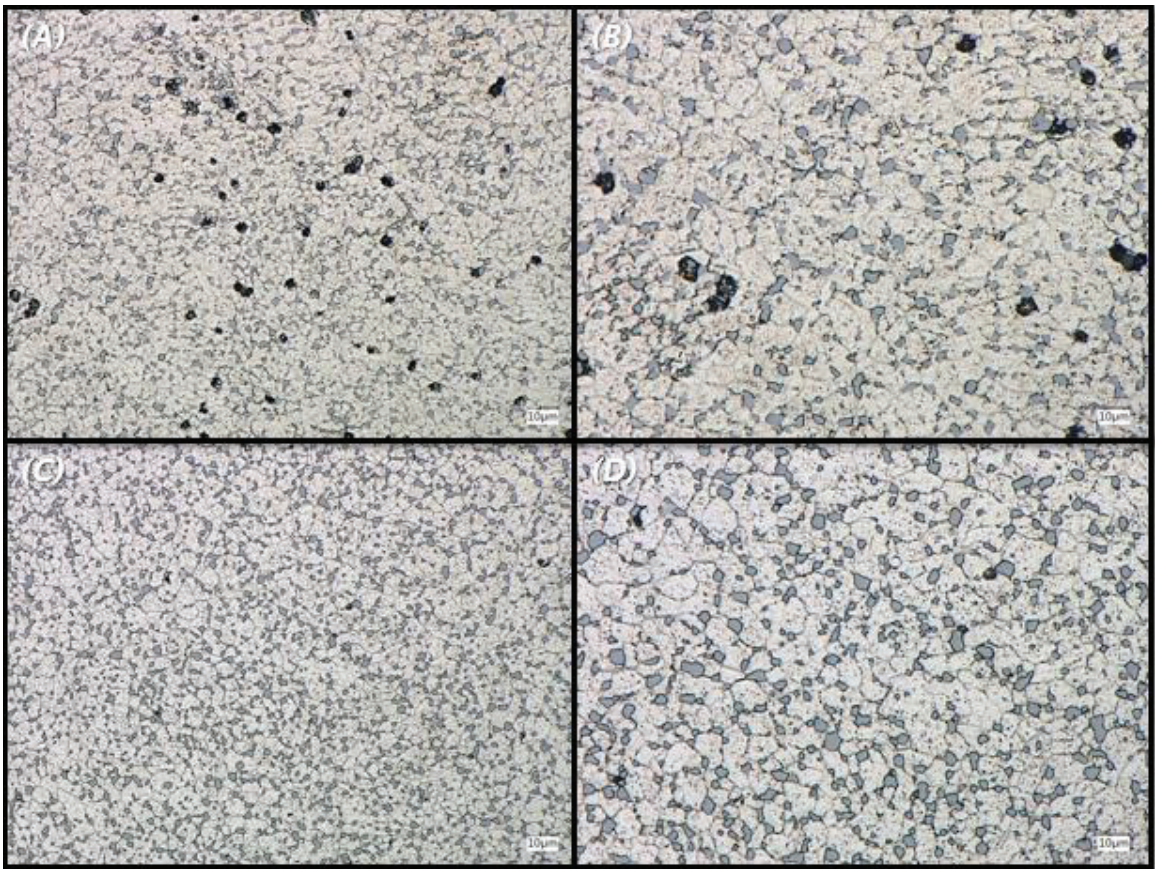


*Figure 58: (A & B) NH grain structure at (A) 1000x and (B) 2000x; (C & D) HIP grain structure at (C) 1000x and (D) 2000x condition (285C2H/X/530C6H/HWQ/16H/160C6H)*

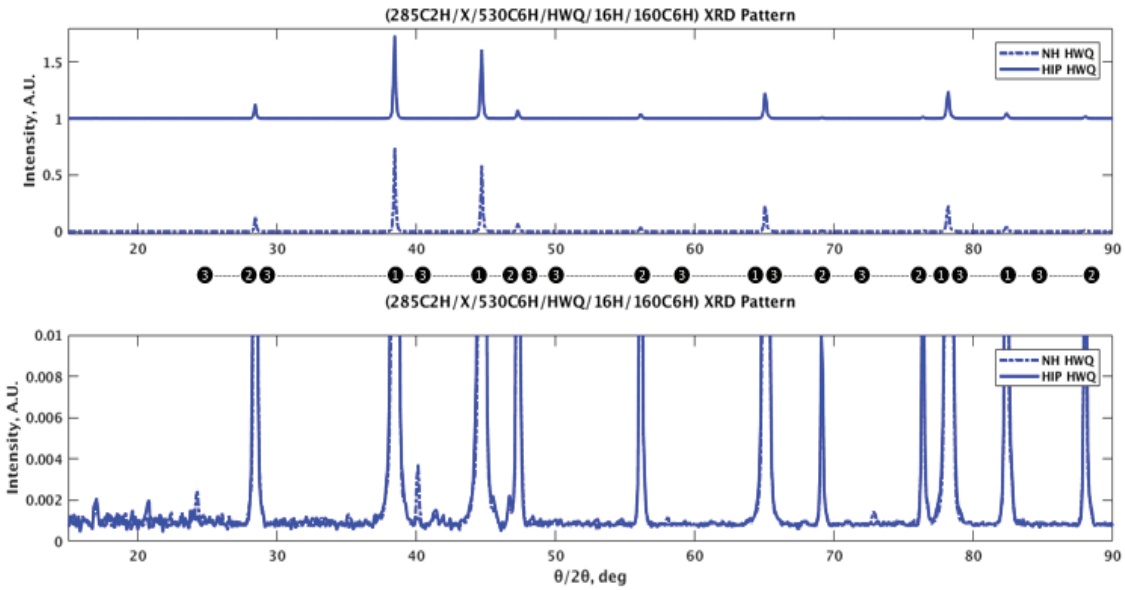


*Figure 59: XRD results for (285C2H/X/530C6H/HWQ/16H/160C6H). ① indicates Al peak, ② indicates Si peak, ③ indicates $Mg_2Si$ peak*

*Table 21: Mechanical properties, both obtained and estimated, for (285C2H/X/530C6H/HWQ/16H/160C6H) samples*

| Condition | Hardness, HV | YS, MPa | | UTS, MPa | | Elongation, % | | Strain Hardening Exponent, n (YS/UTS) | | |
|---|---|---|---|---|---|---|---|---|---|---|
| | | Transverse | Longitudinal | Transverse | Longitudinal | Transverse | Longitudinal | Mean | Transverse | Longitudinal |
| Non-HIP | 58.9±8.8 | 155.9 ±13.8 | 169.9±31 | 256.3±14.5 | 250.1±5.5 | 16.4±2.64 | 13.2±3.86 | .0728/.352 | .0914/.3584 | .0541/.3456 |
| HIP | 60.5±4.3 | 167.1 (Est) | | 260.0 (Est) | | - | - | .0728/.352 | - | - |

## *Ethylene Glycol Quench (285C2H/X/530C6H/GQ/16H/160C6H)*

Contained below are the results gathered from the glycol quench (285C2H/X/530C6H/GQ/16H/160C6H) condition. Figure 60 has multiple components; the left side being optical micrographs and right side being the silicon particle size and interparticle spacing distributions. The figure is then further separated from top to bottom with the non-HIP condition displayed on top and the HIP condition shown in the bottom of the figure. Table 22 is the quantitative results gathered from Figure 60. *A&B* in Figure 61 are the non-HIP grain structures at 1000x and 2000x optical magnification and subsequently *C&D* are the HIP grain structures. The grain structure in this condition is the starkest yet shown. The Weck's reagent had different effects on differently processed samples. The XRD results for both the non-HIP and HIP force air quench are shown in Figure 62. The HIP spectrum is designated as the solid line on the figure and the non-HIP spectrum is the dashed line on the figure. Table 23 is the comparison between non-HIP and HIP mechanical properties gathered in the investigation.

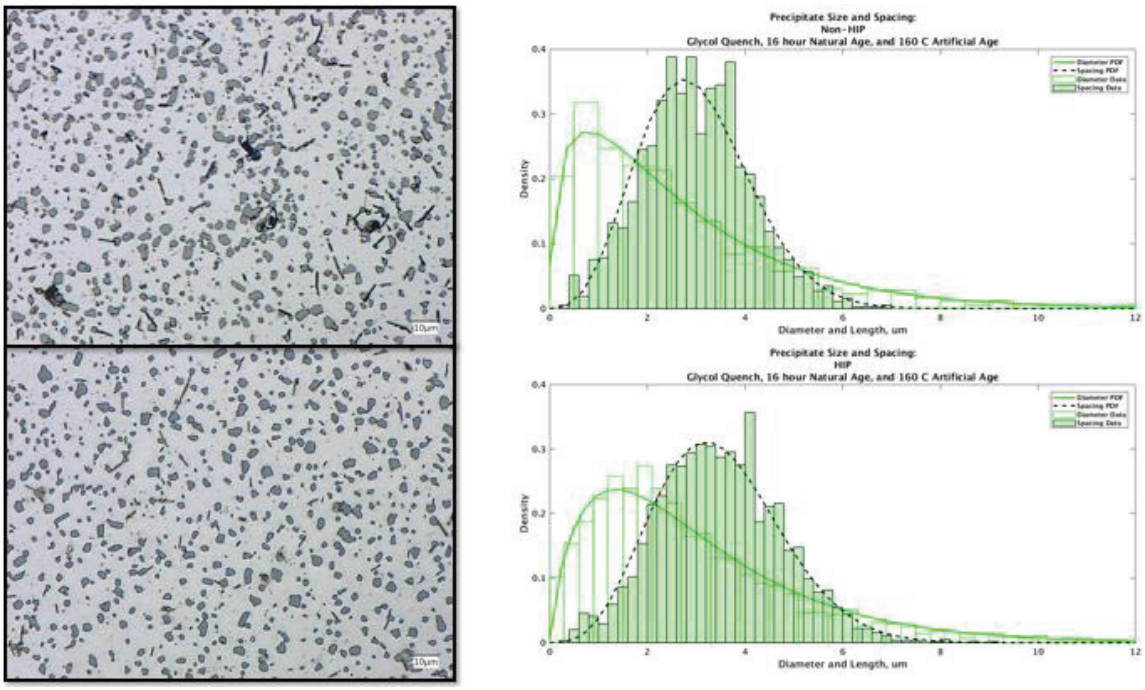


*Figure 60: (left, top (NH) and bottom (HIP)) Microstructure; (right, top (NH) and bottom (HIP)) OM observed silicon and spacing for (285C2H/X/530C6H/GQ/16H/160C6H)*

*Table 22: Porosity and silicon particle results for (285C2H/X/530C6H/GQ/16H/160C6H)*

| Condition | Porosity, % | Si Particle Info | | | | | Interparticle Spacing Info | |
|---|---|---|---|---|---|---|---|---|
| | | Mean, um | Mode, um | SD, um | Number, # | Silicon % | Mean, um | SD, um |
| **Non-HIP** | .36 | 2.62 | .75 | 2.26 | 1860 | 19.04 | 2.89 | 1.12 |
| **HIP** | .03 | 2.92 | 1.95 | 2.29 | 3049 | 16.3 | 3.36 | 1.27 |

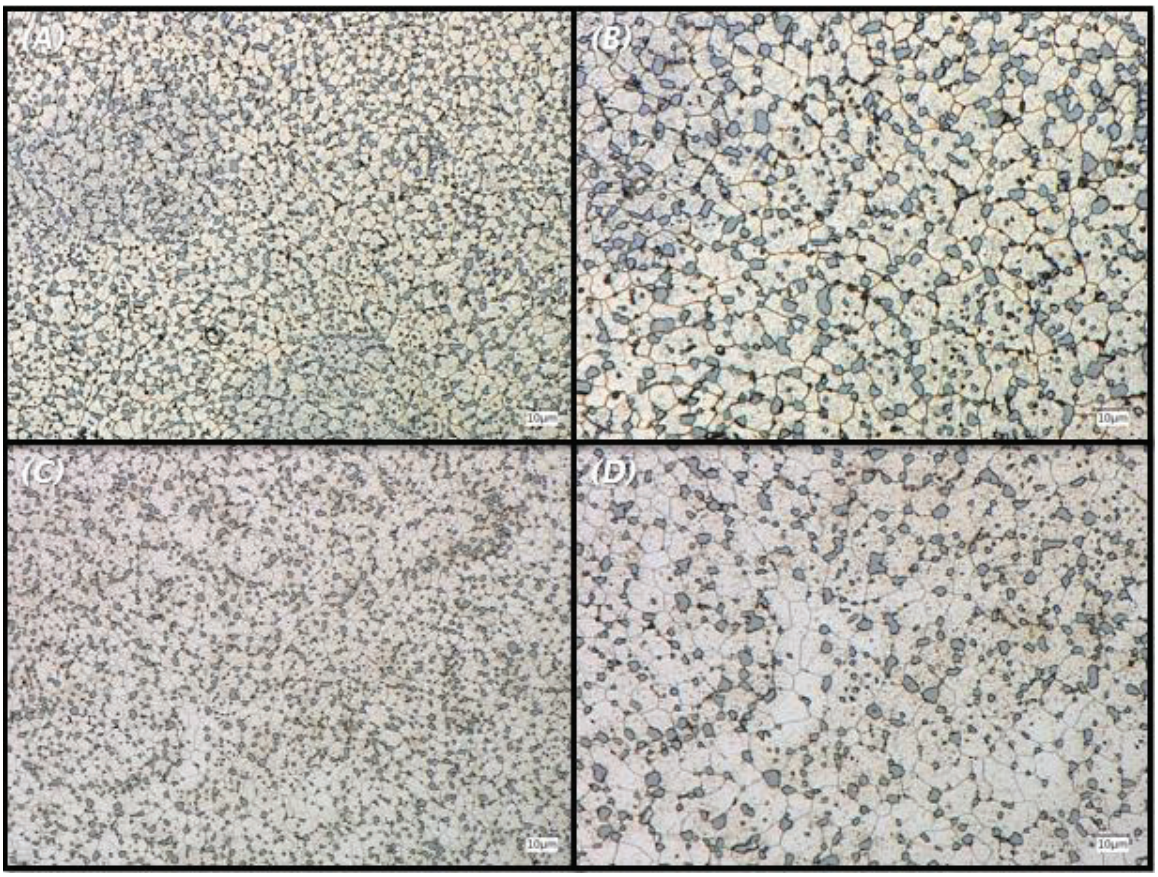


*Figure 61: (A & B) NH grain structure at (A) 1000x and (B) 2000x; (C & D) HIP grain structure at (C) 1000x and (D) 2000x condition (285C2H/X/530C6H/GQ/16H/160C6H)*

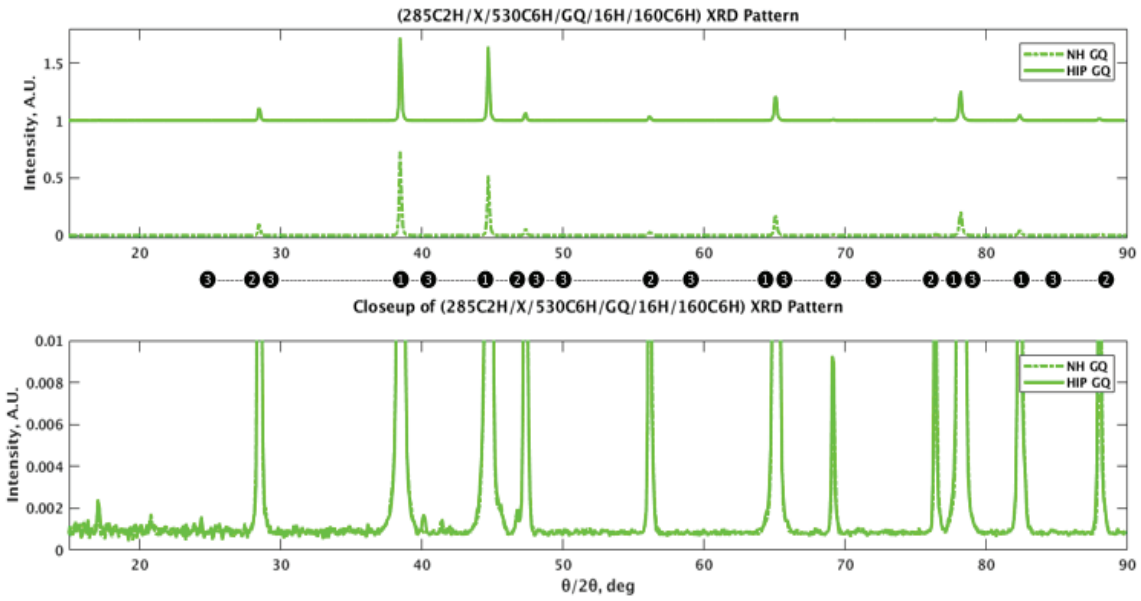


*Figure 62: XRD results for (285C2H/X/530C6H/GQ/16H/160C6H). ① indicates Al peak, ② indicates Si peak, ③ indicates $Mg_2Si$ peak*

*Table 23: Hardness results and estimated properties calculated from* n *for (285C2H/X/530C6H/GQ/16H/160C6H) samples*

| Condition | Hardness, HV | YS, MPa (Est) | UTS, MPa (Est) | Strain Hardening Exponent, n (YS/UTS) |
|---|---|---|---|---|
| Non-HIP | 79.3±4.4 | 177.8 | 262.2 | .1636/.1744 |
| HIP | 81.6±3.7 | 183.0 | 269.8 | |

## *Room Temperature Water Quench (285C2H/X/530C6H/RTWQ/X/X)*

16 Hour Natural Age and 160℃ Artificial Age (T6)

Next are the results gathered from the room temperature water quench (285C2H/X/530C6H/RTWQ/16H/160C6H) condition. Figure 63 has multiple components; the left side being optical micrographs and right side being the silicon particle size and interparticle spacing distributions. The figure is then further separated from top to bottom with the non-HIP condition displayed on top, and the HIP condition shown in the bottom of the figure. Table 24 is the quantitative results gathered from Figure 63. *A&B* in Figure 64 are the non-HIP grain structures at 1000x and 2000x optical magnification and subsequently *C&D* are the HIP grain structures. The XRD results for both the non-HIP and HIP force air quench are shown in Figure 65. The HIP spectrum is designated as the solid line on the figure, and the non-HIP spectrum is the dashed line on the figure. Table 25 is the comparison between non-HIP and HIP mechanical properties gathered in the investigation. Additionally, an age-hardening study was performed on this post-processing condition and the results of which are contained in Figure 66.

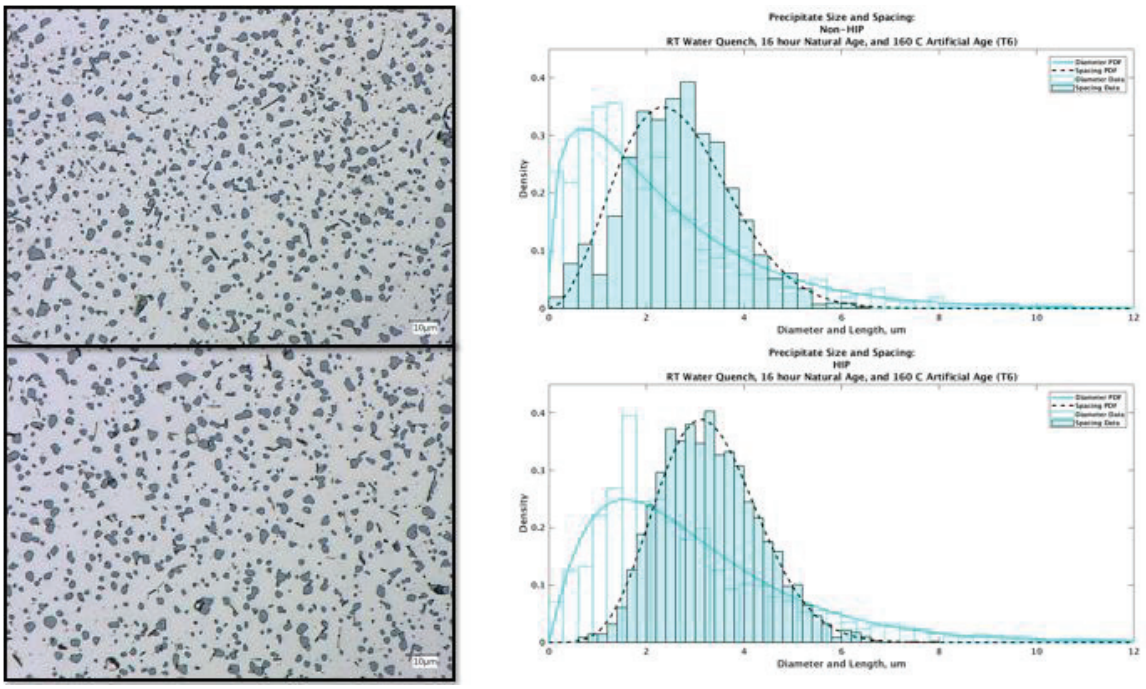


*Figure 63: (left, top (NH) and bottom (HIP)) Microstructure; (right, top (NH) and bottom (HIP)) OM observed silicon and spacing for (285C2H/X/530C6H/RTWQ/16H/160C6H)*

*Table 24: Porosity and silicon particle results for (285C2H/X/530C6H/RTWQ/16H/160C6H)*

| Condition | Porosity, % | Si Particle Info | | | | | Interparticle Spacing Info | |
|---|---|---|---|---|---|---|---|---|
| | | Mean, um | Mode, um | SD, um | Number, # | Silicon % | Mean, um | SD, um |
| Non-HIP | .36 | 2.3 | 1.35 | 1.94 | 1448 | 13.9 | 2.68 | 1.13 |
| HIP | .07 | 2.99 | 1.65 | 2.06 | 3692 | 20.3 | 3.31 | 1.02 |

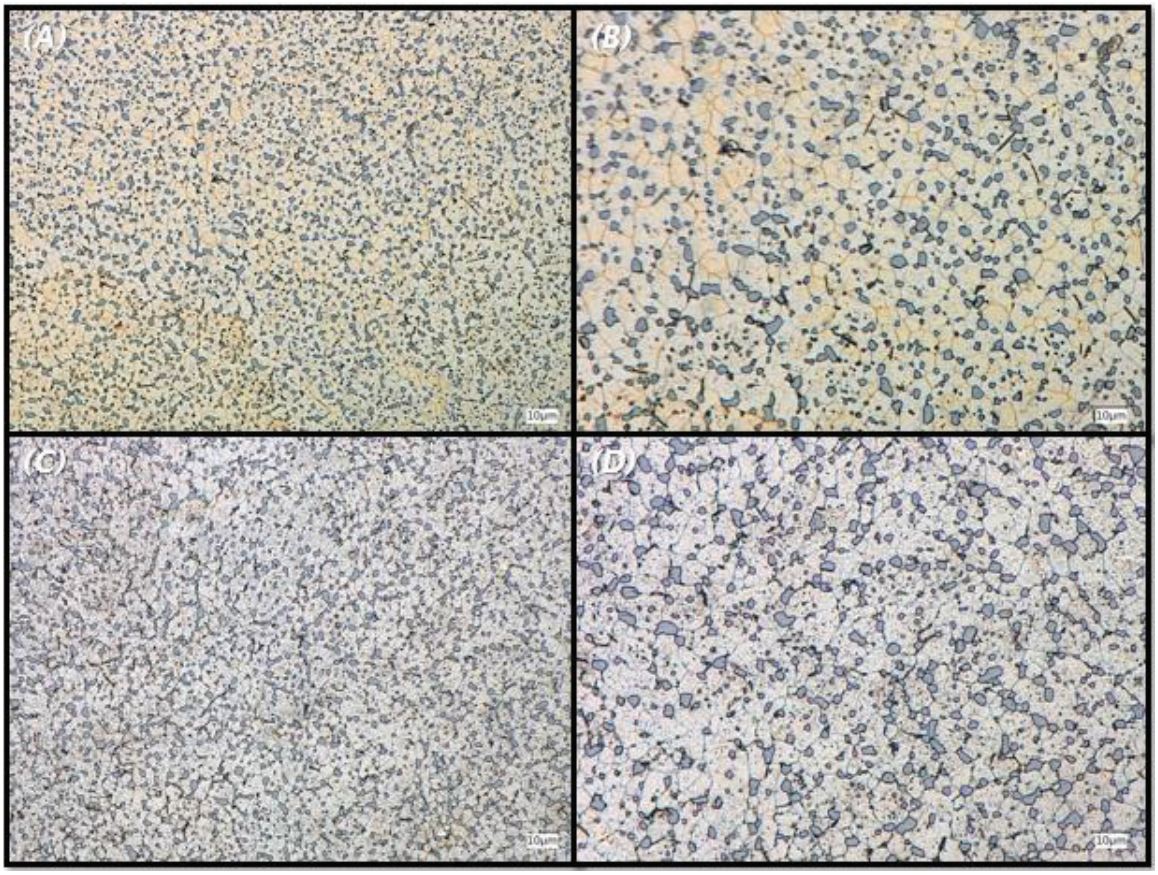


*Figure 64: (A & B) NH grain structure at (A) 1000x and (B) 2000x; (C & D) HIP grain structure at (C) 1000x and (D) 2000x condition (285C2H/X/530C6H/RTWQ/16H/160C6H)*

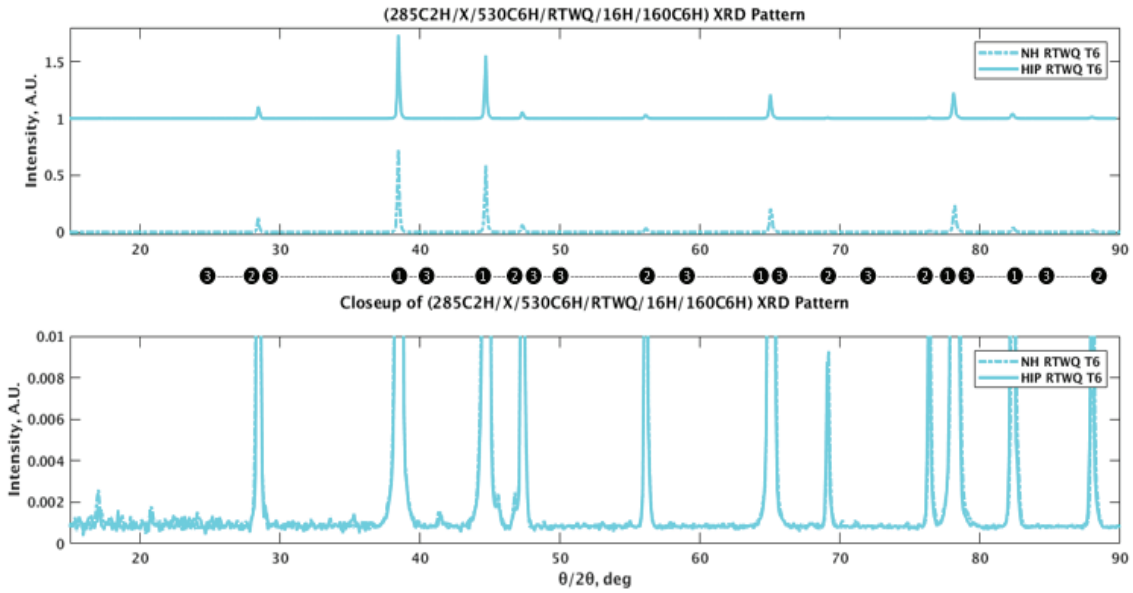


*Figure 65: XRD results for (285C2H/X/530C6H/RTWQ/16H/160C6H). ① indicates Al peak, ② indicates Si peak, ③ indicates $Mg_2Si$ peak*

*Table 25: Mechanical properties and calculated* n *obtained from (285C2H/X/530C6H/RTWQ/16H/160C6H) samples*

| Condition | Hardness, HV | YS, MPa | | UTS, MPa | | Elongation, % | | Strain Hardening Exponent, n (YS/UTS) | | |
|---|---|---|---|---|---|---|---|---|---|---|
| | | Transverse | Longitudinal | Transverse | Longitudinal | Transverse | Longitudinal | Mean | Transverse | Longitudinal |
| **Non-HIP** | 79.9±2.7 | 136.8 ±1.2 | 143.8±15.8 | 250.3±7.9 | 238.9±17.1 | 13.1±1.7 | 8.5±5.7 | .27/.0782 | .2808/.0835 | .2591/.073 |
| **HIP** | 76.4±1.7 | 170.8±14.4 | 150.9±8.7 | 262.5±8.5 | 242.2±3.5 | 17.0±1.3 | 17.4±2.9 | .192/.1637 | .1652/.2095 | .2189/.118 |

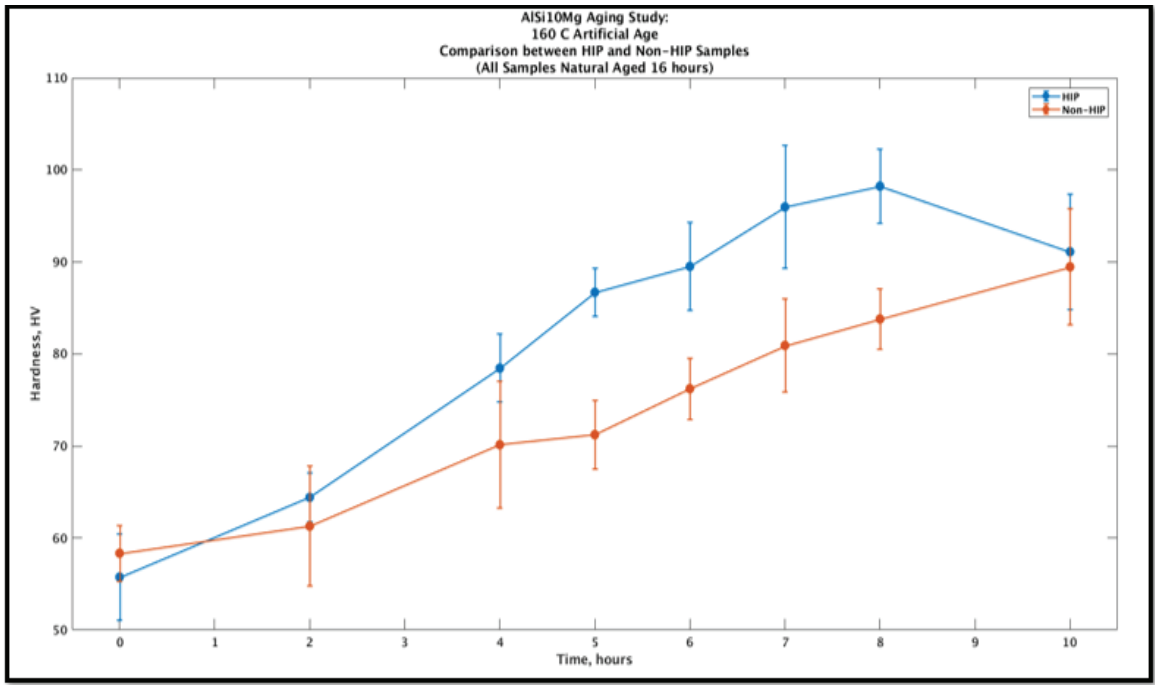


*Figure 66: Artificial aging behavior for (285C2H/X/530C6H/RTWQ/16H/160CXH)*

### 1 Hour Natural Age and 160℃ Artificial Age (T6)

Below are the mechanical properties for the (285C2H/H/530C6H/RTWQ/1H/160C6H) condition. As samples from this condition were post-processed by Oerlikon, only the mechanical properties are available. This is due to these samples primarily being used in other portions of the MAMLS project.

*Table 26: Mechanical properties and calculated* n *obtained from (285C2H/H/530C6H/RTWQ/1H/160C6H) samples*

| Condition | Hardness, HV | YS, MPa | | UTS, MPa | | Elongation, % | | Strain Hardening Exponent, n (YS/UTS) | | |
|---|---|---|---|---|---|---|---|---|---|---|
| | | Transverse | Longitudinal | Transverse | Longitudinal | Transverse | Longitudinal | Mean | Transverse | Longitudinal |
| **HIP** | 106.1±5.3 | 271.9±4.9 | 263.3±10.3 | 339.±5.9 | 318.3±28.8 | 12.0 | 14.7 | .1127/.074 | .1057/.1831 | .1197/.0708 |

## 16 Hour Natural Age and 205℃ Artificial Age (T7)

Below are the results gathered from the room temperature water quench (285C2H/X/530C6H/RTWQ/16H/205C4.5H) condition. Figure 67 has multiple components; the left side being optical micrographs and right side being the silicon particle size and interparticle spacing distributions. The figure is then further separated from top to bottom with the non-HIP condition displayed on top and the HIP condition shown in the bottom of the figure. Table 27 is the quantitative results gathered from Figure 67. *A&B* in Figure 68 are the non-HIP grain structures at 1000x and 2000x optical magnification and subsequently *C&D* are the HIP grain structures. The XRD results for both the non-HIP and HIP force air quench are shown in Figure 69. The HIP spectrum is designated as the solid line on the figure and the non-HIP spectrum is the dashed line on the figure. Table 28 is the comparison between non-HIP and HIP mechanical properties gathered in the investigation. Additionally, an age-hardening study was performed on this post-processing condition and the results of which are contained in Figure 70.

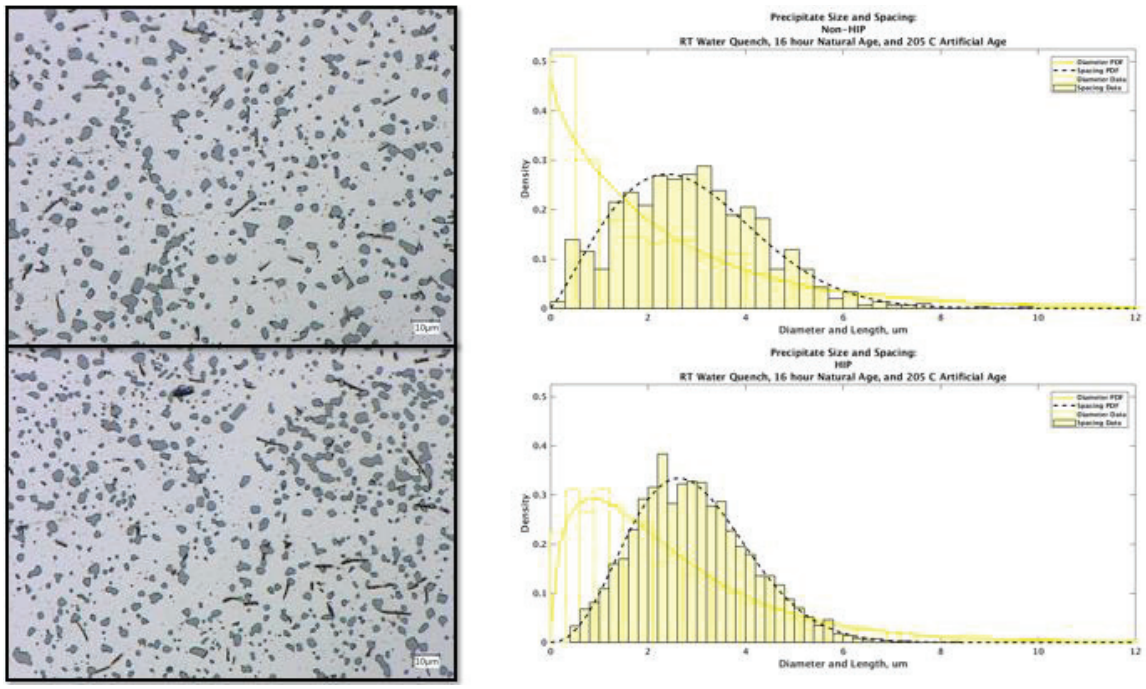


*Figure 67: (left, top (NH) and bottom (HIP)) Microstructure; (right, top (NH) and bottom (HIP)) OM observed silicon and spacing for (285C2H/X/530C6H/RTWQ/16H/205C4.5H)*

*Table 27: Porosity and silicon particle results for (285C2H/X/530C6H/RTWQ/16H/205C4.5H)*

| Condition | Porosity, % | Si Particle Info | | | | | Interparticle Spacing Info | |
|---|---|---|---|---|---|---|---|---|
| | | Mean, um | Mode, um | SD, um | Number, # | Silicon % | Mean, um | SD, um |
| Non-HIP | .74 | 2.41 | .25 | 2.41 | 1077 | 17.1 | 2.75 | 1.46 |
| HIP | .06 | 2.98 | 1.05 | 2.0 | 3511 | 14.7 | 2.75 | 1.18 |

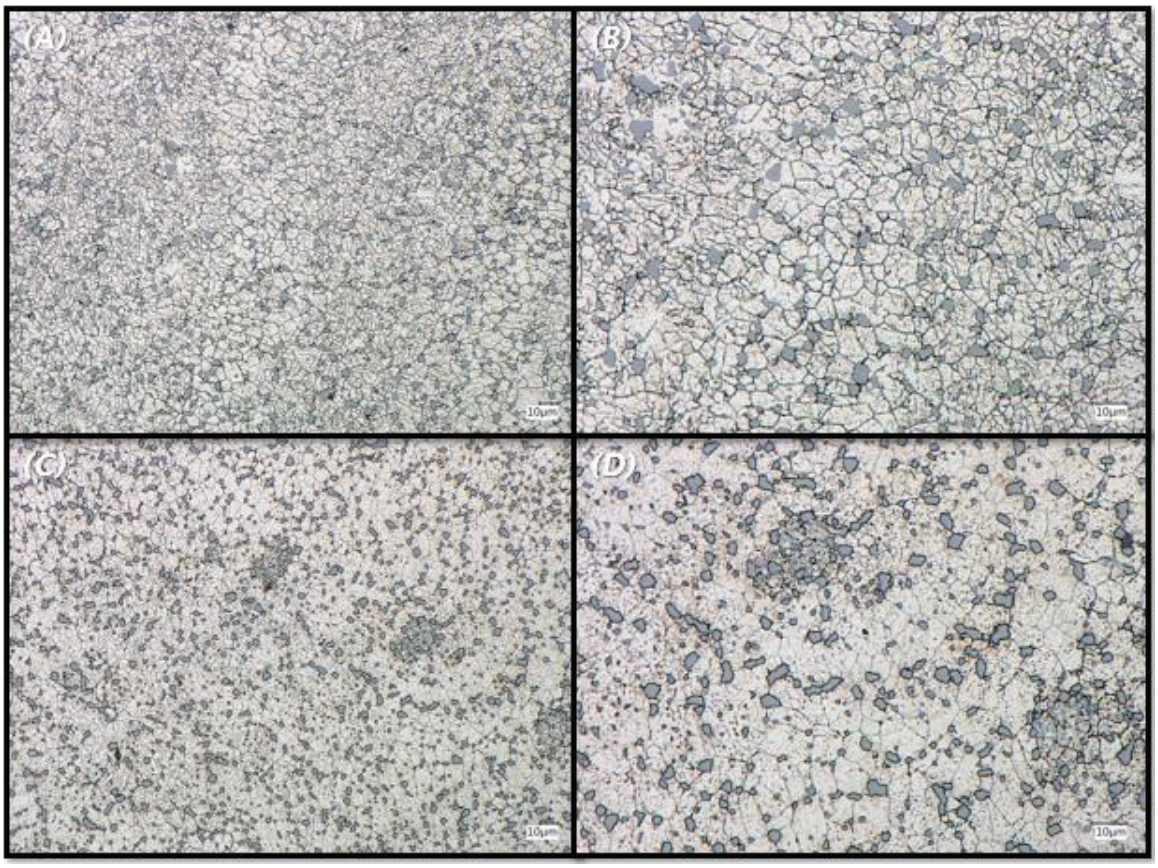


*Figure 68: (A & B) NH grain structure at (A) 1000x and (B) 2000x; (C & D) HIP grain structure at (C) 1000x and (D) 2000x condition (285C2H/X/530C6H/RTWQ/16H/205C4.5H)*

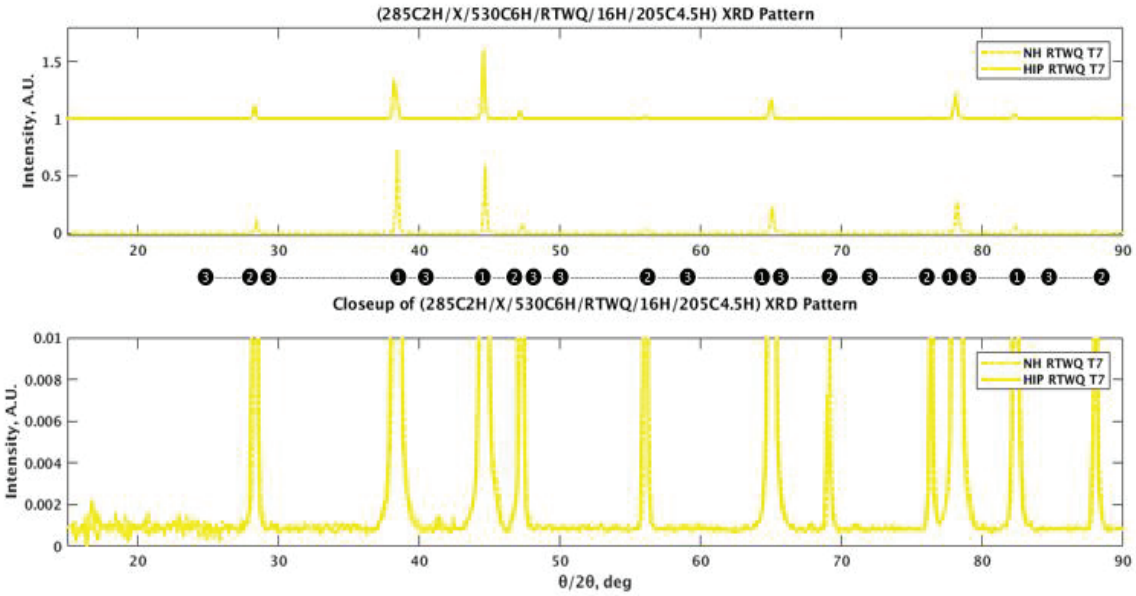


*Figure 69: XRD results for (285C2H/X/530C6H/RTWQ/16H/205C4.5H). ① indicates Al peak, ② indicates Si peak, ③ indicates $Mg_2Si$ peak*

*Table 28: Mechanical properties, both obtained and estimated, from (285C2H/X/530C6H/RTWQ/16H/205C4.5H) samples*

| Condition | Hardness, HV | YS, MPa | | UTS, MPa | | Elongation, % | | Strain Hardening Exponent, n (YS/UTS) | | |
|---|---|---|---|---|---|---|---|---|---|---|
| | | Transverse | Longitudinal | Transverse | Longitudinal | Transverse | Longitudinal | Mean | Transverse | Longitudinal |
| Non-HIP | 95.5±3.7 | 191.5 (Est) | | 299.1 (Est) | | - | - | .2123/.074 | - | - |
| HIP | 104.5±5.2 | 201.5±12.8 | 218.0±21.3 | 248.6±6.4 | 269.5±11.6 | 12.0±2.1 | 8.8±4.6 | .2123/.074 | .2294/.0741 | .1952/.074 |

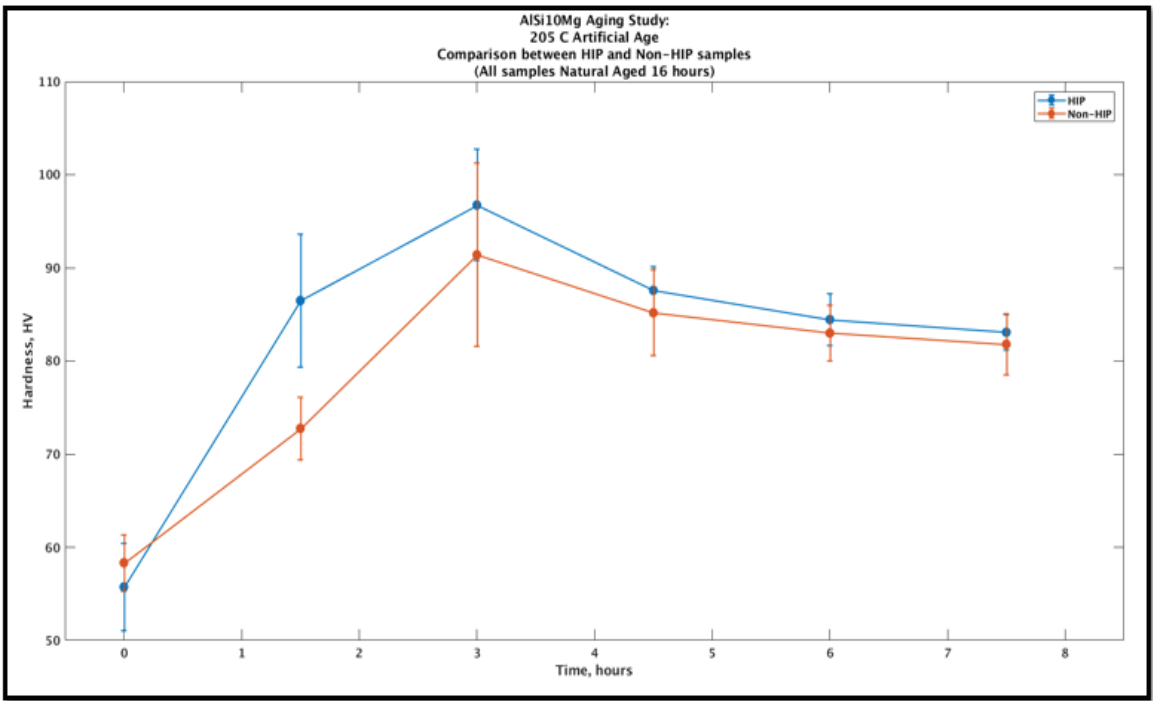


*Figure 70: Artificial aging behavior for (285C2H/X/530C6H/RTWQ/16H/205CXH)*

## *Summary*

This section summarizes all of the results gathered in this investigation. Figure 71, Figure 72, Figure 73, and Figure 74 cover the silicon particle size results. Figure 75 shows the grain size, Hall-Petch, relationship between all of the different post-processing conditions, and Figure 76 shows the mechanical property results with trends illustrated. Lastly, Figure 77 shows the combined results of the age-hardening behavior.

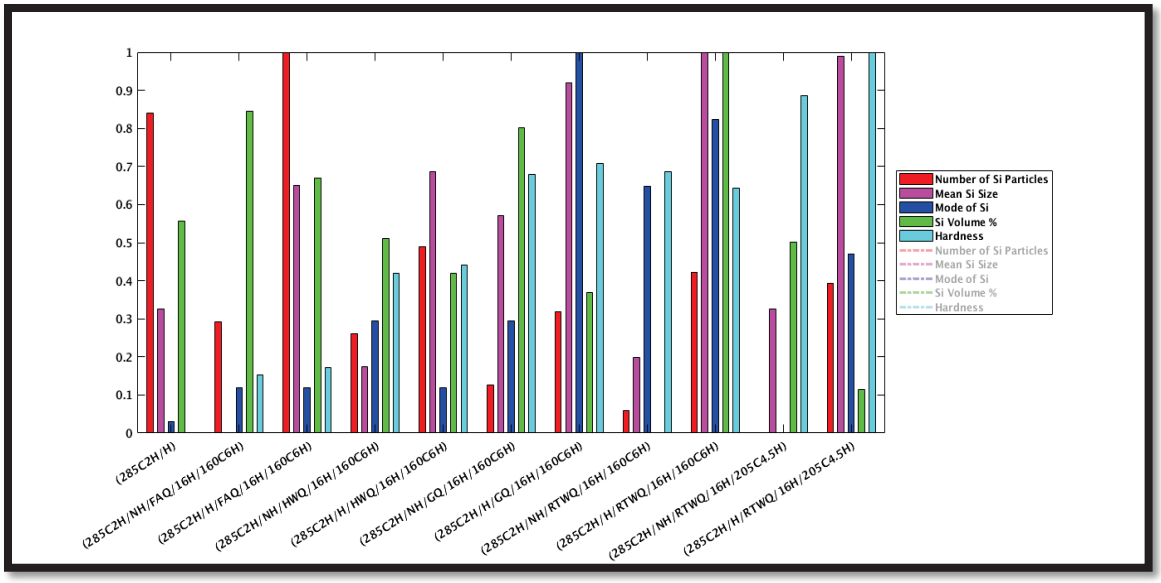


*Figure 71: Summary results of silicon particle data in all applicable post-processing conditions*

The general structure of Figure 71, Figure 72, and Figure 73 consists of the post processing conditions listed starting with (285C2H) at the left and working through the various conditions as a function of increasing quench rate. Also, a general feature of these figures is that the data is normalized between zero and one to eliminate disparities in order of magnitude and to elicit a better visualization of the trends present. The trend line present on Figure 72 designates the number of silicon particles observed in optical microscopy for a given sample condition and loosely decreases from left to right for increasing quench rate. The data exhibits a cyclic nature where the number of particles observed in the non-HIP condition are significantly lower than the number of particles observed in the hip condition. The trend lines in Figure 73 show an increase in hardness directly correlating to an increasing quench rate. Anecdotally, this has been known and reported in the literature. Also, in general the mean silicon particle size seen in optical microscopy increases along with the hardness. Again, there is a somewhat cyclic character as demonstrated in Figure

72 where differences arise between the non-HIP and HIP condition in the form of increased mean feret diameter in HIP versus non-HIP samples.

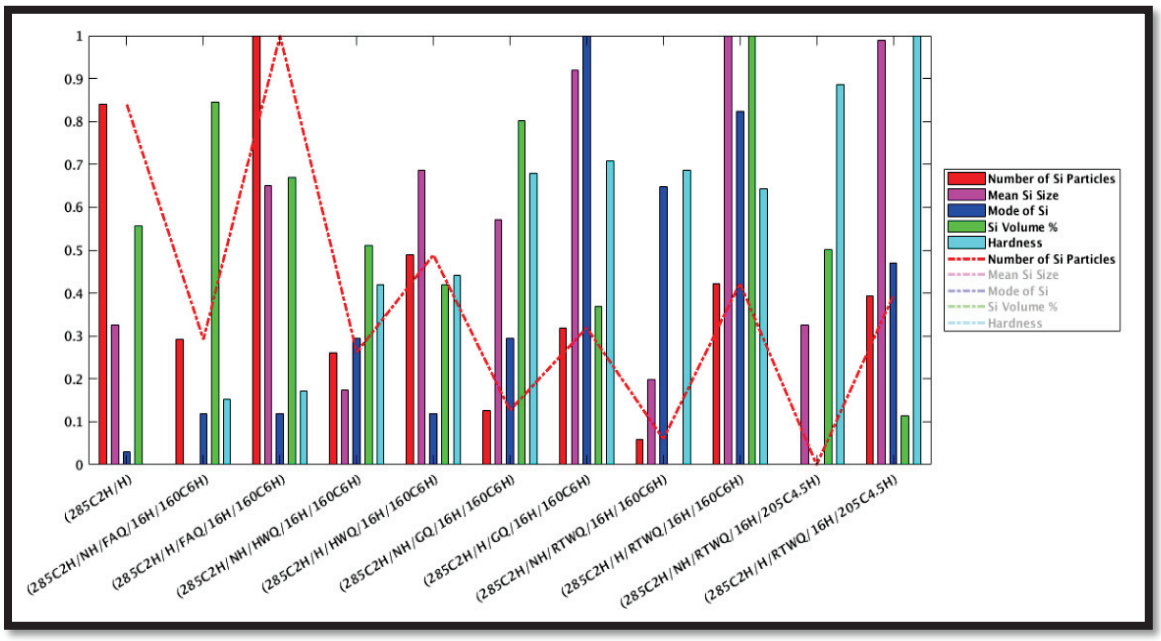


*Figure 72: Summary results of silicon particles with trend line drawn highlighting the number of particles observed in all applicable post-processing condition*

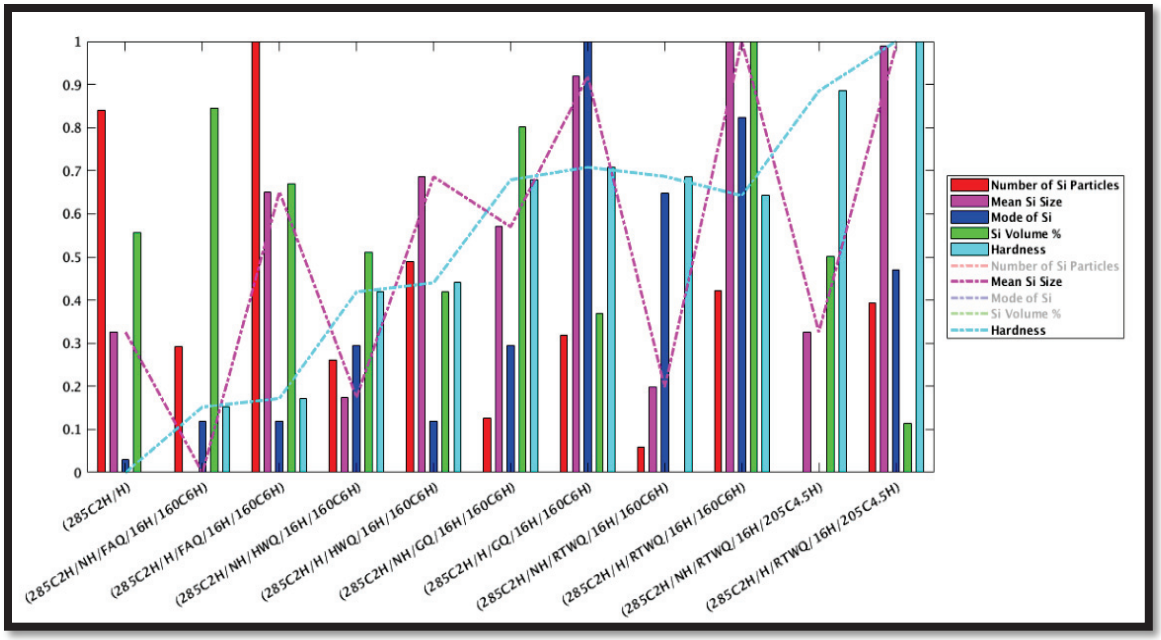


*Figure 73: Summary results of silicon particles with trend lines for mean particle size and hardness in all applicable post-processing conditions*

Figure 74 compares the precipitate size and spacing for all post processing conditions. The precipitate size and spacing is non-dimensionalized by the average diameter or average spacing, respectively. This sets one as the mean to which the probability density is graphed of either the diameter or interparticle spacing of all the post-processing conditions. The top of Figure 74 is the non-HIP samples, while the bottom of Figure 74 is the HIP samples. What can be noticed among both groups is that silicon particle size is non-normally distributed, while interparticle spacing is relatively normal in distribution. The silicon particle size trends towards normality as quench rate is increased in both groups and interparticle spacing has a lower variance in the HIP samples as compared the non-HIP samples. The conclusion that can be drawn from this data is that mechanical property increases are resultant from a homogeneous microstructure. That is to say, a microstructure

with a consistent (close to normally distributed) silicon particle size, and consistent (low variance) interparticle spacing.

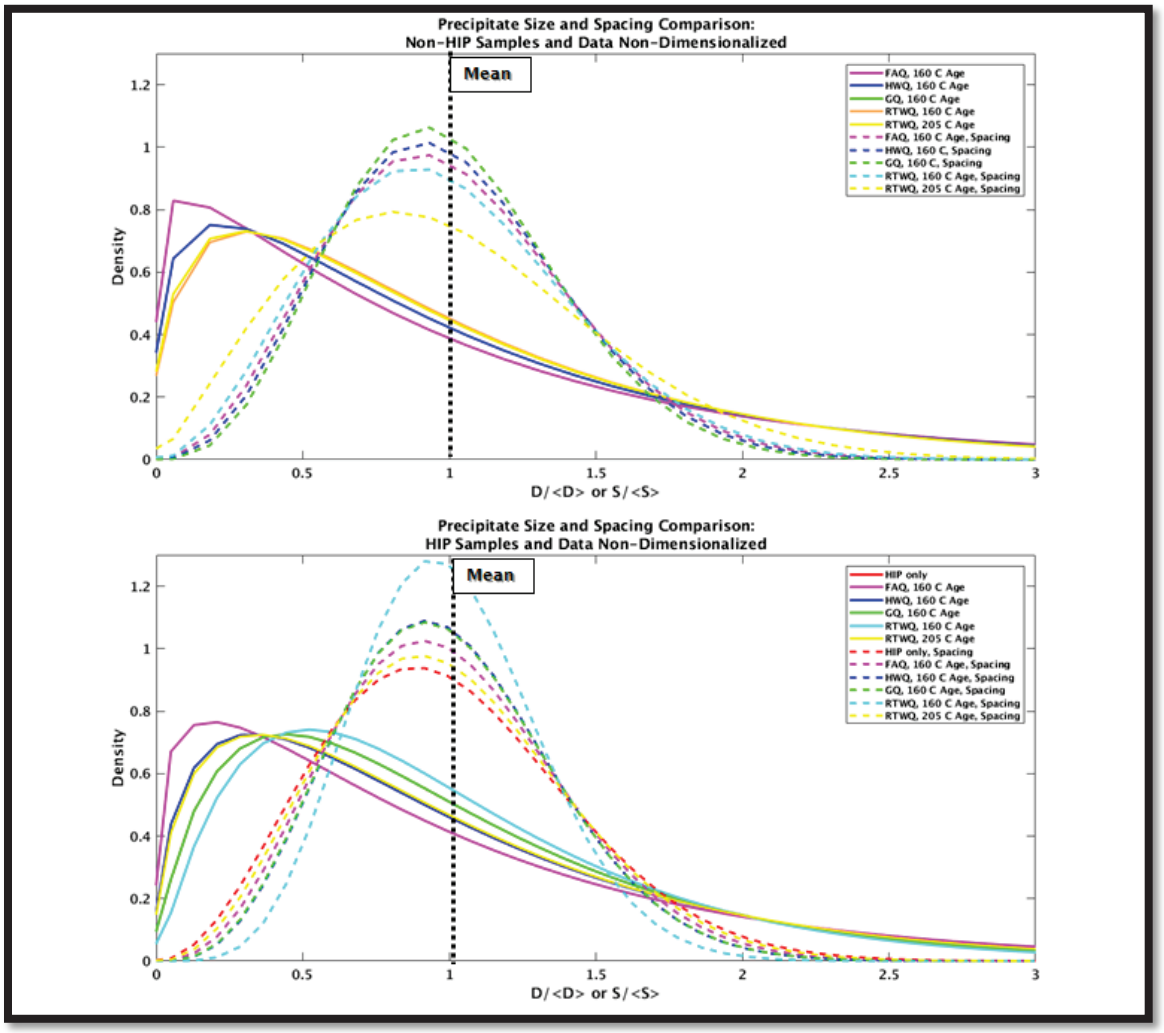


*Figure 74: Summary results of silicon particles size and interparticle spacing in all applicable post-processing conditions; (top) Non-HIP and (bottom) HIP*

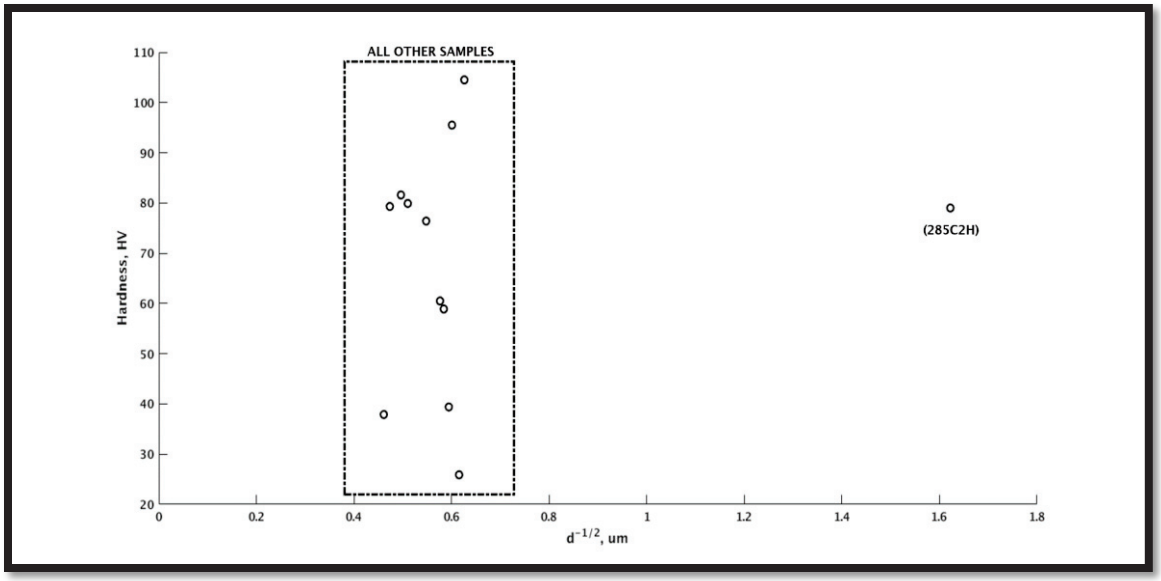


*Figure 75: Hall-Petch grain size versus Vickers Hardness*

The results of the grain size analysis are best captured by Figure 75, where the Hall-Petch diameter of the grains are plotted versus hardness. It can be concluded from this figure that grain size plays no significant role in mechanical properties when considering post-processed LPBF AlSi10Mg.

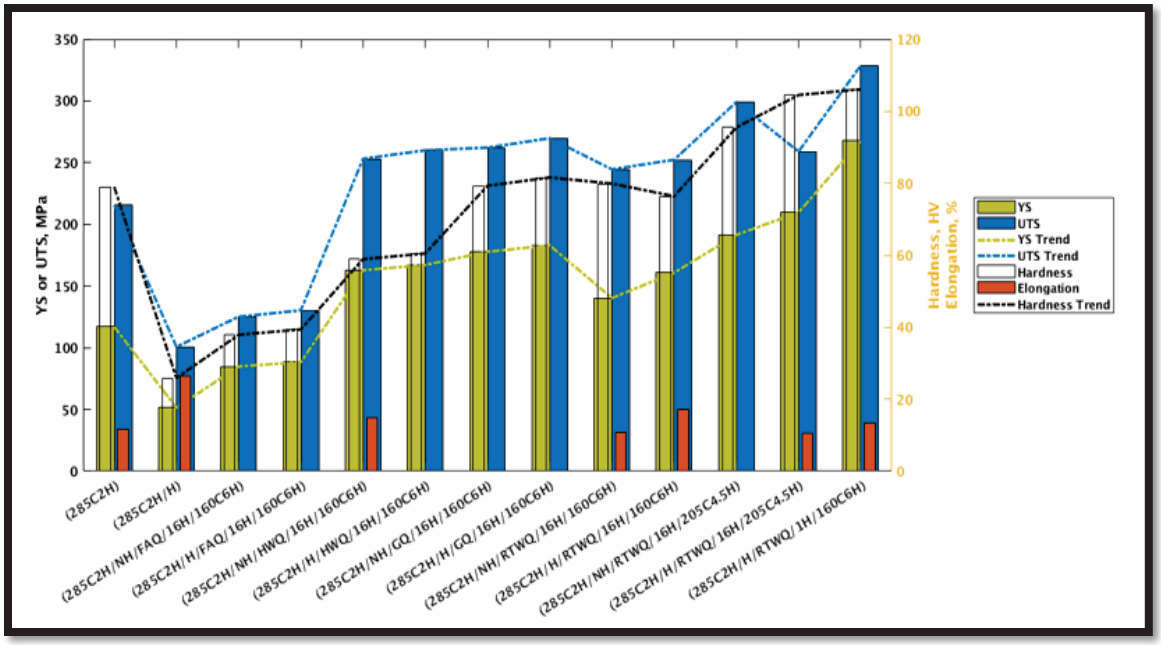


*Figure 76: Summary results of hardness, yield strength, ultimate strength, and elongation in all applicable post-processing conditions*

Figure 76 summarizes all the mechanical results gathered in this investigation. Trim lines are provided for hardness yield strength and ultimate tensile strength. Similar to the other results received, these properties also trend upward with increasing quench rate. Figure 77 is the cut the combined results from the age hardening study. This data suggests that the effect of hot isostatic pressing results in a time shift which serves to decrease the amount of time to reach peak hardness for a given artificial aging temperature.

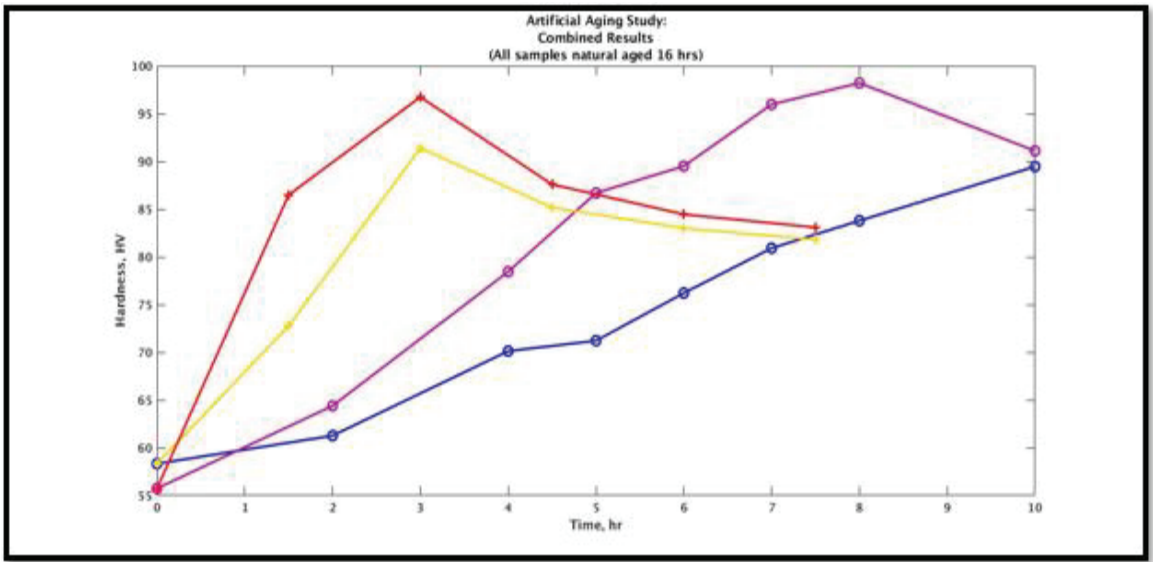


*Figure 77: Summary of age-hardening hardening results*

## *Discussion*

### *Correlation of Youngstown State to Oerlikon Post-processing Data*

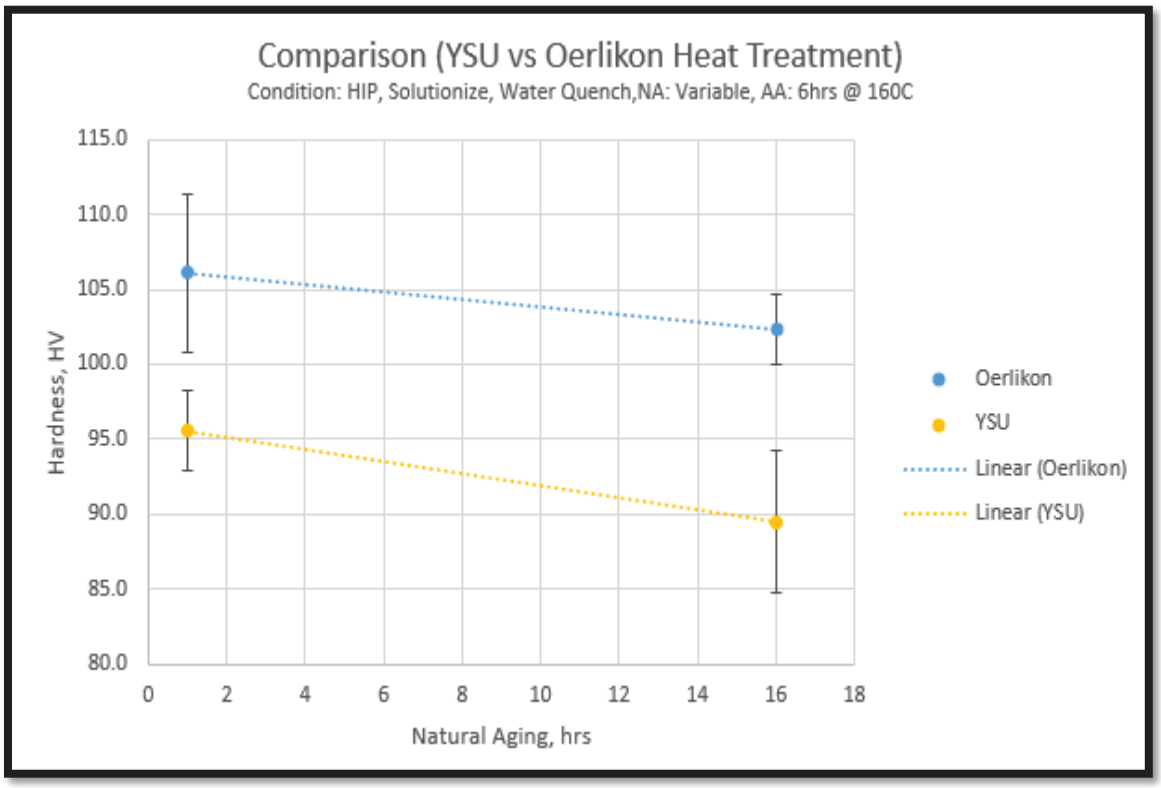


*Figure 78: Effect of natural age length of received hardness and comparison between Youngstown State (YSU) Oerlikon heat treatments*

Differences were discovered in the data received during post processing of AlSi10Mg samples. The differences depended on where the samples were processed. Youngstown State was responsible for the majority of heat treatments during this study, but Oerlikon, a partner on the project, was responsible for hot isostatic pressing of all samples that were scheduled for that process and a subset of samples that received a peak age, *T6*, as specified by ASTM F3318-18. That subset of samples were all uniaxial tensile testing samples following the designation (285C2H/H/530C6H/RTWQ/1H/160C6H). As reported in the results, those samples had significantly higher hardness, yield and ultimate strength as

compared to samples processed similarly by Youngstown State. The initial parameter thought responsible was the length of natural aging, as that differed between Youngstown State and Oerlikon. A subset experiment was devised to quantify the dynamics and possible differences between not only the length of natural aging but also the facility where the samples were processed. The test had both Youngstown State and Oerlikon process samples at one and 16 hour natural age lengths and then artificially aged the samples at *160℃* for *6* hours. Figure 78 shows the results of those experimental conditions. Apparent is the increase in hardness over both conditions with samples processed at Oerlikon. The most logical explanation for the increases is the industrialization of the heat treatment process by dedicated equipment and strict equipment controls at Oerlikon over the facilities available at Youngstown State. Youngstown State, while lacking dedicated heat treatment furnaces and equipment, can be agile and able to vary post processing parameters easily. This variation comes at the cost of roughly a *12%* reduction in mechanical properties. What cannot be gleaned from the data is the effect of the length of natural aging, as all data points are within the measurement error of the respective post processing location. From the data that is presently available, one can but surmise that the natural aging length has no effect on the final properties achieved through artificial aging.

## *Aging Model*

### Model Development

Having experimented and collected a substantial amount of data from various post processing conditions, a model was derived to describe the age hardening behavior of

LPBF AlSi10Mg. Models and or data have been reported by other authors (Rometsch and Schaffer 2002; Lumley, Polmear, and Curtis 2009; Aboulkhair et al. 2015; A. Mertens et al. 2015; Zhou et al. 2018). At present, models of age hardening in the Al-Si system have only been proposed with regards to traditionally produced castings, and generally all rely upon the sum of the individual components and/or processes. Considering that artificial aging is the last step of post-processing in precipitation hardening, a model describing that behavior would by necessity require thoughtful integration of the effects of all previous processing steps. These models can be quite complex and require a host of physical parameters in order to be derived by first principles. The model constructed by this author aims to pare down this requirement for the multitude of physical parameters by borrowing the kernel shared by most age hardening models and inserting it into an empirical model. The kernel shared by most first principles models is at their core the Gaussian function. Figure 79 shows the age hardening behavior observed and a graphical interpretation of how to mathematically describe the experimental data. The empirical model was derived from two Gaussian function stitched together piecewise, about the peak, in order to describe dynamics up to peak age and then a secondary Gaussian to describe the post peak behavior.

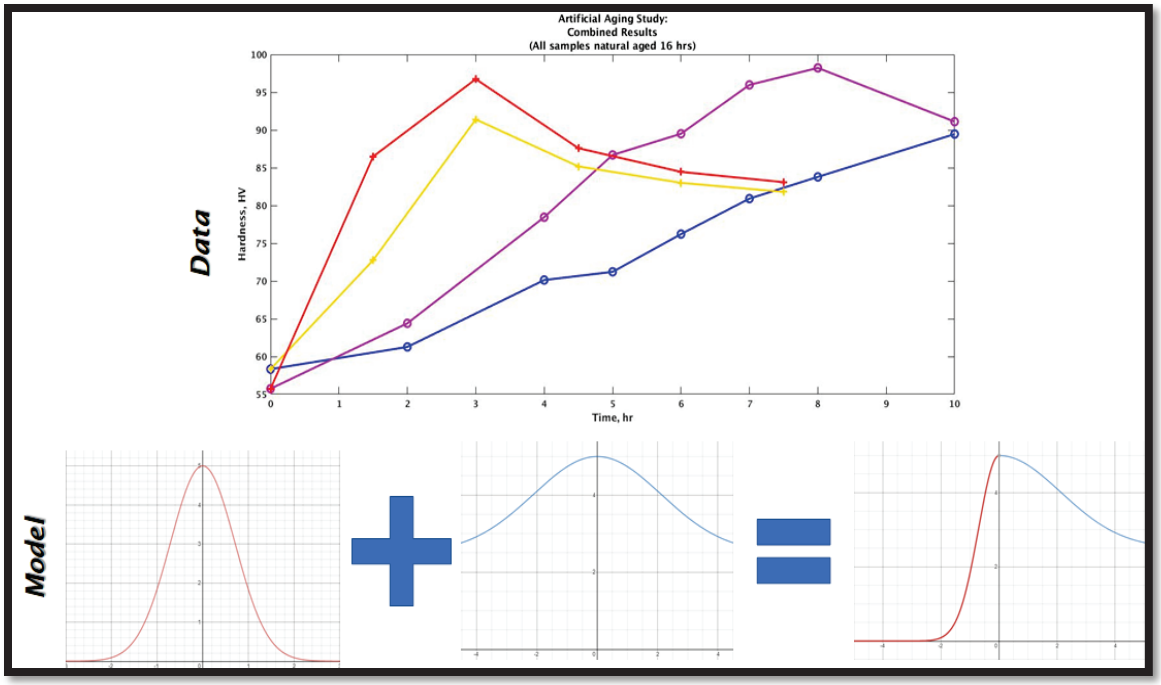


*Figure 79: Graphical argument detailing the construction of the age-hardening model*

The general model formulation (Equation IV) is a function of time (*hours*), temperature (°*C*), and the presence of HIPing (*H*) with the output in Vickers hardness (*HV*)

$$M(t,T,H) = \begin{cases} A_1(T)e^{-\left(\frac{(t-\tau H-\mu(T))}{\sigma_1(T)}\right)^2} + B_1(T), t \leq \mu \\ A_2(T)e^{-\left(\frac{(t-\tau H-\mu(T))}{\sigma_2(T)}\right)^2} + B_2(T), t > \mu \end{cases} \qquad \textit{(Equation IV)}$$

The HIPing parameter, *H*, is a binary, discrete variable that is switched on if hot isostatic pressing was performed, and zero otherwise. In time, and with more data, this variable can be given a more complicated definition, but presently, it was deemed more pragmatic to have it as a binary variable.

$$H = \begin{cases} 1, if\ HIP\ was\ performed \\ 0, otherwise \end{cases} \quad \textit{(Equation V)}$$

Letting $t=\mu$ and forcing the condition that $M(t,T,H)$ is equal at the intersection of the two regions enforces continuity of the end result.

$$M_{t\leq\mu}(\mu,T,H) = M_{t>\mu}(\mu,T,H) \quad \textit{(Equation VI)}$$

With a little rearranging $A_1(T,H)$ can be defined in terms of the other constants, and for brevity collect those terms into $\bar{A}(T,H)$. The last assumption of this model is to set $\sigma_1=\sigma_2$. σ, in general, controls the spread of the Gaussian. A large $\sigma$ results in a dilute Gaussian with heavier tails and a small $\sigma$ having a peaked Gaussian with thinner tails. Coupling the $\sigma_1=\sigma_2$ condition with the continuity condition gives a piecewise model that approximates a smooth, continuous single function. These assumptions and conditions also reduce the degrees of freedom in the model and thus reduces the experimental sample numbers required.

$$A_1(T,H) = A_2(T,H) + B_2(T,H) - B_1(T,H) \quad \textit{(Equation VII)}$$

$$Let\ \bar{A} = A_1(T,H)\ and\ \sigma_1 = \sigma_2 \quad \textit{(Equation VIII)}$$

$$M(t,T,H) = \begin{cases} \bar{A}(T)e^{-\left(\frac{(t-\tau H-\mu(T))}{\sigma(T)}\right)^2} + B_1(T), t \leq \mu \\ A_2(T)e^{-\left(\frac{(t-\tau H-\mu(T))}{\sigma(T)}\right)^2} + B_2(T), t > \mu \end{cases} \quad \textit{(Equation IX)}$$

(Equation IX) shows the finalized model used on the data in this study, and tested on limited literature data. This model assigns the effect of HIPing as a time shift in the kinetics of age hardening. This time shift was introduced after careful consideration of the specific experimental data received in this study and general trends seen in the literature. A trend seen in the literature is that while varying aging temperature peak hardness is invariant, up to any changes in the previous post-processing steps before artificial aging, with time to peak hardness being the variable of interest in this case. Another trend identified is the inconsistency in reported data with regard to the magnitude of the age hardenability. With regards to a model, this is the inconsistent spread of curves seen in the literature. Aboulkhair reports flat aging and Mertens also reports limited ranges in hardness throughout artificial aging (Aboulkhair et al. 2015; A. Mertens et al. 2015). Mechanistically, the development of the mechanical properties during precipitation hardening is attributed to nucleation and growth of coherent $Mg_2Si$ within the microstructure, however this dynamic is not something captured well by mathematical models in the literature. This dynamic results from previous steps in post-processing, but specifically the solutionization time and temperature, and the quench rate are the dominant factors. From the data gathered in this study, homogeneity in the microstructure prior to artificial aging seems to be a key factor in aiding in the development of the $Mg_2Si$. Also

quench rate controls the expulsion amount of silicon from solid solution which inherently effects $Mg_2Si$ formation. While only an empirical model, these effects are the constants $A_n$ and $B_n$ and with further experimentation trends could be developed.

## Modeling of these Data

Modeling of these data were accomplished by using the model developed and the curve fitting suite available in MatLab (Mathworks, USA). A protocol was created and followed to ensure consistent results on free parameters. The protocol is intimated in the following steps:

1. **Initialize on a non-HIP curve (*H=0*).**
2. **Limit all free parameters to be positive and set mu to maximum value in dataset.**
3. **Set solver to Robust-Bisquare and increase function evaluations and iterations to achieve convergence.**
4. **Run the solver.**
5. **Check that convergence was met, the fit quality, and that $B_1 \geq B_2$.**
6. **If all conditions are met, allow $\mu$ to vary and rerun the solver.**
7. **Once satisfied with results, record parameters.**
8. **Use parameters ($\mu$, $\sigma$) on HIP curve (*H=1*).**
9. **Solve for $\tau$.**

**10. Record parameters and report results.**

Figure 80, Figure 81, and Table 29 show the graphical and tabular results of fitting the model to the received data.

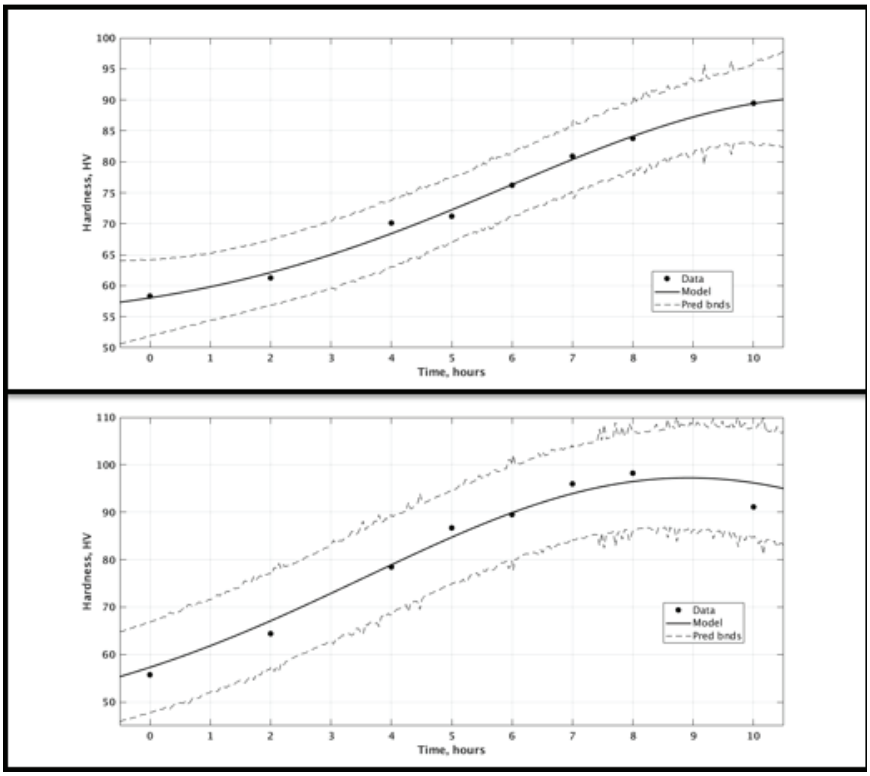


*Figure 80: (Top) Model fitted to (285C2H/NH/530C6H/RTWQ/16H/160CXH) data; (Bottom) Model fitted to (285C2H/H/530C6H/RTWQ/16H/160CXH) data*

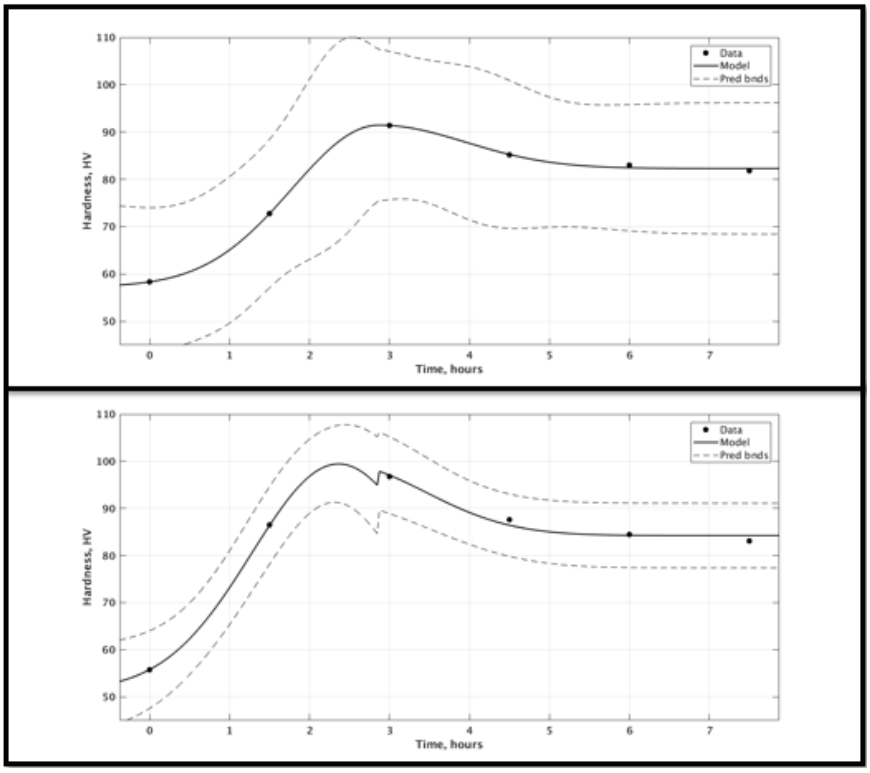


*Figure 81: (Top) Model fitted to (285C2H/NH/530C6H/RTWQ/16H/205CXH) data; (Bottom) Model fitted to (285C2H/H/530C6H/RTWQ/16H/205CXH) data*

*Table 29: Results from model fitting to data in indicated conditions*

| M(t,T,H) | $\mu$ | $\sigma$ | $\tau$ | $\bar{A}$ | $B_1$ | $A_2$ | $B_2$ | $R^2$ | Max Value |
|---|---|---|---|---|---|---|---|---|---|
| **M(t,160,0)** | 11.33 | 7.576 | 0 | 36.35 | 54.15 | 30.11 | 60.39 | .992 | 90.5 |
| **M(t,160,1)** | 11.33 | 7.576 | -2.4 | 52.95 | 44.0 | 27.31 | 69.94 | .963 | 96.95 |
| **M(t,205,0)** | 2.867 | 1.537 | 0 | 34.17 | 57.28 | 9.147 | 82.3 | .998 | 91.45 |
| **M(t,205,1)** | 2.867 | 1.537 | -.503 | 48.18 | 51.25 | 15.21 | 84.22 | .996 | 99.43 |

The results of fitting the model to the data indicate that the magnitude of the time shift in age hardening behavior with a *2.4* hour quickening at *160°C* and a *.5* hour quickening at *205°C* to peak hardness. Since the free parameters are tuned tune to the data set of this study, correlation was sought with data found in the literature and the proposed model. Published data (Zhou et al. 2018) was modeled with the results shown in Figure 82 and table ? and an agreement of *81%* between the two. Zhou's experimental methodology had their samples solutionized at a lower temperature and for less time. Because of those differences to the methodology of this study the parameters $A_n$ and $B_n$ were relaxed due to their high susceptibility to changes pre-artificial aging processing. However, $\mu$ and $\sigma$ were fixed to the values found previously with the data in this study.

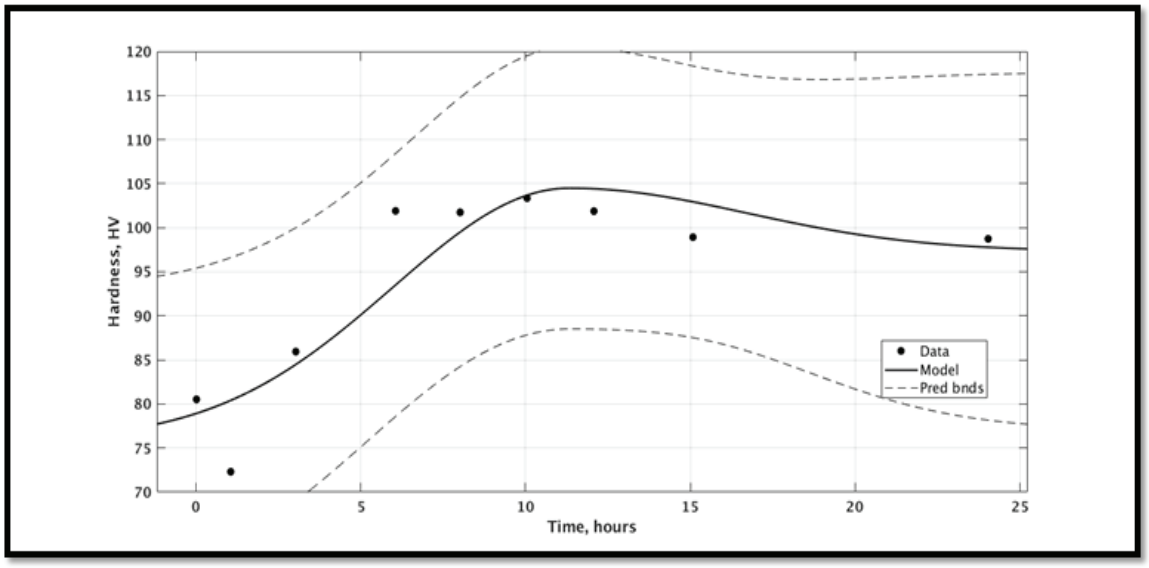


*Figure 82: Model fitted to Zhou* et al. *data*

*Table 30: Results from model fitting to Zhou* et al. *data*

| M(t,T,H) | $\mu$ | $\sigma$ | $\tau$ | $\bar{A}$ | $B_1$ | $A_2$ | $B_2$ | $R^2$ | Max Value |
|---|---|---|---|---|---|---|---|---|---|
| **M(t,160,0)** | 11.33 | 7.576 | 0 | 28.647 | 75.84 | 7.137 | 97.35 | .81 | 104.487 |

### Hardness, Yield Strength, and Ultimate Strength Versions of the Model

As a final measure, the model developed in this work was combined with the work of Cahoon and Tabor to generate material yield and ultimate strengths from hardness values. The equations are shown below. The strain hardening exponents required for those equations can be found in the results section of this document.

$$\sigma_{ys}(t,T,H) = g\left(\frac{M(t,T,H)}{3}\right)\left(\frac{1}{10}\right)^n \qquad \textit{(Equation X)}$$

$$\sigma_{uts}(t,T,H) = g\left(\frac{M(t,T,H)}{2.9}\right)\left(\frac{n}{.217}\right)^n \qquad \textit{(Equation XI)}$$

## *Process-Structure-Property: Kinetics of the LPBF AlSi10Mg System*

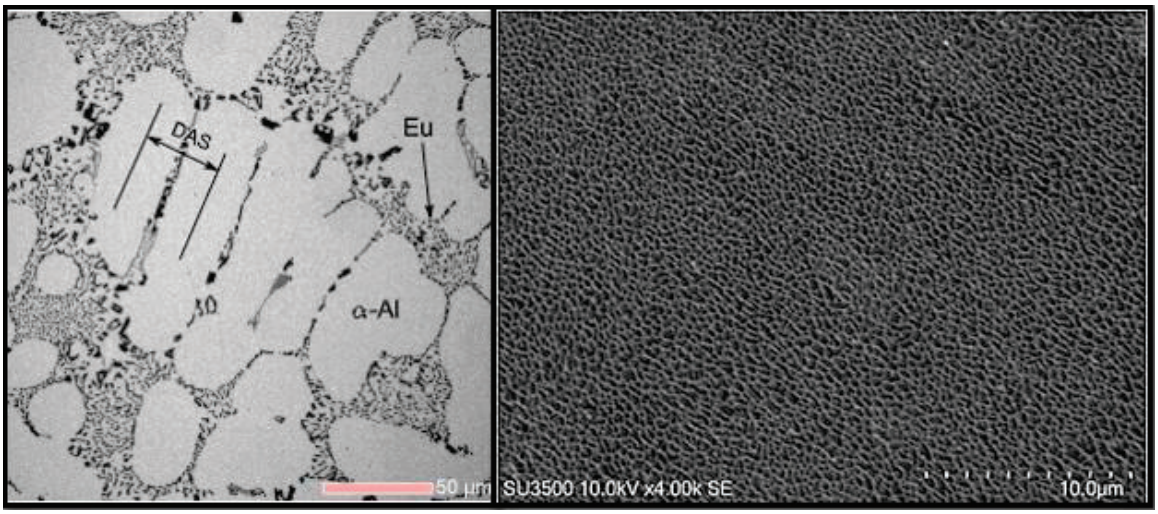


*Figure 83: Comparison of cast versus as-built LPBF microstructures in A356 and AlSi10Mg (Roy and Maijer 2014; Chou et al. 2017)*

The Process-Structure-Property relationship is a great notional model to consider the results received from LPBF AlSi10Mg. The experimental methodology follows a pragmatic doctrine and has been structured in a way to leverage what is known in traditional alloys in order to extend them to a new process, only introducing deviations where required. The process of casting versus LPBF, with the marked difference in solidification rates, produces very different microstructures. Both processing results are non-equilibrium thermodynamically, yet the laser powder bed fusion locks into the solid state a greater degree of that unsteady nature. From the context of mechanical properties, there are four constituents to account for (Equation XII): the intrinsic strength of the majority element, the solid solution contribution, the grain size (Hall-Petch) contribution, the precipitation hardening increases, and the debits due to defects. Analyzing this relationship and comparing between casting several terms drop out.

$$\sigma_{YS\ or\ UTS} = \sigma_{Al,i} + \sigma_{SS} + \sigma_{H-P} + \sigma_{precip} - \sigma_{defects} \quad \textit{(Equation XII)}$$

$$\sigma_{YS\ or\ UTS} = \cancel{\sigma_{Al,i}} + \sum_i k_i C_i^n + \cancel{\sigma_{H-P}} + \cancel{\sigma_{precip}} - \cancel{\sigma_{defects}} \quad \textit{(Equation XIII)}$$

If a comparison is made only between the solid solution strengthening apparent in both processes (Table 31 and (Equation XIII), it can be shown that LPBF has roughly a *110%* increase in properties due to the extended solubility of silicon versus a cast material. Typically, the contribution of concentration on solid solution strength has an exponent associated with it (*n=2/3*), but with the expressly defined contribution of alloying elements a non-exponentiated approach (*n=1*) was taken evaluating the solid solution strength.

*Table 31: Solid solution strengthening increases by alloying element (ASM International 1990)*

| Alloying Element | Yield Strength Increase (MPa/wt.%) | Ultimate Tensile Strength Increase (MPa/wt.%) |
|---|---|---|
| **Si** | 9.2 | 39.6 |
| **Mg** | 18.6 | 50.3 |
| **Cu** | 13.8 | 43.1 |
| **Mn** | 30.3 | 53.8 |
| **Zn** | 2.9 | 15.2 |

These two values are very illustrative of the non-equilibrium thermodynamics locked in by the two processes at solid state and a good metric when considering the results later received during post-processing. The chemistry of A356 is a little different, with a lower silicon weight percentage, than LPBF AlSi10Mg, but A356 is process post processed to peak hardness (*T6*) in a very similar manner to what is recommended for AlSi10Mg by standard. While compositionally near identical to LPBF AlSi10mg, A360 is typically used

in high pressure diecasting and subsequently post processing of this alloy is markedly different (Lumley). For this analysis, a comparison between cast A356-*T6* and LBPF AlSi10Mg-*T6* will be utilized to parse the differences in kinetics. From the standard (AMS 2771) A356 is solutionized at *540℃* for *6* hours and artificially aged at *155℃* for a range of *1-6* hours to reach the peak hardened condition (T6), while ASTM F3318 specifies that LPBF AlSi10Mg be solutionized for a minimum of *6* hours at *530°C* and subsequently artificially aged for a minimum of *6* hours at *160℃*. From the standards alone, it can be deduced that peak hardening occurs in AlSi10Mg at a longer time period than A356. This is supported by the data collected in this study, showing that that the closest equivalent condition (285C2H/NH/530C6H/X/160C6H) to cast A356 reaches peak hardness at approximately *11.3* hours. It then requires roughly twice as long of an artificial age in AlSi10Mg to achieve the same result as A356 which is also roughly the same order of magnitude difference in the solid solution strength of these two systems. Furthermore, the kinetics of AlSi10Mg are time shifted when hot isostatic pressing is included in the post processing. This increases the amount of above *500℃* thermal processing the alloy receives. The conclusion therefore is that the metric of solid solution strength, as built or as cast, is a measure of how much of the non-equilibrium composition of LPBF AlSi10Mg needs to be "undone" in order to equate the effects of post processing to that of A356.

In keeping with the adage that, "there is no such thing as a free lunch," the increases to strength in the as built condition due to the unique process comes with the additional time and energy expenditure if augmented properties are desired by utilizing the precipitation hardening capability within AlSi10Mg. This implies no bias towards one process over another only a recounting of what AlSi10Mg is in the context of A356/A360. Beyond the

novel microstructure imparted through the laser powder bed process, the material evolves through post processing like any of the other Al-Si-Mg casting alloys with strength levels primarily indicative of the formation of $Mg_2Si$.

## *Closing Remarks*

The figure below illustrates an effect which is prevalent in most of the microscopy presented in this document. That effect is the elliptic, or circular, morphology forming boundaries within the microstructure. As shown in the figure this morphology stems from melt pool boundaries which are inherent to the process of LPBF. However, it is unknown why these melt pool boundaries persist through post-processing. It can be speculated that the extreme solidification rates and/or boundary remelting may be causing micro-segregation between the aluminum and other alloying elements. Also, another prevalent thought is that oxides along the melt pool boundary are forming a diffusion barrier which is the cause for that morphology to remain through post-processing. At this time, it is unclear what is the exact mechanism for this persistent morphology and would be the basis for continued research.

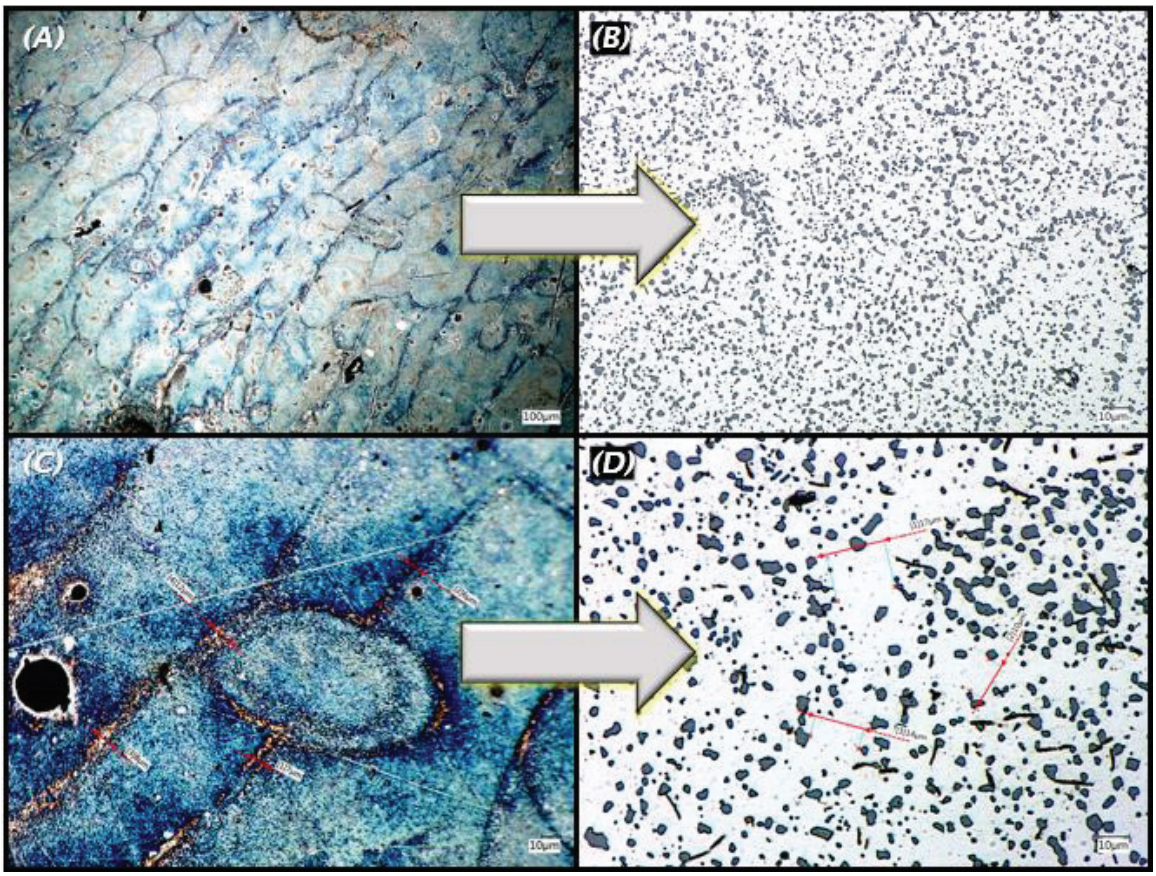


*Figure 84: Melt pool boundaries in stress relieved samples and their retention through post-processing*

Another area to extend the work done here is with further development of the age-hardening model. This could include further characterization of the artificial aging process, or the inclusion of previous post-processing steps. Further characterization of the artificial aging process would allow for different functional relationships (currently linear) on the free parameters to be employed. These place bounds on the parameters within a space which physically allowable phenomena. Inclusion of previous post-processing steps within the model allows for significantly more cross comparison with data found in the literature. The model presented here has limited applicability when incorporating literature data, due to the significant effects of stress relieving, solutionizing, and quenching on the properties at arrival to artificial aging. This is not to downplay the predictive power of the

model, especially when following the post-processing schedule described in this work, but to state its limitations and therefore to describe how it can be improved.

In closing, this work has served to significantly characterize the effects of post-processing heat treatment of AlSi10Mg to include HIP followed by precipitation hardening heat treatments, where, in particular, HIP has been shown to accelerate artificial aging. The final specification recommended from this research, as a replacement for components traditionally cast in A356, is (285C2H/H/530C6H/RTWQ/1-4H/160C8H).

## *Presentations Related to this Research*

Michael Juhasz, Will Bevan, Jared Clark, Jason Walker, and Brett Conner. "Post-processing Heat Treatments and Residual Stress Behavior of AlSi10Mg." Presentation. 2019 Annual International Solid Freeform Fabrication Symposium (SFF Symp 2019), Session: Materials: Metals IV - Aluminum Alloys. August 2019

Michael Juhasz, Jared Clark, William Bevin, Jason Walker, and Brett Conner. "Post-processing Heat Treatments and Residual Stress Behavior of AlSi10Mg." Presentation. Materials Science & Technology 2019, Symposium: Additive Manufacturing of Metals: Post Processing. October 2019.

## *References*


Aboulkhair, Nesma T., Ian Maskery, Chris Tuck, Ian Ashcroft, and Nicola M. Everitt. 2016. "The Microstructure and Mechanical Properties of Selectively Laser Melted AlSi10Mg: The Effect of a Conventional T6-like Heat Treatment." *Materials Science and Engineering: A* 667 (June): 139–46.

Aboulkhair, Nesma T., Chris Tuck, Ian Ashcroft, Ian Maskery, and Nicola M. Everitt. 2015. "On the Precipitation Hardening of Selective Laser Melted AlSi10Mg." *Metallurgical and Materials Transactions A* 46 (8): 3337–41.

Alkhair, Almabrouk Mousa. 2016. "Experimental Investigations of Curling Phenomenon in Selective Laser Sintering Process." *Rapid Prototyping Journal* 22 (2): 405–15.

"AMS2771F: Heat Treatment of Aluminum Alloy Castings - SAE International." n.d. Accessed November 6, 2019. https://www.sae.org/standards/content/ams2771f/.

Anderson, I. E., R. S. Figliola, and H. Morton. 1991. "Flow Mechanisms in High Pressure Gas Atomization." *Materials Science and Engineering: A* 148 (1): 101–14.

Asensio-Lozano, By: Juan, and George Vander Voort. n.d. "The Al-Si Phase Diagram."

https://www.buehler.com/solutions/technotes/vol5issue1.pdf.
ASM International, ed. 1990. *ASM Handbook*. 10th ed. Materials Park, OH: ASM International.
"ASTM F3318 - 18 Standard for Additive Manufacturing – Finished Part Properties – Specification for AlSi10Mg with Powder Bed Fusion – Laser Beam." n.d. Accessed November 6, 2019. https://www.astm.org/Standards/F3318.htm.
Astm, I. 2016. "ASTM E8/E8M-16a: Standard Test Methods for Tension Testing of Metallic Materials." *West Conshohocken, PA, USA: ASTM International*.
Astm, Iso. 2015. "ASTM52900-15 Standard Terminology for Additive Manufacturing—General Principles—Terminology." *ASTM International, West Conshohocken, PA*.
Barrett, Christopher, Carolyn Carradero, Evan Harris, Kirk Rogers, Eric MacDonald, and Brett Conner. 2019. "Statistical Analysis of Spatter Velocity with High-Speed Stereovision in Laser Powder Bed Fusion." *Progress in Additive Manufacturing* 4 (4): 423–30.
Baumers, M., C. Tuck, and R. Hague. 2015. "Selective Heat Sintering versus Laser Sintering: Comparison of Deposition Rate, Process Energy Consumption and Cost Performance." In *Solid Freeform Fabrication Symposium*. sffsymposium.engr.utexas.edu. https://sffsymposium.engr.utexas.edu/sites/default/files/2015/2015-9-Baumers.pdf.
Beretta, S., and S. Romano. 2017. "A Comparison of Fatigue Strength Sensitivity to Defects for Materials Manufactured by AM or Traditional Processes." *International Journal of Fatigue* 94 (January): 178–91.
Bourdeau, Romeo G. 1983. Rotary atomizing process. USPTO 4415511. *US Patent*, filed December 27, 1982, and issued November 15, 1983. https://patentimages.storage.googleapis.com/b1/bf/fd/64e4821befd6c9/US4415511.pdf.
Bourell, David L., Harris L. Marcus, Joel W. Barlow, Joseph J. Beaman, and Carl R. Deckard. 1990. Multiple material systems for selective beam sintering. USPTO 4944817. *US Patent*, filed September 5, 1989, and issued July 31, 1990. https://patentimages.storage.googleapis.com/ab/34/d3/81b54818650723/US4944817.pdf.
Brandl, Erhard, Ulrike Heckenberger, Vitus Holzinger, and Damien Buchbinder. 2012. "Additive Manufactured AlSi10Mg Samples Using Selective Laser Melting (SLM): Microstructure, High Cycle Fatigue, and Fracture Behavior." *Materials & Design* 34 (February): 159–69.
Braszczyński, Janusz, and Andrzej Zyska. 2000. "Analysis of the Influence of Ceramic Particles on the Solidification Process of Metal Matrix Composites." *Materials Science and Engineering: A* 278 (1): 195–203.
Buchbinder, D., and W. Meiners. 2010. "Generative Fertigung von Aluminiumbauteilen Für Die Serienproduktion." *AluGenerativ Abschlussbericht BMBF 01RIO639A-D*.
Cahoon, J. R. 1972. "An Improved Equation Relating Hardness to Ultimate Strength." *Metallurgical and Materials Transactions B* 3 (11): 3040–3040.
Cahoon, J. R., W. H. Broughton, and A. R. Kutzak. 1971. "The Determination of Yield Strength from Hardness Measurements." *Metallurgical Transactions* 2 (7): 1979–83.
Candel-Ruiz, Antonio, Sebastian Kaufmann, and Oliver Müllerschön. 2015. "Strategies for High Deposition Rate Additive Manufacturing by Laser Metal Deposition."

*Proceedings of Lasers in Manufacturing (LiM)*, 584–610.
Chen, B., S. K. Moon, X. Yao, G. Bi, J. Shen, J. Umeda, and K. Kondoh. 2017. "Strength and Strain Hardening of a Selective Laser Melted AlSi10Mg Alloy." *Scripta Materialia* 141 (December): 45–49.
Chou, R., A. Ghosh, S. C. Chou, M. Paliwal, and M. Brochu. 2017. "Microstructure and Mechanical Properties of Al10SiMg Fabricated by Pulsed Laser Powder Bed Fusion." *Materials Science and Engineering: A* 689 (March): 53–62.
Conner, Brett P., Guha P. Manogharan, Ashley N. Martof, Lauren M. Rodomsky, Caitlyn M. Rodomsky, Dakesha C. Jordan, and James W. Limperos. 2014. "Making Sense of 3-D Printing: Creating a Map of Additive Manufacturing Products and Services." *Additive Manufacturing* 1-4 (October): 64–76.
Criales, Luis E., Yiğit M. Arısoy, Brandon Lane, Shawn Moylan, Alkan Donmez, and Tuğrul Özel. 2017. "Laser Powder Bed Fusion of Nickel Alloy 625: Experimental Investigations of Effects of Process Parameters on Melt Pool Size and Shape with Spatter Analysis." *International Journal of Machine Tools & Manufacture* 121 (October): 22–36.
Croucher, T. 1982. "Quenching of Aluminum Alloys: What This Key Step Accomplishes." *Heat Treating Progress* 14 (5): 20–21.
Croucher, Tom. 2009. "Minimizing Machining Distortion in Aluminum Alloys through Successful Application of Uphill Quenching—a Process Overview." *Journal of ASTM International* 6 (7): 1–14.
Cunningham, Ross, Sneha P. Narra, Colt Montgomery, Jack Beuth, and A. D. Rollett. 2017. "Synchrotron-Based X-Ray Microtomography Characterization of the Effect of Processing Variables on Porosity Formation in Laser Powder-Bed Additive Manufacturing of Ti-6Al-4V." *JOM Journal of the Minerals Metals and Materials Society* 69 (3): 479–84.
Cunningham, Ross, Cang Zhao, Niranjan Parab, Christopher Kantzos, Joseph Pauza, Kamel Fezzaa, Tao Sun, and Anthony D. Rollett. 2019. "Keyhole Threshold and Morphology in Laser Melting Revealed by Ultrahigh-Speed X-Ray Imaging." *Science* 363 (6429): 849–52.
Deckard, Carl R. 1989. Method and apparatus for producing parts by selective sintering. USPTO 4863538. *US Patent*, filed October 17, 1986, and issued September 5, 1989. https://patentimages.storage.googleapis.com/d2/84/74/eaf2b3d455fe5e/US4863538.pdf.
Edwards, G. A., K. Stiller, G. L. Dunlop, and M. J. Couper. 1998. "The Precipitation Sequence in Al–Mg–Si Alloys." *Acta Materialia* 46 (11): 3893–3904.
Elmer, J., P. Hochanadel, K. Lachenberg, and T. Webber. 2009. "Introduction to High Energy Density Electron and Laser Beam Welding." Lawrence Livermore National Lab.(LLNL), Livermore, CA (United States). https://www.osti.gov/servlets/purl/1213660.
Entezarian, M., F. Allaire, P. Tsantrizos, and R. A. L. Drew. 1996. "Plasma Atomization: A New Process for the Production of Fine, Spherical Powders." *JOM Journal of the Minerals Metals and Materials Society* 48 (6): 53–55.
"EOS Metal Materials for Additive Manufacturing." n.d. Accessed November 6, 2019. https://www.eos.info/material-m.
Fiocchi, J., A. Tuissi, P. Bassani, and C. A. Biffi. 2017. "Low Temperature Annealing

Dedicated to AlSi10Mg Selective Laser Melting Products." *Journal of Alloys and Compounds* 695 (February): 3402–9.
Foster, B., E. Reutzel, A. Nassar, B. Hall, S. Brown, and C. Dickman. 2015. "Optical, Layerwise Monitoring of Powder Bed Fusion." In *Solid Freeform Fabrication Symposium, Austin, TX, Aug*, 10–12. sffsymposium.engr.utexas.edu.
Frazier, William E. 2014. "Metal Additive Manufacturing: A Review." *Journal of Materials Engineering and Performance* 23 (6): 1917–28.
Fulcher, Benjamin A., David K. Leigh, and Trevor J. Watt. 2014. "Comparison of AlSi10Mg and Al 6061 Processed through DMLS." In *Proceedings of the Solid Freeform Fabrication (SFF) Symposium, Austin, TX, USA*. Vol. 46. pdfs.semanticscholar.org. https://pdfs.semanticscholar.org/536b/53a6b3e80579cbe3419bd99b266cf2561256.pdf.
Gao, Li, Yohei Harada, and Shinji Kumai. 2015. "Microstructural Characterization of Aluminum Alloys Using Weck's Reagent, Part I: Applications." *Materials Characterization* 107 (September): 426–33.
Geyer, Frank. 2016. "Powder Based Additive Manufacturing Methods LMF/LMD--Requirements, Comparison and Applications." In *International Congress on Applications of Lasers & Electro-Optics*, 2016:701. LIA.
Gockel, Joy, Jack Beuth, and Karen Taminger. 2014. "Integrated Control of Solidification Microstructure and Melt Pool Dimensions in Electron Beam Wire Feed Additive Manufacturing of Ti-6Al-4V." *Additive Manufacturing* 1-4 (October): 119–26.
Gong, Xibing, Ted Anderson, and Kevin Chou. 2014. "Review on Powder-Based Electron Beam Additive Manufacturing Technology." *Manufacturing Review* 1: 2.
Gu, D. D., W. Meiners, K. Wissenbach, and R. Poprawe. 2012. "Laser Additive Manufacturing of Metallic Components: Materials, Processes and Mechanisms." *International Materials Reviews* 57 (3): 133–64.
Hadadzadeh, Amir, Babak Shalchi Amirkhiz, Akindele Odeshi, Jian Li, and Mohsen Mohammadi. 2019. "Role of Hierarchical Microstructure of Additively Manufactured AlSi10Mg on Dynamic Loading Behavior." *Additive Manufacturing* 28 (August): 1–13.
Hansen, Max, Kurt Anderko, and H. W. Salzberg. 1958. "Constitution of Binary Alloys." *Journal of the Electrochemical Society* 105 (12): 260C – 261C.
Heinl, P., A. Rottmair, C. Körner, and R. F. Singer. 2007. "Cellular Titanium by Selective Electron Beam Melting." *Advanced Engineering Materials* 9 (5): 360–64.
Hopkinson, Neil, and Poonjolai Erasenthiran. 2004. "High Speed Sintering-Early Research into a New Rapid Manufacturing Process." In *Solid Freeform Fabrication Symposium*, 312–20.
Kahnert, M., S. Lutzmann, and M. F. Zaeh. 2007. "Layer Formations in Electron Beam Sintering." In *Solid Freeform Fabrication Symposium*, 88–99. pdfs.semanticscholar.org.
Kempen, K., L. Thijs, J. Van Humbeeck, and J-P Kruth. 2012. "Mechanical Properties of AlSi10Mg Produced by Selective Laser Melting." *Physics Procedia* 39 (January): 439–46.
. 2015. "Processing AlSi10Mg by Selective Laser Melting: Parameter Optimization

and Material Characterization." *Materials Science and Technology* 31 (8): 917–23.
Khairallah, Saad A., Andrew T. Anderson, Alexander Rubenchik, and Wayne E. King. 2016. "Laser Powder-Bed Fusion Additive Manufacturing: Physics of Complex Melt Flow and Formation Mechanisms of Pores, Spatter, and Denudation Zones." *Acta Materialia* 108 (April): 36–45.
Kimura, Takahiro, and Takayuki Nakamoto. 2016. "Microstructures and Mechanical Properties of A356 (AlSi7Mg0.3) Aluminum Alloy Fabricated by Selective Laser Melting." *Materials & Design* 89 (January): 1294–1301.
King, Wayne E., Holly D. Barth, Victor M. Castillo, Gilbert F. Gallegos, John W. Gibbs, Douglas E. Hahn, Chandrika Kamath, and Alexander M. Rubenchik. 2014. "Observation of Keyhole-Mode Laser Melting in Laser Powder-Bed Fusion Additive Manufacturing." *Journal of Materials Processing Technology* 214 (12): 2915–25.
Kleszczynski, Stefan, J. Zur Jacobsmühlen, J. Sehrt, and G. Witt. 2012. "Error Detection in Laser Beam Melting Systems by High Resolution Imaging." In *Proceedings of the Solid Freeform Fabrication Symposium*. Vol. 2012. researchgate.net. https://www.researchgate.net/profile/Stefan_Kleszczynski/publication/279622279_Error_detection_in_laser_beam_melting_systems_by_high_resolution_imaging/links/5742bf8b08ae298602ee540a.pdf.
Kruth, J-P, G. Levy, F. Klocke, and T. H. C. Childs. 2007. "Consolidation Phenomena in Laser and Powder-Bed Based Layered Manufacturing." *CIRP Annals* 56 (2): 730–59.
Lewandowski, John J., and Mohsen Seifi. 2016. "Metal Additive Manufacturing: A Review of Mechanical Properties." *Annual Review of Materials Research* 46 (1): 151–86.
Liu, Bochuan, Ricky Wildman, Christopher Tuck, Ian Ashcroft, and Richard Hague. 2011. "Investigation the Effect of Particle Size Distribution on Processing Parameters Optimization in Selective Laser Melting Process." *Additive Manufacturing Research Group, Loughborough University*, 227–38.
Liu, Yang, Yongqiang Yang, Shuzhen Mai, Di Wang, and Changhui Song. 2015. "Investigation into Spatter Behavior during Selective Laser Melting of AISI 316L Stainless Steel Powder." *Materials & Design* 87 (December): 797–806.
Lumley, R. N., I. J. Polmear, and P. R. Curtis. 2009. "Rapid Heat Treatment of Aluminum High-Pressure Diecastings." *Metallurgical and Materials*. https://idp.springer.com/authorize/casa?redirect_uri=https://link.springer.com/article/10.1007/s11661-009-9836-y&casa_token=Rt0FO3B3uvIAAAAA:GslkasQy-U11QvSF57kbHB1VDa39wjUM52QZupLW4mOx-lUGWr50_ovN8xB2piOSyp6ux148dPZpKTy0bA.
Ly, Sonny, Alexander M. Rubenchik, Saad A. Khairallah, Gabe Guss, and Manyalibo J. Matthews. 2017. "Metal Vapor Micro-Jet Controls Material Redistribution in Laser Powder Bed Fusion Additive Manufacturing." *Scientific Reports* 7 (1): 4085.
Manfredi, D., E. P. Ambrosio, and F. Calignano. n.d. "Direct Metal Laser Sintering: An Additive Manufacturing Technology Ready to Produce Lightweight Structural Parts for Robotic Applications." *La Metallurgia*. https://www.gruppofrattura.it/ors/index.php/aim/article/viewFile/1210/1163.
Manfredi, Diego, Flaviana Calignano, Manickavasagam Krishnan, Riccardo Canali, Elisa Paola Ambrosio, and Eleonora Atzeni. 2013. "From Powders to Dense Metal Parts:

Characterization of a Commercial AlSiMg Alloy Processed through Direct Metal Laser Sintering." *Materials* 6 (3): 856–69.
Ma, Pan, Konda G. Prashanth, Sergio Scudino, Yandong Jia, Hongwei Wang, Chunming Zou, Zunjie Wei, and Jürgen Eckert. 2014. "Influence of Annealing on Mechanical Properties of Al-20Si Processed by Selective Laser Melting." *Metals* 4 (1): 28–36.
Marola, Silvia, Diego Manfredi, Gianluca Fiore, Marco Gabriele Poletti, Mariangela Lombardi, Paolo Fino, and Livio Battezzati. 2018. "A Comparison of Selective Laser Melting with Bulk Rapid Solidification of AlSi10Mg Alloy." *Journal of Alloys and Compounds* 742 (April): 271–79.
Maskery, I., N. T. Aboulkhair, C. Tuck, R. D. Wildman, I. A. Ashcroft, N. M. Everitt, and R. J. M. Hague. 2015. "Fatigue Performance Enhancement of Selectively Laser Melted Aluminium Alloy by Heat Treatment." In *26th Annual International Solid Freeform Fabrication Symposium, Austin, Texas, USA*, 1017–25. researchgate.net.
Mertens, A. I., and J. Delahaye. 2017. "Fusion-Based Additive Manufacturing for Processing Aluminum Alloys: State-of-the-Art and Challenges." *Advanced Engineering Materials*. https://onlinelibrary.wiley.com/doi/abs/10.1002/adem.201700003?casa_token=0RbiSEXSUvcAAAAA:DT7fd_nMa2k1nMF60KyDkK8hTqbJ3eWG3bgYR52DmZjQWG4LHOhMHHg32bmkZkoqM7RUnA6vtlfuhz16.
Mertens, Anne, Olivier Dedry, David Reuter, Olivier Rigo, and Jacqueline Lecomte-Beckers. 2015. "Thermal Treatments of AlSi10Mg Processed by Laser Beam Melting." In *Proceedings of the 26th International Solid Freeform Fabrication Symposium*, 1007–16. Austin.
Mohammadtaheri, M. 2012. "A New Metallographic Technique for Revealing Grain Boundaries in Aluminum Alloys." *Metallography, Microstructure, and Analysis* 1 (5): 224–26.
Möller, H., G. Govender, and W. E. Stumpf. 2007. "Natural and Artificial Aging Response of Semisolid Metal Processed Al–Si–Mg Alloy A356." *International Journal of Cast Metals Research* 20 (6): 340–46.
Moustafa, M. A., F. H. Samuel, and H. W. Doty. 2003. "Effect of Solution Heat Treatment and Additives on the Microstructure of Al-Si (A413.1) Automotive Alloys." *Journal of Materials Science* 38 (22): 4507–22.
Murayama, M., and K. Hono. 1999. "Pre-Precipitate Clusters and Precipitation Processes in Al–Mg–Si Alloys." *Acta Materialia* 47 (5): 1537–48.
Murayama, M., K. Hono, M. Saga, and M. Kikuchi. 1998. "Atom Probe Studies on the Early Stages of Precipitation in Al–Mg–Si Alloys." *Materials Science and Engineering: A* 250 (1): 127–32.
Murray, J. L., and A. J. McAlister. 1984. "The Al-Si (Aluminum-Silicon) System." *Bulletin of Alloy Phase Diagrams* 5 (1): 74.
Myers, Kyle M. 2016. "Structure-Property Relationship of Binder Jetted Fused Silica Preforms to Manufacture Ceramic-Metallic Interpenetrating Phase Composites." Youngstown State University. http://rave.ohiolink.edu/etdc/view?acc_num=ysu1464089607.
Myhr, O. R., Ø. Grong, and S. J. Andersen. 2001. "Modelling of the Age Hardening Behaviour of Al–Mg–Si Alloys." *Acta Materialia* 49 (1): 65–75.
Nauka, Krzysztof, Vladek Kasperchik, and Aja Hartman. 2019. Finishing a 3d printed

object. USPTO 20190030803:A1. *US Patent*, filed May 5, 2016, and issued January 31, 2019. https://patentimages.storage.googleapis.com/56/3f/40/8faaa3dc4163e9/US20190030803A1.pdf.

Oberhofer, Johann, Joachim Göbner, and Hans-Ulrich Büse. 2014. Method and device for manufacturing a three-dimensional object that is suitable for application to microtechnology. USPTO 8784720. *US Patent*, filed February 22, 2011, and issued July 22, 2014. https://patentimages.storage.googleapis.com/82/2d/90/bc7aaa6423ba38/US8784720.pdf.

Orowan, E. 1948. "Internal Stress in Metals and Alloys." *The Institute of Metals, London* 451.

Parry, L., I. A. Ashcroft, and R. D. Wildman. 2016. "Understanding the Effect of Laser Scan Strategy on Residual Stress in Selective Laser Melting through Thermo-Mechanical Simulation." *Additive Manufacturing* 12 (October): 1–15.

Persson, F., A. Eliasson, and P. Jönsson. 2012. "Prediction of Particle Size for Water Atomised Metal Powders: Parameter Study." *Powder Metallurgy* 55 (1): 45–53.

"Powder Bed Fusion | Additive Manufacturing Research Group | Loughborough University." n.d. Accessed December 17, 2019. https://www.lboro.ac.uk/research/amrg/about/the7categoriesofadditivemanufacturing/powderbedfusion/.

Prashanth, K. G., S. Scudino, H. J. Klauss, K. B. Surreddi, L. Löber, Z. Wang, A. K. Chaubey, U. Kühn, and J. Eckert. 2014. "Microstructure and Mechanical Properties of Al–12Si Produced by Selective Laser Melting: Effect of Heat Treatment." *Materials Science and Engineering: A* 590 (January): 153–60.

Rao, Suraj, Ross Cunningham, Tugce Ozturk, and Anthony D. Rollett. 2016. "Measurement and Analysis of Porosity in Al-10Si-1Mg Components Additively Manufactured by Selective Laser Melting." *Materials Performance and Characterization* 5 (5): 701–16.

Read, Noriko, Wei Wang, Khamis Essa, and Moataz M. Attallah. 2015. "Selective Laser Melting of AlSi10Mg Alloy: Process Optimisation and Mechanical Properties Development." *Materials & Design* 65 (January): 417–24.

Romano, S., A. Brückner-Foit, A. Brandão, J. Gumpinger, T. Ghidini, and S. Beretta. 2018. "Fatigue Properties of AlSi10Mg Obtained by Additive Manufacturing: Defect-Based Modelling and Prediction of Fatigue Strength." *Engineering Fracture Mechanics* 187 (January): 165–89.

Rometsch, P. A., and G. B. Schaffer. 2002. "An Age Hardening Model for Al–7Si–Mg Casting Alloys." *Materials Science and Engineering: A* 325 (1): 424–34.

Rosenthal, Idan, Adin Stern, and Nachum Frage. 2014. "Microstructure and Mechanical Properties of AlSi10Mg Parts Produced by the Laser Beam Additive Manufacturing (AM) Technology." *Metallography, Microstructure, and Analysis* 3 (6): 448–53.

Rosenthal, I., A. Stern, and N. Frage. 2017. "Strain Rate Sensitivity and Fracture Mechanism of AlSi10Mg Parts Produced by Selective Laser Melting." *Materials Science and Engineering: A* 682 (January): 509–17.

Roy, M. J., and D. M. Maijer. 2014. "Response of A356 to Warm Rotary Forming and Subsequent T6 Heat Treatment." *Materials Science and Engineering: A* 611

(August): 223–33.
Sames, W. J., F. A. List, S. Pannala, R. R. Dehoff, and S. S. Babu. 2016. "The Metallurgy and Processing Science of Metal Additive Manufacturing." *International Materials Reviews* 61 (5): 315–60.
Sames, W. J., F. Medina, W. H. Peter, S. S. Babu, and R. R. Dehoff. 2014. "Effect of Process Control and Powder Quality on Inconel 718 Produced Using Electron Beam Melting." In *8th Int. Symp. Superalloy 718 Deriv*, 409–23. books.google.com.
Santomaso, A., P. Lazzaro, and P. Canu. 2003. "Powder Flowability and Density Ratios: The Impact of Granules Packing." *Chemical Engineering Science* 58 (13): 2857–74.
Schindelin, Johannes, Ignacio Arganda-Carreras, Erwin Frise, Verena Kaynig, Mark Longair, Tobias Pietzsch, Stephan Preibisch, et al. 2012. "Fiji: An Open-Source Platform for Biological-Image Analysis." *Nature Methods* 9 (7): 676–82.
Seifi, Mohsen, Ayman Salem, Jack Beuth, Ola Harrysson, and John J. Lewandowski. 2016. "Overview of Materials Qualification Needs for Metal Additive Manufacturing." *JOM Journal of the Minerals Metals and Materials Society* 68 (3): 747–64.
Seki, Y., S. Okamoto, H. Takigawa, and N. Kawai. 1990. "Effect of Atomization Variables on Powder Characteristics in the High-Pressured Water Atomization Process." *Metal Powder Report* 45 (1): 38–40.
Sercombe, T. B., and X. Li. 2016. "Selective Laser Melting of Aluminium and Aluminium Metal Matrix Composites: Review." *Materials Technology* 31 (2): 77–85.
Shellabear, M., and O. Nyrhilä. 2004. "DMLS-Development History and State of the Art." *Laser Assisted Netshape Engineering 4, Proceedings of the 4th LANE*, 21–24.
Shivkumar, S., C. Keller, and D. Apelian. 1990. "Aging Behavior in Cast Al-Si-Mg Alloys." *AFS Transactions* 98: 905–11.
Siddique, Shafaqat, Muhammad Imran, and Frank Walther. 2017. "Very High Cycle Fatigue and Fatigue Crack Propagation Behavior of Selective Laser Melted AlSi12 Alloy." *International Journal of Fatigue* 94 (January): 246–54.
Siddique, Shafaqat, Muhammad Imran, Eric Wycisk, Claus Emmelmann, and Frank Walther. 2015. "Influence of Process-Induced Microstructure and Imperfections on Mechanical Properties of AlSi12 Processed by Selective Laser Melting." *Journal of Materials Processing Technology* 221 (July): 205–13.
Siddique, S., E. Wycisk, and G. Frieling. 2015. "Microstructural and Mechanical Properties of Selective Laser Melted Al 4047." *Applied Mechanics*. https://www.scientific.net/AMM.752-753.485.
Slotwinski, J. A., E. J. Garboczi, P. E. Stutzman, C. F. Ferraris, S. S. Watson, and M. A. Peltz. 2014. "Characterization of Metal Powders Used for Additive Manufacturing." *Journal of Research of the National Institute of Standards and Technology* 119 (September): 460–93.
Sönegard, Johan, and Maria Warholm. 2017. "Industrialization of Additive Manufacturing." Edited by Hans Sjöberg. Master's Degree, Chalmers University of Technology. http://publications.lib.chalmers.se/records/fulltext/249679/249679.pdf.
Spierings, A. B. 2011. "Influence of the Particle Size Distribution on Surface Quality and Mechanical Properties in AM Steel Parts." *Rapid Prototyping Journal* 17 (3): 195–202.

Spierings, Adriaan B., and Gideon Levy. 2009. “Comparison of Density of Stainless Steel 316L Parts Produced with Selective Laser Melting Using Different Powder Grades.” In *Proceedings of the Annual International Solid Freeform Fabrication Symposium*, 342–53. Austin, TX.

TABOR, and D. 1951. “The Hardness and Strength of Metals.” *Journal of the Institute of Metals* 79: 1.

Tabor, D. 2000. *The Hardness of Metals*. Oxford: Oxford University Press.

Tang, Ming, and P. Chris Pistorius. 2017. “Oxides, Porosity and Fatigue Performance of AlSi10Mg Parts Produced by Selective Laser Melting.” *International Journal of Fatigue*, Fatigue and Fracture Behavior of Additive Manufactured Parts, 94 (January): 192–201.

Tang, Ming, P. Chris Pistorius, and Jack L. Beuth. 2017. “Prediction of Lack-of-Fusion Porosity for Powder Bed Fusion.” *Additive Manufacturing* 14 (March): 39–48.

Tradowsky, U., J. White, R. M. Ward, N. Read, W. Reimers, and M. M. Attallah. 2016. “Selective Laser Melting of AlSi10Mg: Influence of Post-Processing on the Microstructural and Tensile Properties Development.” *Materials & Design* 105 (September): 212–22.

Trevisan, Francesco, Flaviana Calignano, Massimo Lorusso, Jukka Pakkanen, Alberta Aversa, Elisa Paola Ambrosio, Mariangela Lombardi, Paolo Fino, and Diego Manfredi. 2017. “On the Selective Laser Melting (SLM) of the AlSi10Mg Alloy: Process, Microstructure, and Mechanical Properties.” *Materials* 10 (1): 76.

Uzan, Naor Elad, Roni Shneck, Ori Yeheskel, and Nachum Frage. 2017. “Fatigue of AlSi10Mg Specimens Fabricated by Additive Manufacturing Selective Laser Melting (AM-SLM).” *Materials Science and Engineering: A* 704 (September): 229–37.

Wang, Di, Shibiao Wu, Fan Fu, Shuzhen Mai, Yongqiang Yang, Yang Liu, and Changhui Song. 2017. “Mechanisms and Characteristics of Spatter Generation in SLM Processing and Its Effect on the Properties.” *Materials & Design* 117 (March): 121–30.

Wohlers, Terry, Tim Caffrey, Robert Ian Campbell, Olaf Diegel, and Joseph Kowen. 2018. *Wohlers Report 2018: 3D Printing and Additive Manufacturing State of the Industry; Annual Worldwide Progress Report*. Wohlers Associates.

Yasa, Evren, Jan Deckers, Tom Craeghs, Mohsen Badrossamay, and Jean-Pierre Kruth. 2009. “Investigation on Occurrence of Elevated Edges in Selective Laser Melting.” In *International Solid Freeform Fabrication Symposium, Austin, TX, USA*, 673–85. pdfs.semanticscholar.org.

Zhou, Le, Abhishek Mehta, Esin Schulz, Brandon McWilliams, Kyu Cho, and Yongho Sohn. 2018. “Microstructure, Precipitates and Hardness of Selectively Laser Melted AlSi10Mg Alloy before and after Heat Treatment.” *Materials Characterization* 143: 5–17.